Study on stabilization/solidi?cation of selenium oxyanions in geopolymer

田, 全志

Study on stabilization/solidification of selenium oxyanions in geopolymer

By

Quanzhi Tian

A thesis submitted to
Kyushu University
for the degree of
Ph.D.

Department of Earth Resources Engineering
Graduate School of Engineering
Kyushu University

September 2020

Contents

Abstract

Waste production has risen tenfold in the past decades as industrialization and urbanization increase, and waste management has been gradually one of the major environmental concerns in the world. One of the most harmful aspects of solid wastes is the leachability of hazardous elements to the surroundings (e.g. groundwater or soil). Selenium (Se) can be associated with coal or other minerals, so Se can be discharged in the mineral processing, smelting process, and combustion of coal as well as radioactive wastes as ^{79}Se. Once it is discharged, it is easily diffused as mobile oxyanions (SeO_3^{2-} and SeO_4^{2-}). Cement-based stabilization/solidification (S/S) is a conventional treatment for solid wastes. However, there are some disadvantages for cement-based S/S: (1) relatively high leaching rate, (2) susceptible hydration process, and (3) larger amount of CO_2 emission. Geopolymer (GEO) is a solidified material which is formed through condensation polymerization of alkaline silica solution with powdery aluminosilicate. Currently, it has been attracted much attention because of its greater mechanical strength and chemical stability than Ordinary Portland Cement (OPC). The greatest feature of GEO is to deep cut of CO_2 emission in production. Few studies have focused on the immobilization of anionic species in GEO. In the present thesis, the effects of activator and additives on the immobilization of Se oxyanions in GEO were investigated. Then, based on the new phenomena, more works have been done for clear elucidation.

In **Chapter 1**, background information including hazardous waste pollution, the policies for solid waste treatment, treatment techniques were summarized. GEO is proposed to be a promising material for S/S. In order to overcome the low affinity of anionic species to GEOs, some strategies are proposed. Then, the objectives of this

thesis were proposed. All methodologies used in this thesis were summarized in **Chapter 2**.

In **Chapter 3**, the immobilization of SeO_3^{2-} and SeO_4^{2-} was explored using GEOs activated by different alkaline solutions (NaOH and Na_2SiO_3), with/without calcined hydrotalcite (CHT). Na_2SiO_3-activated GEOs without CHT additive showed the greater stability of SeO_3^{2-} and SeO_4^{2-} than NaOH-activated GEOs. It has been proven that electrostatic interaction is the main association mode of SeO_3^{2-} and SeO_4^{2-} in both GEOs. Higher compactness played a vital role in suppressing Se leaching from GEO. The addition of CHT reduced the compactnesses of Na_2SiO_3-activated GEOs. Soluble silicate disturbed the formation of hydrotalcite, since aluminum is preferentially consumed by polymerization of aluminosilicate. However, this phenomenon was not observed in NaOH-activated GEOs. The CHT additive contributed to immobilize SeO_3^{2-} and SeO_4^{2-} in NaOH-activated GEOs. Thus, the stability of Se oxyanions is influenced mainly by activators affecting the development of aluminosilicate to increase in compactness of the GEO, and marginally by regeneration of HT from CHT additive without silicate activator.

As above mentioned, the soluble silicate has a significant effect on the memory effect of layered double hydroxides (LDHs). The influence of silicate on the structural memory effect of LDHs was focused excluding silica precursors such as metakaolin and silica fume. In **Chapter 4**. five types of calcined LDHs (CLDHs) were synthesized by the combination of Mg, Al, and Fe with different molar ratios, to apply for the sorption of Se oxyanions with/without silicate at the initial pH 10 and 13. The results indicated that silicate can significantly affect the phase transformation of CLDHs, and the sorption amounts of selenite and selenate dramatically decreased in the presence

of silicate. Specifically, silicate can react with MgO and Al_2O_3 in CLDHs to generate magnesium silicate hydrate and geopolymer-like substance which were covered on the surface of particles, blocking the hydroxylation of metal oxides, then resulting in the non-regeneration of LDHs particularly for CLDH-1 (Mg_2Al-oxide) and CLDH-4 ($Mg_2Fe_{0.67}Al_{0.33}$-oxide) after reaction at pH 10. However, higher pH suppressed the interaction between MgO and silicate and enhanced the formation of a geopolymer-like substance, which promoted the regeneration of LDHs. Al in CLDHs plays a critical role in the regeneration of LDHs. In addition, the ternary oxides (CLDH-2, $Mg_2Fe_{0.33}Al_{0.67}$-oxide; CLDH-3, $Mg_2Fe_{0.5}Al_{0.5}$-oxide) possessed larger specific surface areas (127.7 and 158.2 m^2/g) and consequently presented more resistance to silicate.

The LDHs were always regenerated in the NaOH-activated GEOs showing a suppressive effect on Se leaching in **Chapter 3**. A novel function of the composite of LDH/GEO was explored in the cosorption of Cs^+ and SeO_4^{2-} in **Chapter 5**. The adsorption density of Cs^+ on LDH/GEO was maintained as that on pure GEO, even though the surface of GEO was covered with LDH platelets. The sorption of Cs^+ onto LDH/GEO composite occurred via ion exchange, controlled by particle diffusion, which was different from Cs^+ sorption onto pure GEO governed by film diffusion. Therefore, "Pocket diffusion" was proposed for particle diffusion as the case of LDH/GEO. For SeO_4^{2-} sorption by LDH/GEO, ion-exchange with the interlayer NO_3^- and surface sorption could be the main mechanisms. Importantly, the sorption speed of SeO_4^{2-} achieved by LDH/GEO composite was much faster than that by pure LDH. In the binary system (Cs^++ SeO_4^{2-}), the sorption of Cs^+ was slightly suppressed compared to the single system, mainly due to the formation of the ion-pair complex of

$[CsSeO_4]^-$. However, it did not have a negative effect on the SeO_4^{2-} sorption. In the presence of other cations or anions, the cosorption performances of Cs^+ and SeO_4^{2-} were satisfactorily obtained. The combined MgAl-LDH/geopolymer composite can be a promising material for the immobilization of Cs^+ and SeO_4^{2-}.

In order to further enhance the immobilization efficiency of selenate in geopolymer, the ferrous additive was explored to include in the reaction system in **Chapter 6**, where key reactions were extracted to simplify by using alkaline earth metallic oxides (CaO and MgO) as precursors. The results indicated that selenate was mostly reduced to selenite in the CaO-based reaction within 7 day-curing. Then the generated selenite was mainly adsorbed onto Fe(III)-bearing minerals (Fe_2O_3 and FeOOH) through the formation of both bidentate mononuclear edge-sharing (^1E) and monodentate mononuclear corner-sharing (^1V) inner-sphere surface complexes, suggested by PHREEQC simulation and extended X-ray absorption fine structure (EXAFS) analysis. Differently, less amount of selenate (~45.50%) was reduced to selenite in the MgO-based reaction. However, if the curing time increases to a longer time (more than 7 days), further reduction could occur because there are still Fe(II) species in the matrix. Most of the selenium (SeO_3^{2-} and SeO_4^{2-}) was preferentially distributed onto the $Mg(OH)_2$ through outer-sphere adsorption.

In **Chapter 7**, the main conclusions were summarized. It has been certified that geopolymer can be able to immobilize selenium oxyanions through electrostatic interaction. The reaction processes and mechanisms have been explored and proposed. Based on the results, novel geopolymerization systems including the selection of activators, necessity of additives, etc. can be designed and proposed.

List of Tables

List of figures

Abbreviations

S/S	Stabilization/solidification
OPC	Ordinary Portland cement
MOC	Magnesia-based cement
MKPC	Magnesium potassium phosphate cement
FA	Fly ash
LDH	Layered double hydroxides
CLDH	Calcined layered double hydroxides
MK	Metakaolin
QXRD	Quantitative X-ray diffraction
CHT	Calcined hydrotalcite
GEO	Geopolymer

Chapter 1

Introduction

1.1 Solid waste pollution

The sources of solid waste could be divided into several aspects including industrial, residential, and commercial activities, etc. [1]. Since the last century, waste production has risen sharply as the world's population has grown and gradually become more urban and affluent. It has been predicted that it will double again by 2025. Specifically, the global solid-waste generation would increase from more than 3.5 million tonnes per day in 2010 to more than 6 million tonnes per day in 2025 [2]. Solid waste composition varies substantially with industries, technologies, locations, waste collections, etc. On the whole, solid waste can be divided into several categories including industrial wastes (e.g. tailing, fly ash, slag, sludge, etc.), municipal wastes (e.g. metal, paper, organic matter, etc.) and agricultural wastes (e.g. rice husk, food waste, etc.) [3-6]. Once these solid wastes cannot be properly handled, serious air, water, and soil pollutions would be caused. For example, it has been reported that aromatic compounds are major components of volatile organic compounds emitted from municipal solid waste landfills, significantly contributing to air pollution [7]. The leachates of solid wastes such as fly ash, tailings, and municipal waste have been confirmed to easily contaminate river and groundwater [8]. Moreover, the improper disposal of tailings has led to serious soil contamination in the world [9]. Therefore, human health can be affected by these contaminations caused by solid wastes. Many studies have been carried out in various parts of the world to establish a connection between health and waste [10]. Hence, proper treatment of each kind of solid waste is extremely important for the sustainable development of human society.

Heavy metal pollution has become a severe problem in many parts of the world, mainly caused by anthropogenic activities including mining, smelting, coal

combustion, etc [11]. Specifically, it is precise because of the improper disposal of the wastes produced from these anthropogenic activities. Heavy metal pollution is converted, persistent, and irreversible due to that heavy metals cannot be decomposed like organic matters, but they can exist in various chemical associations. In the past five decades, more than 800,000 tons of Pb and 30,000 tons of Cr were released into the environment globally, and most of them were accumulated in soil [12]. This kind of pollution not only degrades food crops but also threatens the health and well-being of animals and human beings through the food chain [13, 14]. Specifically, Pb is a non-essential element to the human body, and excessive uptake of Pb can damage the nervous, skeletal, enzymatic, and immune systems of humans [15]. Furthermore, it has been reported that Cd-contaminated rice leads to the "Itai-Itai disease" which happens in Japan during the 1950s and is also found in China [16]. Some other metals including Hg, Zn, Cu, Ni, etc. have been detected in many regions, with extremely high concentrations, which severely affects the local corps and human health [12, 17-19]. Besides these cationic pollutants, anionic pollutants such as As, Se which are generally called metalloids can also lead to serious pollutions to the environment. Excessive and long-term intake of As can cause arsenicosis, thereby leading to skin problems, skin cancers, diseases of the blood vessels, high blood pressure, and reproductive disorders [20]. There are two kinds of As species including arsenite and arsenate normally detected in the water. Similarly, selenite and selenate are the dominant species of Se in aqueous environments. Excessive Se in soil and/or water could also lead to severe risk and damage to human health, due to the anthropogenic activities including mining, coal combustion, oil refining, etc. [21, 22]. More seriously, ^{79}Se is a critical radionuclide in terms of the safe disposal of radioactive wastes because of its long half-

life (2.95×10^5 yrs) [23, 24]. Once ^{79}Se is released into environments (e.g. Fukushima nuclear accident), it would bring serious disaster to the world. In addition to As and Se, there are several inorganic anions including fluoride, bromate, and phosphate, etc. which can also bring about severe pollutions [25].

According to the above statement, both cationic and anionic metal ions can cause serious pollutions to the environment. Compared to cationic species, anionic species possess higher mobility and transportability because they cannot easily be sorbed on some natural clay minerals due to the charge repulsion. Furthermore, anionic species such as As and Se can still be in the ionic state under both acidic and alkaline conditions, and this is different from cationic species such as Cu, Pb, and Zn which would precipitate at alkaline pH. Particularly, the Se oxyanions have very low affinities to other metal ions including Ca^{2+}, Mg^{2+}, Fe^{3+}, etc. and they can transport easily in the natural environments. Therefore, the remediation of anionic pollutants should be paid much attention as well as cationic pollutants.

1.2 Solid waste treatment

1.2.1 Resource recovery

In the current predominantly linear production and consumption systems, resource recovery is considered to be one of the important aspects of waste management [26, 27]. It is a kind of strategic investment aiming for zero waste residue and requiring limited external energy input. The developed technologies including gravity separation, magnetic separation, flotation, leaching, etc. can recover different types of materials from mixed waste matrices. For instance, many studies have proposed to recover the unburned carbon from coal fly ash using flotation, and the

purified fly ash can be used for cement production [28-30]. The recovery of precious metals from wastes such as waste printed circuit boards by hydrometallurgical processing is also recommended [31]. The utilization of red mud as the source materials for construction materials, glass ceramics, iron production, extraction of rare earth elements, and environmental protection, etc. has also been proposed by researchers [32, 33]. However, only 30% of the total waste material is involved in resource recovery globally [26]. Resource recovery from solid waste is a complex procedure because the capital market is another important factor for the resource recovery process besides the advanced technologies. Resource recovery should result in strategic economic benefits, and such economic benefits need to outweigh the recovery costs. Then, the process of resource recovery can be conducted securely.

1.2.2 Waste reduction/minimization

There are several definitions of waste reduction/minimization promoted by governing bodies in the international community. On one hand, it refers to the use of source reduction or strategies that are aiming to prevent waste through upstream interventions [34-36]. It aims to strengthen awareness and prompt environmentally conscious consumption patterns and consumer responsibility to reduce the overall levels of waste generation. But for the fixed amount of produced wastes, waste reduction means reducing the volumes of hazardous wastes for further landfilling or transportation. A typical example is the incineration of municipal solid waste. It is the most common waste treatment because the waste mass and volume can be reduced by 70% and 90%, respectively [37]. The emissions from waste incinerators can be reduced to an extremely low level by adopting pollution control technologies.

Importantly, heat and/or electricity can also be produced. Incineration is currently considered as attractive waste treatment, especially in developed countries [38]. However, incineration is just only suitable for combustible solid waste. For the non-combustible wastes such as construction waste, crushing, and compacting are generally needed to reduce the waste volume [39].

1.2.3 Safe disposal of wastes

The safe disposal of solid wastes, especially hazardous wastes, can be seen as the final and vital step of effective waste management [40]. Before the waste disposal, the prior activities such as waste collection, prevention, minimization, storage, treatment, etc. could have been conducted. Thus, the safe waste disposal can be regarded as a multiphase activity composed of all the aforementioned stages, and its main purpose is to prevent/reduce the motilities of pollutants in the waste [40]. Currently, the sanitary landfill method for the ultimate disposal of solid waste such as municipal solid waste is still to be widely accepted and used because of its economic advantages [41]. Besides, the deep disposal is normally adopted for the isolation of hazardous wastes, especially radioactive wastes. Therefore, stabilization/solidification (S/S) is always adopted as the pretreatment process before landfilling or burying in the underground to achieve the safe disposal of hazardous wastes [42]. Generally, the S/S process is to mix the solid waste with binding material including cement, asphalt, etc. to achieve good physical properties and meanwhile immobilize harmful components within solidified material [43, 44]. It can be seen that the binding material plays a critical role in the S/S performance for the specific waste.

1.3 Stabilization/solidification for hazardous wastes

1.3.1 Materials

According to the above statement, the S/S process is an important step to prevent pollutants from releasing into the environment, and the overall S/S performance can be controlled by the selected material and the specific waste. In the S/S process, cement is the most frequently used and widely studied material due to the simple operation, low processing cost, and good efficiency in the reduction of heavy metal leaching [45]. Ordinary Portland cement (OPC) is, of course, the most broadly adopted for the S/S process. Mineralogically, OPC is composed of four main phases which have idealized compositions close to Ca_2SiO_5 (50-70%), Ca_2SiO_4 (15-30%), $Ca_3Al_2O_6$ (5-10%) and $Ca_2(Al, Fe)O_5$ (5-15%) [46, 47]. The hydration products of OPC mainly include calcium silicate hydrate (C-S-H), ettringite (AFt), and monosulfate (AFm), etc. which are believed to be the main holders for both cationic and anionic pollutants [48]. Bie et al. [49] reported that the leaching concentration of Pd and Cd from MSWI fly ash significantly reduced after being mixed with OPC. Clancy et al. [50] conducted the S/S of arsenic-bearing iron wastes by cement and found that cement stabilization lowered arsenic leaching at high pH. In many cases, some additives were added into OPC pastes to improve the S/S performance. For example, Mallampati et al. [51] found that the immobilization efficiencies of heavy metals (As, Cd, Cr, and Pb) increased from 85-90% to 98-100% by adding a nanometallic Ca/CaO dispersion mixture produced by grinding. Lasheras-Zubiate et al. [52] proposed that the chitosan additives can not only reduce the Zn leaching but also enhance the compressive strengths of the mortars. On the other hand, many researchers proposed to use coal fly ash or slag (or partially replaced with cement) for the solidification of hazardous wastes because of

the high energy consumption and a large amount of CO_2 released during cement production. Dermatas et al. [53] utilized fly ash and quicklime to immobilize lead and chromium contaminated soils, and it effectively reduced heavy metal leachability below the nonhazardous regulatory limits. Furthermore, Wang et al. [54] used calcined kaolinite activated by CaO to stabilize As and Pb in the contaminated soil, and the leachabilities of As and Pb in high-Ca S/S treated samples were reduced by 96.2% and 98.8%. According to the above statement, no matter what kind of materials are used for the S/S process, the pozzolanic reaction is the basic reaction of them. Thus, the S/S using OPC, coal fly ash and calcium oxide, slag, and other activated silicon/alumina can be classified as pozzolanic-based S/S treatment.

Magnesia-based cement (MOC) as an alternative type of cement uses MgO as a building block rather than CaO that comprises more than 60% of the OPC compositions [55]. The lower temperatures required for the production of MgO compared to the conversation of $CaCO_3$ to OPC leads to envision MgO-based cement as being central to the future of eco-friendly cement production [55]. Normally, it includes magnesium-phosphate cement, magnesium oxychloride cement, etc. which have been also adopted as S/S materials. Ma et al. [56] used magnesium oxychloride cement as a stabilizer for S/S of sewage sludge and achieved better mechanical strength and immobilization ability. Wang et al. [57] concluded that magnesium potassium phosphate cement (MKPC) is an efficient and chemically stable inorganic binder for the Pb S/S process. Su et al. [58] used MKPC as immobilization material for the S/S of incineration fly ash (MSWI FA) and found that the mixture of MKPC and MSWI FA exhibited a synergistic effect on S/S of Pb and the S/S blocks with less than 20% MSWI FA can be used as the construction materials. Furthermore, Qian et

al. [59] conducted the S/S of radioactive fluoride liquid waste using MKPC and concluded that the freeze-thaw resistance of MKPC paste was enhanced. Similarly, the utilization of magnesia-based cement can also consume some industrial wastes while for the S/S process. Wang et al. [60] summarized that low-carbon MgO and Si-rich waste materials (e.g. glass powder) can be a promising cementitious material for the S/S of contaminated sediment. Also, Viani et al [61] examined the magnesium phosphate cement prepared from asbestos wastes and the measured strengths can be satisfied with the cement standard. There are still other studies indicating that magnesia-based cement is a promising material for the S/S process due to their good mechanical strengths and encapsulation abilities [62-65]. In addition to OPC and MOC, there are other types of cement including calcium aluminate cement, sulfate aluminate cement, etc. which have been adopted as the S/S of heavy metals [66-69]. For instance, Navarro-Blasco assessed the ability of calcium aluminate cement to encapsulate toxic metals, and found that almost all of Cu and Pb were retained in the mortars [66]. In this case, calcium aluminate cement was perfectly able to encapsulate the toxic metals, allowing its utilization for waste management.

On the other hand, high-level radioactive wastes are the highly radioactive materials produced as a byproduct of the reactions that occur inside nuclear reactors. Because of their highly radioactive fission products, high-level waste, and spent fuel must be handled and safely stored for a very long time [70]. Thus, titanate, zirconate, and phosphate-based ceramics have been particularly used for the safe storage of high-level radioactive wastes, together with iron phosphate-based glasses and basaltic glass-ceramics [71].

1.3.2 Mechanisms

As for the pozzolanic reaction (**Fig. 1.1a**), the hydration products including ettringite, hydrocalumite, and calcium silicate hydrate (C-S-H) would be generated, and these newly formed phases, especially ettringite and hydrocalumite, are considered to be able to incorporate anions, such as AsO_4^{3-}, MoO_4^{2-}, into their structures [47, 72]. These anionic pollutants including $B(OH)_4^-$, SeO_3^{2-}, AsO_4^{3-}, MoO_4^{2-}, etc. can be effectively incorporated into the structures of ettringite [73-75]. Furthermore, more specific incorporation mechanisms of anionic species into ettringite have been proposed. Generally, ettringite has a structure based on columns of empirical composition $(Ca_2(Al(OH)_6)\cdot 12H_2O)^{3+}$ which run parallel to the needle axis, and the sulfate ions and remaining water molecular lie between them (**Fig. 1.1b**) [76]. It has been confirmed that the incorporation of SeO_4^{2-} into ettringite is mainly through oxyanion exchange. By contrast, SeO_3^{2-} is easily immobilized to form inner-sphere complexes in ettringite [24]. Furthermore, SeO_4^{2-}–substituted hydrocalumite was formed as an intermediate and then transformed to SeO_4^{2-}–substituted ettringite [77]. Also, IO_3^- can be stabilized in ettringite by hydrogen bonding and electrostatic forces, and it was also confirmed that substituting IO_3^- for SO_4^- was energetically favorable by – 0.41 eV [78]. Cr(III) in solution with a pH higher than 12 shows $Cr(OH)_4^-$, CrO_2^- or oxidized form of CrO_4^{2-} which might be able to incorporate into the interlayer of hydrocalumite (**Fig. 1.1b**) [79]. However, some previous studies suggested that Cr(III) could directly participate in the structure of ettringite as cation [80, 81]. Except for the structural incorporation in ettringite or hydrocalumite, precipitation is also an important immobilization mechanism for some anions. For instance, F^- as a common pollutant in the wastes could react with Ca^{2+} to precipitate as CaF_2 ($Ksp \approx 10^{-10}$, 25 °C),

then it would be immobilized in the cement pastes [82]. Phosphate ions can be involved with calcium-based precipitation to form the precipitates such as hydroxyapatite ($Ca_{10}(PO_4)_6(OH)_2$) or struvite ($NH_4MgPO_4{\cdot}6H_2O$) with low *Ksp* values [83, 84]. In addition to anionic species, most of the cations including Pb^{2+}, Zn^{2+}, Cd^{3+}, Co^{3+}, etc. can precipitate in the alkaline condition, and then immobilized in the cement pastes. Specifically, Pb can be retained in OPC as plumalsite ($Pb_4Al_2(SiO_3)_7$), lead silicate hydrate ($Pb_2SiO_4{\cdot}xH_2O$) and alamosite ($PbSiO_3$) [85]. In addition, the formation of $ZnAl_2(SO_4)_4{\cdot}22H_2O$ and the incorporation of Zn in C-S-H are the main immobilization mechanisms of Zn in OPC [85, 86]. It can be seen that these cations could exist in several phases in the OPC cement. This "multi-phase immobilization" phenomenon also occurs in the case of the immobilization of other cations such as Cd, Ni, in cement pastes [47]. Therefore, the mechanisms for the S/S process using OPC should include physical encapsulation, (co-) precipitation, sorption, incorporation, etc.

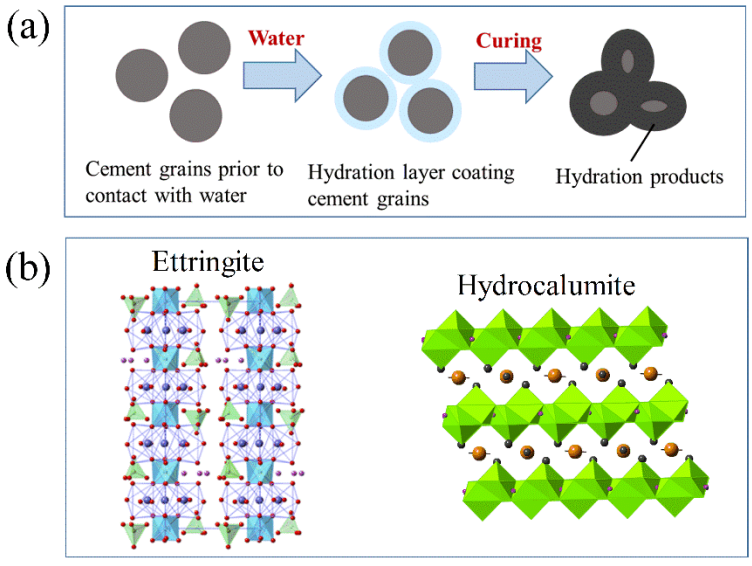

Fig. 1.1 Schematic diagrams of (a) pozzolanic reaction and (b) structures of ettringite and hydrocalumite [87].

Similarly, physical encapsulation is also an important mechanism of heavy metal immobilization for other cement, such as MOC. However, different chemical reactions

occur in various cement systems. Compared to OPC reaction, Pb^{2+} can be stabilized in the MKPC paste by the chemical precipitation with residual phosphate (e.g. pyromorphite and lead phosphate), which showed better S/S performance [57]. In addition, Cd can also react with phosphate to form the stable phase of $NaCdPO_4$ [88]. Analogously, the formation of hopeite ($Zn_3(PO_4)_2 \cdot 4H_2O$), scholzite ($CaZn_2(PO_4)_2 \cdot 4H_2O$), zinc hydroxide ($Zn(OH)_2$), and fluoropyromorphite ($Pb_5(PO_4)_3F$) is the main mechanisms for the immobilizations of Zn and Pb using the KMP binder consisted of a mixture of oxalic acid-activated phosphate rock, monopotassium phosphate (KH_2PO_4) and reactive magnesia (MgO) [89]. Thus, it can be known that PO_4^{3-} ion plays a critical role in the immobilization of cationic pollutants. As for ceramics and glasses, the extremely dense structures of them greatly contribute to the effective S/S of hazardous wastes. Thus, based on the above analysis, no matter what kind of materials used for the S/S process, the mechanisms of physical encapsulation, precipitation, incorporation, etc. should be involved.

1.3.3 Existing problems

Each technique has certain advantages and disadvantages. The S/S using cement especially OPC is, of course, an effective and economic method for the treatment of hazardous wastes. However, the cement hydration could be to some extent easily affected by heavy metals in hazardous waste. Specifically, heavy metal ions could result in the reduction of pH and accelerating cement hydration, further influencing the nucleation and growth of reaction products [43]. Furthermore, cement-based S/S of wastes is relatively fragile to physical and chemical degradation processes, which depends on factors such as permeability, chemical and mineralogical composition, and

microstructure [90]. Carbon dioxide attack might be probably the most common degradation mechanism for cement-solidified waste. The pH would become lower because of the reaction between dissolved CO_2 and the phases including $Ca(OH)_2$ and C-S-H [43, 91]. Besides the CO_2 attack, the cement pastes can also suffer attacks from sulfate, chloride, water, and some organic substances, consequently leading to the change of porosity, volume, and solidified waste performance [92]. This may cause expansion, cracking as well as strength loss. On the other hand, the lifetime of concrete produced from OPC is approximately 50-100 yrs [93]. This is not suitable for the S/S of hazardous wastes, especially radioactive wastes, for a long time. Also, the production of ordinary Portland cement could consume much energy and meanwhile lead to massive CO_2 emission [54, 94, 95]. Therefore, more and more attention should be increasingly paid to develop environmentally friendly construction/solidification materials.

1.4 Geopolymer

1.4.1 Synthesis

Geopolymers are a kind of inorganic polymers consisted of SiO_4 and AlO_4 tetrahedrons connected by sharing the oxygen atoms [96]. They can be normally synthesized by low-temperature polycondensation of different materials such as metakaolin, coal fly ash [97]. It has been viewed as a practical alternative to Portland cement because it exhibits better mechanical properties and durabilities, and has lower energy requirement and greenhouse gas emission [98]. Other applications including fire-resistant materials [99], foams, and radioactive waste management [100], etc. have also been explored. For the synthesis of geopolymer, there can be broadly two kinds

of geopolymer synthesis methods. Geopolymer is the most commonly refer to the inorganic aluminosilicate based on geological materials which can react with an alkaline solution to form binder through polycondensation reaction [101]. Another way is to use acidic phosphate component or phosphoric acid as the activator for the complex acid-based reaction to initiate, and the obtained solid can also be called chemically bonded phosphate ceramics [4]. Compared to the alkali-activation, the low reactivity of silicate-based minerals limit them for the synthesis of phosphate bonding ceramics. Thus, the term "geopolymer" would be just referred to alkali-activated materials in this thesis. Under alkali conditions, the aluminum and silicon are dissolved from the aluminosilicate source. After reaching the equilibrium, the dissolved Al and Si tetrahedrons would go through gelation, reorganization, and polymerization to form the hardened geopolymer paste [102]. Based on the experimental results and theoretical deduction, Davidovits proposed the structural model of K-geopolymer as shown in **Fig. 1.2** [102], and it can be seen that the monolithic polymer has a cross-linked inorganic network resembling organic polymers.

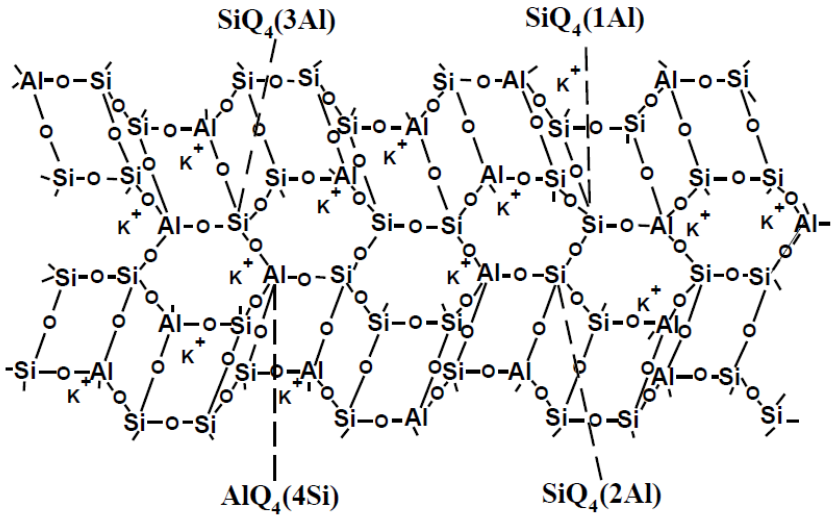

Fig. 1.2 Proposed structural model for geopolymer [103].

Based on the aluminosilicate sources, geopolymer materials can be divided into several types including fly ash-based geopolymer, metakaolin-based geopolymer, slag-based geopolymer, mine tailing-based geopolymer, etc [104, 105]. Different aluminosilicates could possess various chemical activities. Therefore, geopolymer properties such as mechanical performance, thermal behavior, durability, would have a close relationship with these aluminosilicates. For example, the compressive strength of fly ash-based geopolymer has been reported as higher than 47 MPa [96]. However, the red mud-based geopolymer just shows a low compressive strength of 20.5 MPa [106]. It is widely accepted that amorphous phases in the aluminosilicate source are the main reactive components in the geopolymerization, and most of the crystalline phases are hardly dissolved during the reaction [107]. Thus, the thermal activation is an effective method to modify the physicochemical properties of materials. During heat treatment, phase transformations occur in the material, resulting from the loss of volatile components and reorganization of atomic structures [108]. For example, kaolinite can be converted into metakaolin through the calcination at temperatures between 700 and 900 °C [109]. However, there is no change on some minerals such as quartz, mullite after thermal treatment. Thus, alkaline fusion was proposed to increase the geopolymeric reactivity of materials. The structures of quartz and mullite would be decomposed by the calcination of the mixture of raw material and sodium hydroxide, then promoting the dissolution of Si and Al species [108]. Besides, mechanical activations including grinding, comminution, etc. have also been put forward to increase the specific surface areas and reaction sites. On the other hand, NaOH or KOH and Na_2SiO_3 or K_2SiO_3 solutions are commonly used as the activators for geopolymer synthesis [110, 111]. Generally, the geopolymer pastes activated by Na_2SiO_3 solution

always have better mechanical strength than that obtain from NaOH activation [110, 111]. Thus, it can be known that soluble silicate has a significant effect on the properties of geopolymer. Except for being a new kind of binder, there are many other applications of geopolymer including fire- and heat-resistant coating and adhesives, high-temperature ceramics, fire-resistant fiber composite, and hazardous waste encapsulation, etc. It should be noted that effective S/S of toxic waste using geopolymer is the main target of this thesis.

1.4.2 S/S of hazardous wastes

In recent years, geopolymers have been gradually attracted much attention for the S/S treatment. The permanently negative charges produced from Al tetrahedrons can make it always have strong affinities with cations [112]. There are also many studies focusing on the S/S of cationic species including Pb^2, Zn^{2+}, Mn^{2+}, Co^{2+}, Ni^{2+}, Cs^{+}, Sr^{2+}, etc. as shown in **Table 1.1**. The majority of synthesized geopolymers for the S/S process were based on the fly ash and metakaolin, and the addition of the simulated heavy metal pollutants was mainly mixed with the aluminosilicate precursor and alkali activator [112]. The toxicity characteristic leaching procedure (TCLP) which is the standard toxic leaching method recommended by the Environmental Protection Agency (EPA) has been the most widely used for human health assessment [113]. Besides, the acid, base, and salt solution were also used in leaching for simulating various environmental conditions, which could provide important information for geopolymer applications in complex natural environments [112]. From **Table 1.1**, the S/S efficiencies for cations are always higher than 95%. It has been proven that geopolymers always show good S/S performance for cationic species, mainly because

of the permanently negative charges of geopolymer which can be compensated by cations. On the other hand, the cations can also react with OH^- to form precipitates, contributing to the S/S performance.

However, few studies have focused on the immobilization of anionic species in geopolymer. Currently, only several studies about the immobilization of anionic species using geopolymers were reported. Al-Mashqbeh [122] utilized metakaolin-based geopolymers to immobilize the inorganic anions ($Cr_2O_7^{2-}$, MnO_4^- and $Fe(CN)_6^{3-}$) and concluded that geopolymer had limited capacity for the immobilization of metal anions. Nikolić [126] employed fly ash-based geopolymers to immobilize Cr(VI) and found that geopolymer pastes containing Cr (0.5–2.0%) cannot meet the requirement of landfill due to the high leaching concentration. Since geopolymers possess many excellent properties as stated above, it would extend the application of geopolymer in the S/S of anionic pollutants if the anionic-intercalated phases could be incorporated into geopolymer pastes. Thus, the main purpose of this thesis is to find a way to adopt geopolymer for the S/S of anionic species.

Table 1.1 Recent studies about S/S of heavy metals using geopolymer.

Materials	Heavy metal species (content)	Curing condition	Leaching conditions or methods	Leaching concentration ($mg \cdot L^{-1}$)	Reference immobilization efficiency	Reference
Class C fly ash Municipal solid waste incineration fly ash Nano-Al_2O_3 particles Nano-SiO_2 particles	Cu (563.2 mg kg^{-1}) Pb (1515.0 mg kg^{-1}) Cr (157.0 mg kg^{-1}) Zn (3269.0 mg kg^{-1})	Cured at room temperature for 24 h.	HJ/T299-2007	Cu (0.03) Pb (< 0.05) Cr (0.11) Zn (< 0.01)	Cu [98.34%] Pb [>98.97%] Cr [78.18%] Zn [>99.90%]	[114]
Fly ash Kaolin/fly ash Kaolin/zeolite	Pb (200/1000 mg L^{-1}) Cd (200/1000 mg L^{-1}) Cu (200/1000 mg L^{-1}) Cr (200/1000 mg L^{-1})	Cured at 80 °C for 24 h.	Distilled water 0.1M NaCl 1.0M NaCl 0.1M HCl 1.0M HCl	Pb (25.0–49.4/8.5–18.3) Cd (0.0–9.2/0.2–1.9) Cu (5.0–20.0/0.9–1.9) Cr (0.0–11.9/0.0–4.1)	Pb [92.45–98.70%] Cd [98.59–100%] Cu [96.94–99.86%] Cr [98.18–100%]	[115]
Bottom ash Metakaolin Waste solution (circuit board industries)	Pb (12619.91 ± 20.78 mg kg^{-1}) Cr (2.6 ± 0.05 mg kg^{-1}) Cu (347.51 ± 3.97 mg kg^{-1}) Sn (2371.07 ± 25.64 mg kg^{-1})	Cured for at room temp., 28 d.	8 M KOH 12 M NaOH	Pb (0.037–0.2)] Cr (0.029–0.06) Cu (0.52–1.0) Sn (0.05–0.5)	Pb [>99.99%] C) [99.39–99.58%] Cu [99.91–99.95%] Sn [>99.99%]	[116]
Fly ash Na_2S NaH_2PO_3 TMT DTCR	$Cr(NO_3)_3$ (0.5–3.0 wt%)	Cured at 20 ± 1 °C, 24 h relative humidity 95 ± 1%.	-	Cr (0.07–1.93)	Cr [99.41–99.87%]	[117]
Power plant fly ash	$Pb(NO_3)_2$ (1.0–3.0 wt%) $Cd(NO_3)_2 \cdot 4H_2O$ (1.0–3.0 wt%) $MnSO_4 \cdot H_2O$ (1.0–3.0 wt%) $Cr(NO_3)_3 \cdot 9H_2O$ (1.0–3.0 wt%)	Cured at 80 °C, 12 h in an oven, and left at the room temperature for 7 d.	HJ/T299-2007	Pb (0.18–0.80) Cd (0.44–1.29) Mn (0.75–1.53) Cr (0.37–1.14)	Pb [99.91–99.94%] Cd [99.75–99.76%] Mn [99.53–99.69%] Cr [99.65–99.66%]	[118]
Coal fly ash	$CsNO_3$ (2%)	Cured at 60 °C for 28 d with the humidity of 90%.	Distilled water	5.4% of the leaching amount from OPC matrix	Not given	[119]
Mn slag	$Co(NO_3)_2 \cdot 6H_2O$ (5.56%)	Cured at 25 °C for 30 d with the humidity of 90%.	TCLP	%leaching Co (0.2-0.25%)	Not given	[120]
Metakaolin Slag	Cu (0.1–0.3 wt%) Pb (0.1–0.3 wt%)	Cured at 20 °C, 8d.	TCLP	Cu [Not given] Pb [Not given]	Cu [98.67–99.66%] Pb [98.84–99.27%]	[121]

Metakaolin Chromite ore processing residue Na_2S	Cr (294.56 mg kg^{-1}) Cr(VI) (279.84 mg kg^{-1})	Sealed with polyethylene film and steam cured at 60 °C for 2 h.	TCLP	Cr (1.37) Cr(VI) (0.01)	Cr [Not given] Cr(VI) [Not given]	[122]
Medical waste incineration ash (Bottom/Fly)	Cr (0.336/0.187 mg kg−1) Zn (0.154/11.80 mg kg−1) Ba (2.535/1.797 mg kg−1)	Cured at 50 °C, 24 h, and aging for 28 d.	TCLP	Cr (0.0245–0.730) Zn (0.012–2.145) Ba (0.3640–0.9856)	Cr [Not given] Zn [Not given] Ba [Not given]	
Metakaolin Potassium dichromate Potassium permanganate Potassium hexacyanoferrate	$K_2Cr_2O_7$ (0.2 wt%) $KMnO_4$ (0.2 wt%) $K_3Fe(CN)_6$ (0.2 wt%)	Cured at 60 °C for 24 h in an oven, and at room temperature for 14 d.	Deionized water 0.1M NaOH 0.1M NaCl 1.0M NaCl 0.1M HCl 1.0M HCl	%leaching 10-20%	Less than 80%	[123]
Electrofilter fly ash Fabric filter fly ash Metakaolin	Cd (EF105/FF190 mg kg^{-1}) Cr (EF196/FF71 mg kg^{-1}) Cu (EF473/FF474 mg kg^{-1}) Ni (EF38/FF0 mg·kg^{-1}) Pb (EF502/FF1363 mg kg^{-1})	Setting stage maintaining the cast at room temperature for 24 h and at 50 °C for 24 h; Cured at room temperature, 7 d.	UNI 10802	Cd (EF0.0/FF0.0) Cr (EF10.09/FF0.64) Cu (EF0.07/FF0.03) Ni (EF0.0/FF0.0) Pb (EF0.03/FF0.11)	Cd [Not given] Cr [Not given] Cu [Not given] Ni [Not given] Pb [Not given]	[124]
Coal fly ash	PbO (1.0–8.0 wt%) $PbSO_4$ (1.0–8.0 wt%) PbS (1.0–8.0 wt%)	Cured at 85 °C for 24 h, 7 d of aging.	TCLP	%leaching PbO (1.03–49.81%) PbSO4 (0.235–2.890%) PbS (0.386–4.360%)	PbO [50.19–98.97%] PbSO4 [97.1199.77%] PbS [95.64–99.61%]	[125]
Chromite ore processing residue (COPR) Blast furnace slag	COPR (10–70 wt%)	Cured at 25 °C, 24 h, 90% relative humidity.	HJ/T299-2007	Cr(VI) (0.027–6.724)	Cr(VI) [Not given]	[126]

Note: the contents of table 1.1 are partially derived from Ref [112]
UNI 10802: Nitric acid, pH = 2.0, vibration time = (24 ± 0.5) h, liquid-solid ratio = 10:1 (L/kg).
HJ/T299-2007: Sulfuric acid–nitric acid, pH = (3.20 ± 0.05), vibration time = 18 h, liquid-solid ratio = 20:1 (L/kg).
TCLP: Acetic acid, pH = (2.88 ± 0.05), temperature= (23 ± 2) °C, vibration time = 18 h, liquid-solid ratio = 20:1 (L/kg).

1.5 Immobilization of Se oxyanions

Selenium (Se), as an essential micronutrient, can benefit the health of them at low concentrations, but excessive intake of Se can result in serious health problems, such as skin lesions, paralysis, etc. [127]. In recent years, Se pollution on water and soil has been reported as a serious problem because of the substantial increase in anthropogenic activities including mining, coal combustion, etc. [128]. Due to its bioaccumulative property, the concentration of Se in the aquatic organisms such as fish and shell animals can increase along the trophic chain. This might further have adverse effects on the health of human beings. On the other hand, ^{79}Se is also one of the fission products in nuclear reactors, and it possesses an extremely long half-life of approximately 1.11×10^6 [77, 129, 130]. Serious injuries on plants, animals, and even humans can be caused once ^{79}Se is unintentionally released into the environment (eg. Fukushima accident), because of its strong radioactivity. Se can exist in several oxidation states including selenide (-II), elemental Se (0), selenite (IV) and selenate (VI), etc. (**Fig. 1.3**). Among them, SeO_3^{2-} and SeO_4^{2-} are the dominant species in water environments, with high mobility and transportability [131]. Therefore, the effective immobilization of SeO_3^{2-} and SeO_4^{2-} is critically important for the remediation of Se contaminated water or soil.

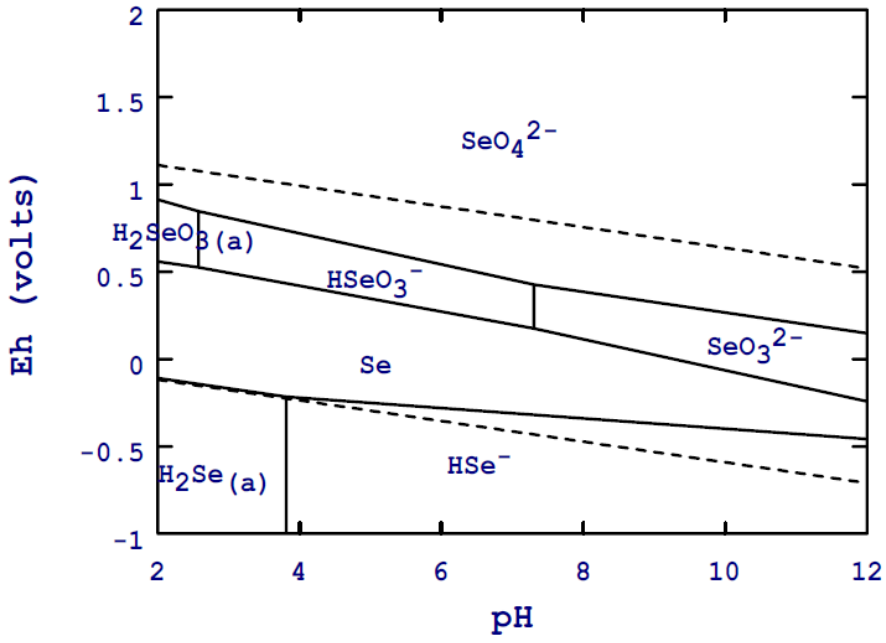

Fig. 1.3 Eh/pH diagram showing the stability regions for various selenium species: 0.050 mg/L Se [132].

As stated above, geopolymer has a low affinity with anionic species. Thus, some other strategies should be adopted. CaO and MgO are commonly adopted as adsorbent, pH regulator, etc. in wastewater treatment, waste-gas cleaning, solid waste disposal, and soil remediation [60, 133-136]. The combination of aluminosilicate oxides and alkaline-earth metal oxides for the synthesis of geopolymer might benefit for the immobilization of anionic species because some other phases might be formed except geopolymer. This expectation could be found in the case of slag-based geopolymer. Hydrotalcite has been confirmed to be formed in the slag-based geopolymer paste due to the high content of CaO and MgO in slag, providing the sorption sites for anionic species theoretically [137]. Consequently, it would extend the application of geopolymer in the S/S of anionic pollutants if the anionic-intercalated phases could be incorporated into geopolymer pastes by adding metal oxides such as CaO and MgO. On the other hand, iron-based materials

including zero-valent iron (ZVI) or ferrous salts are environmentally friendly and inexpensive reagents, and they have been extensively studied and widely used for in-situ and ex-situ environmental remediations [138, 139]. However, the ferric coating on the surface of ZVI is always the biggest obstacle for its long-time application [140, 141]. For ferrous salts such as ferrous sulfate or ferrous chloride, they have been commonly used in wastewater treatment [142]. Furthermore, Fe^{2+} can be simultaneously a reductant, so Fe(II)-adsorbed montmorillonite or calcite, green rust, pyrite, etc. have been tested for the reduction of selenate and/or selenite [143-147]. The addition of ferrous salt into aluminosilicate oxide reaction or alkaline-earth metal oxide hydration might be a possible approach to enhance the remediation efficiencies.

1.6 Research basis for the thesis

The studies in the thesis have been done based on the previously published works (**Table 1.2**), even though these works are not included in the main chapters of the thesis. A brief explanation would be given to make connections with the chapter contents of the thesis. Coal fly ash as a widely used material for the synthesis of geopolymer was examined for the leaching of anionic species, and the results showed that many anions including SeO_4^{2-}, SeO_3^{2-}, $B(OH)_4^-$, AsO_4^{3-}, etc. can be easily leached out [22]. Then, the pozzolanic reaction was adopted to suppress these anionic species leaching by adding calcium minerals. The leaching behaviors of the majority of anions except Se can be effectively suppressed through precipitation or encapsulation [134]. Thereafter, the applications of fly ash for the synthesis of zeolite or calcium silicate hydrate were also conducted for the stabilization process [148, 149]. Then, geopolymer was also synthesized

from fly ash to complete the solidification of spent adsorbent [149]. In addition, in order to characterize the amorphous structure of geopolymer, the structural analysis of geopolymer after adsorption of various cationic radioactive surrogates (Li^+, Cs^+, Sr^{2+}, and Co^{2+}) was studied and compared [150]. Furthermore, the effect of the Si/Al molar ratio on the immobilization of Cs^+ was explored, and it has been confirmed that a low ratio can benefit for the immobilization of cations [151]. In order to immobilize anionic species, Fe(II)-modified geopolymer was prepared. The results showed that approximately 0.16 mmol/g As can be achieved by the modified geopolymer. This provided useful information for S/S of anions using geopolymer-based materials. Based on these preliminary explorations, the works in each chapter of this thesis have been proposed and completed, as shown in **Fig. 1.4**.

Table 1.2 Previous published works related to the thesis.

Title	Author	Published journal	Year	DOI
Distributions and Leaching Behaviors of Toxic Elements in Fly Ash	Quanzhi Tian Binglin Guo Shingo Nakama Keiko Sasaki	ACS Omega	2018	https://doi.org/10.1021/acsomega.8b02096
Reduction of undesirable element leaching from fly ash by adding hydroxylated calcined dolomite	Quanzhi Tian Binglin Guo Shingo Nakama Li Zhang Zhaochu Hu Keiko Sasaki	Waste Management	2019	https://doi.org/10.1016/j.wasman.2019.01.027
Characterizations of calcium silicate hydrates derived from coal fly ash and their mechanisms for phosphate removal	Quanzhi Tian Keiko Sasaki	Desalination and Water Treatment	2019	https://doi:10.5004/dwt.2019.24135
Application of fly ash-based materials for stabilization/solidification of cesium and strontium	Quanzhi Tian Keiko Sasaki	Environmental Science and Pollution Research	2019	https://doi.org/10.1007/s11356-019-05612-1
Application of fly ash-based geopolymer for removal of cesium, strontium and arsenate from aqueous solutions: kinetic, equilibrium and mechanism analysis	Quanzhi Tian Keiko Sasaki	Water Science & Technology	2019	https://doi.org/10.2166/wst.2019.209

Structural characterizations of fly ash-based geopolymer after adsorption of various metal ions	Quanzhi Tian Keiko Sasaki	Environmental Technology	2019	https://doi.org/10.1080/09593330.2019.1649469
Immobilization of cesium in fly ash-silica fume based geopolymers with different Si/Al molar ratios	Quanzhi Tian Shingo Nakama Keiko Sasaki	Science of the Total Environment	2019	https://doi.org/10.1016/j.scitotenv.2019.06.095
Suppression processes of anionic pollutants released from fly ash by various Ca additives	Binglin Guo Shingo Nakama Quanzhi Tian Niko Dian Pahlevi Zhaochu Hu Keiko Sasaki	Journal of Hazardous Materials	2019	https://doi.org/10.1016/j.jhazmat.2019.03.036
Stabilization of borate by hot isostatic pressing after co-precipitation with hydroxyapatite using MAP	Keiko Sasaki Yoshikazu Hayashi Takeshi Nakamura Binglin Guo Quanzhi Tian	Chemosphere	2020	https://doi.org/10.1016/j.chemosphere.2020.126860

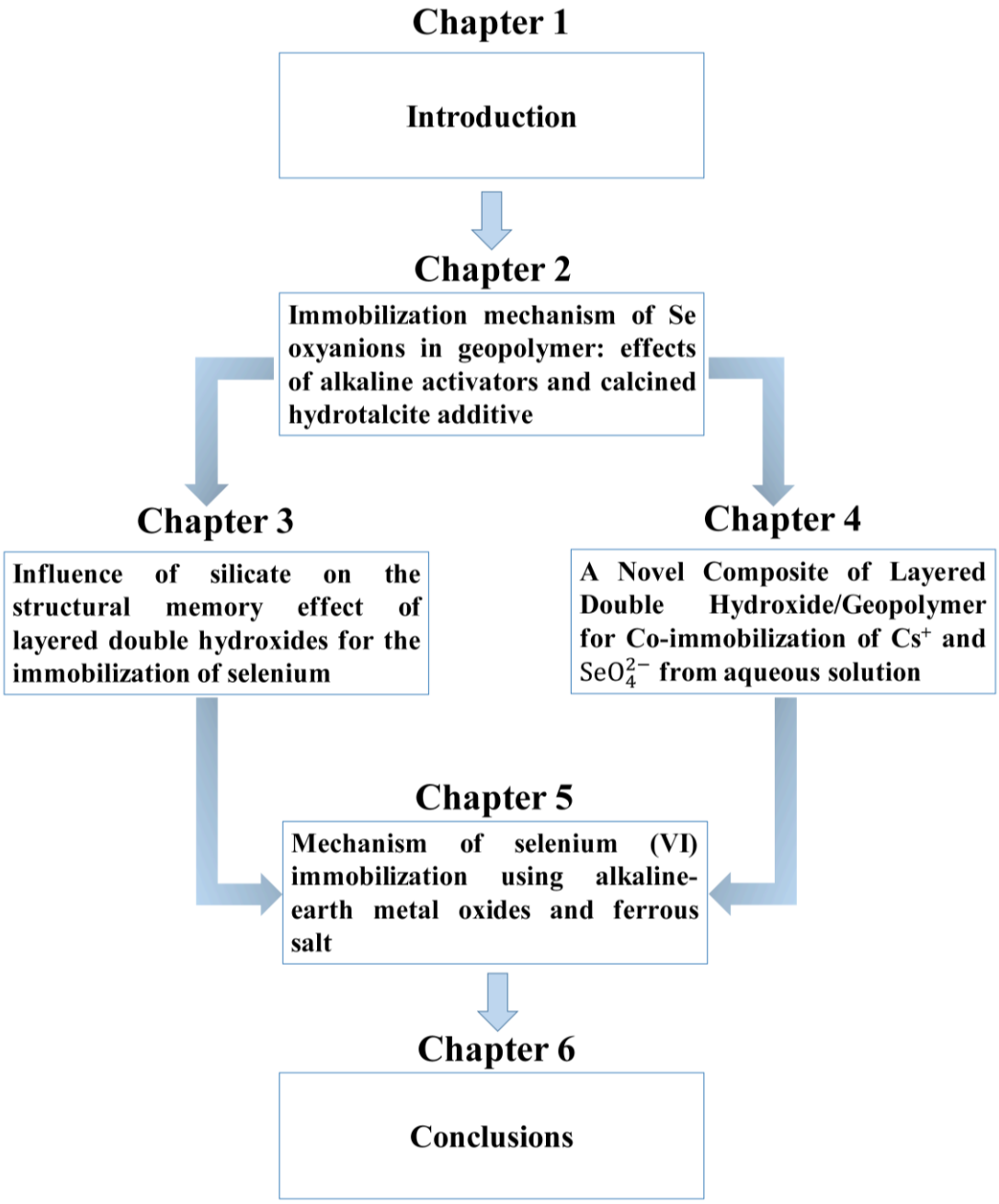

Fig. 1.4 Schematic flowsheet of the thesis structure.

1.7 Objectives and outline of the thesis

Based on the above illustration, geopolymers as a kind of inorganic polymers have been attracted increasing attention as a new civil engineering material. By now, few studies about the immobilization of anionic species using geopolymer have been reported. On the other hand, Se pollution has been a serious problem as illustrated above. Therefore, the objective of the thesis is to immobilize Se oxyanions using geopolymer. Some additives such as metal oxides were added into geopolymer paste to improve the S/S efficiencies. Furthermore, the specific immobilization mechanisms of Se oxyanions in geopolymer were explored. The outline of the thesis is as follows:

The background information about hazardous waste pollution, the policies for solid waste treatment, and treatment techniques were reviewed in **Chapter 1**. The different materials including cement, ceramic, and geopolymer used for S/S treatment were summarized and compared. Based on the above statement, the objectives of the thesis were specified. Furthermore, a summary of methodologies was presented in **Chapter 2**.

Firstly, the immobilization of Se oxyanions was investigated using metakaolin-based geopolymers in **Chapter 3**. The effects of alkaline activator and calcined hydrotalcite on the Se leaching behaviors and the mechanical properties of geopolymer blocks were investigated. Furthermore, the corresponding immobilization mechanisms of Se were discussed and proposed via characterizations including TCLP, XAFS, NMR, XRD, TG, etc.

Based on the observed phenomenon in **Chapter 3**, the influence of silicate on the structural memory effect of layered double hydroxides (LDHs) was studied in **Chapter 4**. Briefly, five types of calcined LDHs (CLDHs) were synthesized and

adopted as sorbents for the sorption of selenium in the presence/absence of silicate ions, under the initial pH 10 and 13, respectively. Moreover, different reaction behaviors occurred to these CLDHs, and accordingly reaction mechanisms were specified.

The synthesis of a novel composite of layered double hydroxide/geopolymer (LDH/GEO) for the co-sorption of Cs^+ and SeO_4^{2-} was demonstrated in **Chapter 5**, also based on the phenomenon found in **Chapter 3**. Furthermore, the sorption of Cs^+ and SeO_4^{2-} by LDH and geopolymer were also conducted to make a comparison with the composite.

The materials including metakaolin, calcined hydrotalcite, fly ash, etc. used for the synthesis of geopolymer can be regarded as the mixture of oxides. Thus, in order to improve the S/S performance using geopolymer, some strategies should be adopted. For the preliminary exploration, **Chapter 6** presents the work about the immobilization of Se(VI) using metal oxides and ferrous salt. To get a better understanding of the immobilization mechanism, this work was designed outside the geopolymer reaction system. Furthermore, the specific mechanism was deeply discussed and proposed.

Chapter 7 summarized the main conclusions of the thesis and suggestions for future research.

References

[1] A.N. Jerry, Solid-waste management, New York: Encyclopedia Britannica, Inc, 2015.

[2] D. Who, Waste production must peak this century, Nature, 502 (2013) 31.

[3] E. Aprianti, P. Shafigh, S. Bahri, J.N. Farahani, Supplementary cementitious materials origin from agricultural wastes–A review, Construction and Building Materials, 74 (2015) 176-187.

[4] P. Kinnunen, A. Ismailov, S. Solismaa, H. Sreenivasan, M.-L. Räisänen, E. Levänen, M. Illikainen, Recycling mine tailings in chemically bonded ceramics–a review, Journal of Cleaner Production, 174 (2018) 634-649.

[5] R. Salemdeeb, E.K. zu Ermgassen, M.H. Kim, A. Balmford, A. Al-Tabbaa, Environmental and health impacts of using food waste as animal feed: a comparative analysis of food waste management options, Journal of Cleaner Production, 140 (2017) 871-880.

[6] M.-S. Wei, K.-H. Huang, Recycling and reuse of industrial wastes in Taiwan, Waste Management, 21 (2001) 93-97.

[7] Y. Liu, W. Lu, H. Guo, Z. Ming, C. Wang, S. Xu, Y. Liu, H. Wang, Aromatic compound emissions from municipal solid waste landfill: Emission factors and their impact on air pollution, Atmospheric Environment, 139 (2016) 205-213.

[8] J. Kapelewska, U. Kotowska, J. Karpińska, A. Astel, P. Zieliński, J. Suchta, K. Algrzym, Water pollution indicators and chemometric expertise for the assessment of the impact of municipal solid waste landfills on groundwater located in their area, Chemical Engineering Journal, 359 (2019) 790-800.

[9] X. Zhang, H. Yang, Z. Cui, Evaluation and analysis of soil migration and distribution characteristics of heavy metals in iron tailings, Journal of Cleaner Production, 172 (2018) 475-480.

[10] N. Raman, D.S. Narayanan, Impact of solid waste effect on ground water and soil quality nearer to Pallavaram solid waste landfill site in Chennai, Rasayan J. Chem, 1 (2008) 828-836.

[11] J.O. Duruibe, M. Ogwuegbu, J. Egwurugwu, Heavy metal pollution and human biotoxic effects, International Journal of Physical Sciences, 2 (2007) 112-118.

[12] Q. Yang, Z. Li, X. Lu, Q. Duan, L. Huang, J. Bi, A review of soil heavy metal pollution from industrial and agricultural regions in China: pollution and risk assessment, Science of the Total Environment, 642 (2018) 690-700.

[13] J. Dong, Q.-w. Yang, L.-n. Sun, Q. Zeng, S.-j. Liu, J. Pan, X.-l. Liu, Assessing the concentration and potential dietary risk of heavy metals in vegetables at a Pb/Zn mine site, China, Environmental Earth Sciences, 64 (2011) 1317-1321.

[14] Z. Li, Z. Ma, T.J. van der Kuijp, Z. Yuan, L. Huang, A review of soil heavy metal pollution from mines in China: pollution and health risk assessment, Science of the Total Environment, 468 (2014) 843-853.

[15] X. Zhang, L. Yang, Y. Li, H. Li, W. Wang, B. Ye, Impacts of lead/zinc mining and smelting on the environment and human health in China, Environmental Monitoring and Assessment, 184 (2012) 2261-2273.

[16] H. Li, N. Luo, Y.W. Li, Q.Y. Cai, H.Y. Li, C.H. Mo, M.H. Wong, Cadmium in rice: transport mechanisms, influencing factors, and minimizing measures, Environmental Pollution, 224 (2017) 622-630.

[17] M.-J. Kang, Y.K. Kwon, S. Yu, P.-K. Lee, H.-S. Park, N. Song, Assessment of Zn pollution sources and apportionment in agricultural soils impacted by a Zn smelter in South Korea, Journal of Hazardous materials, 364 (2019) 475-487.

[18] S. Hou, N. Zheng, L. Tang, X. Ji, Y. Li, X. Hua, Pollution characteristics, sources, and health risk assessment of human exposure to Cu, Zn, Cd and Pb pollution in urban street dust across China between 2009 and 2018, Environment International, 128 (2019) 430-437.

[19] A. Karimi, G.H. Haghnia, T. Safari, H. Hadadian, Lithogenic and anthropogenic pollution assessment of Ni, Zn and Pb in surface soils of Mashhad plain, northeastern Iran, Catena, 157 (2017) 151-162.

[20] F. Edition, Guidelines for drinking-water quality, WHO Chronicle, 38 (2011) 104-108.

[21] Y. He, Y. Xiang, Y. Zhou, Y. Yang, J. Zhang, H. Huang, C. Shang, L. Luo, J. Gao, L. Tang, Selenium contamination, consequences and remediation techniques in water and soils: a review, Environmental Research, 164 (2018) 288-301.

[22] Q. Tian, B. Guo, S. Nakama, K. Sasaki, Distributions and Leaching Behaviors of Toxic Elements in Fly Ash, ACS Omega, 3 (2018) 13055-13064.

[23] S. Jiang, M. He, L. Diao, J. Guo, S. Wu. Remeasurement of the half-life of 79Se with the projectile X-ray detection method. Chinese Physics Letters, 18 (2001): 746-748.

[24] B. Guo, K. Sasaki, T. Hirajima, Selenite and selenate uptaken in ettringite: Immobilization mechanisms, coordination chemistry, and insights from structure, Cement and Concrete Research, 100 (2017) 166-175.

[25] E. Kumar, A. Bhatnagar, W. Hogland, M. Marques, M. Sillanpää, Interaction of anionic pollutants with Al-based adsorbents in aqueous media – A review, Chemical Engineering Journal, 241 (2014) 443-456.

[26] J. Singh, I. Ordoñez, Resource recovery from post-consumer waste: important lessons for the upcoming circular economy, Journal of Cleaner Production, 134 (2016) 342-353.

[27] T. Sterr, T. Ott, The industrial region as a promising unit for eco-industrial development—reflections, practical experience and establishment of innovative instruments to support industrial ecology, Journal of Cleaner Production, 12 (2004) 947-965.

[28] N.E. Altun, C. Xiao, J.-Y. Hwang, Separation of unburned carbon from fly ash using a concurrent flotation column, Fuel Processing Technology, 90 (2009) 1464-1470.

[29] F. Zhou, C. Yan, H. Wang, S. Zhou, H. Liang, The result of surfactants on froth flotation of unburned carbon from coal fly ash, Fuel, 190 (2017) 182-188.

[30] J.C. Hower, J.G. Groppo, U.M. Graham, C.R. Ward, I.J. Kostova, M.M. Maroto-Valer, S. Dai, Coal-derived unburned carbons in fly ash: A review, International Journal of Coal Geology, 179 (2017) 11-27.

[31] A. Akcil, C. Erust, C.S. Gahan, M. Ozgun, M. Sahin, A. Tuncuk, Precious metal recovery from waste printed circuit boards using cyanide and non-cyanide lixiviants – A review, Waste Management, 45 (2015) 258-271.

[32] W. Liu, X. Chen, W. Li, Y. Yu, K. Yan, Environmental assessment, management and utilization of red mud in China, Journal of Cleaner Production, 84 (2014) 606-610.

[33] S. Qin, B. Wu, Effect of self-glazing on reducing the radioactivity levels of red mud based ceramic materials, Journal of Hazardous Materials, 198 (2011) 269-274.

[34] N.L. Nemerow, Zero pollution for industry: Waste minimization through industrial complexes, John Wiley & Sons 1995.

[35] N.P. Cheremisinoff, Handbook of solid waste management and waste minimization technologies, Butterworth-Heinemann 2003.

[36] M.A. Chaaban, Hazardous waste source reduction in materials and processing technologies, Journal of Materials Processing Technology, 119 (2001) 336-343.

[37] A. Kumar, S.R. Samadder, A review on technological options of waste to energy for effective management of municipal solid waste, Waste Management, 69 (2017) 407-422.

[38] N. Scarlat, V. Motola, J. Dallemand, F. Monforti-Ferrario, L. Mofor, Evaluation of energy potential of municipal solid waste from African urban areas, Renewable and Sustainable Energy Reviews, 50 (2015) 1269-1286.

[39] J. Becker, C. Ponce, J. Rodríguez, D. Vázquez, H. Ponce, Can crush: An automated waste compacting system for public areas, 2017 IEEE Mexican Humanitarian Technology Conference (MHTC), IEEE, 2017, pp. 149-152.

[40] C. Visvanathan, Hazardous waste disposal, Resources, Conservation and Recycling, 16 (1996) 201-212.

[41] S. Renou, J.G. Givaudan, S. Poulain, F. Dirassouyan, P. Moulin, Landfill leachate treatment: Review and opportunity, Journal of Hazardous Materials, 150 (2008) 468-493.

[42] C. Shi, A. Fernández-Jiménez, Stabilization/solidification of hazardous and radioactive wastes with alkali-activated cements, Journal of Hazardous Materials, 137 (2006) 1656-1663.

[43] Q. Chen, M. Tyrer, C.D. Hills, X. Yang, P. Carey, Immobilisation of heavy metal in cement-based solidification/stabilisation: a review, Waste Management, 29 (2009) 390-403.

[44] J. Kiventerä, K. Piekkari, V. Isteri, K. Ohenoja, P. Tanskanen, M. Illikainen, Solidification/stabilization of gold mine tailings using calcium sulfoaluminate-belite cement, Journal of Cleaner Production, 239 (2019) 118008.

[45] C. Fan, B. Wang, T. Zhang, Review on Cement Stabilization/Solidification of Municipal Solid Waste Incineration Fly Ash, Advances in Materials Science and Engineering, (2018) 5120649.

[46] F. Glasser, Fundamental aspects of cement solidification and stabilisation, Journal of Hazardous Materials, 52 (1997) 151-170.

[47] B. Guo, B. Liu, J. Yang, S. Zhang, The mechanisms of heavy metal immobilization by cementitious material treatments and thermal treatments: A review, Journal of Environmental Management, 193 (2017) 410-422.

[48] G. Laforest, J. Duchesne, Immobilization of chromium (VI) evaluated by binding isotherms for ground granulated blast furnace slag and ordinary Portland cement, Cement and Concrete Research, 35 (2005) 2322-2332.

[49] R. Bie, P. Chen, X. Song, X. Ji, Characteristics of municipal solid waste incineration fly ash with cement solidification treatment, Journal of the Energy Institute, 89 (2016) 704-712.

[50] T.M. Clancy, K.V. Snyder, R. Reddy, A. Lanzirotti, S.E. Amrose, L. Raskin, K.F. Hayes, Evaluating the cement stabilization of arsenic-bearing iron wastes from drinking water treatment, Journal of Hazardous Materials, 300 (2015) 522-529.

[51] S.R. Mallampati, Y. Mitoma, T. Okuda, S. Sakita, M. Kakeda, Enhanced heavy metal immobilization in soil by grinding with addition of nanometallic Ca/CaO dispersion mixture, Chemosphere, 89 (2012) 717-723.

[52] M. Lasheras-Zubiate, I. Navarro-Blasco, J.M. Fernández, J.I. Álvarez, Encapsulation, solid-phases identification and leaching of toxic metals in cement systems modified by natural biodegradable polymers, Journal of Hazardous Materials, 233-234 (2012) 7-17.

[53] D. Dermatas, X. Meng, Utilization of fly ash for stabilization/solidification of heavy metal contaminated soils, Engineering Geology, 70 (2003) 377-394.

[54] L. Wang, D.-W. Cho, D.C.W. Tsang, X. Cao, D. Hou, Z. Shen, D.S. Alessi, Y.S. Ok, C.S. Poon, Green remediation of As and Pb contaminated soil using cement-free clay-based stabilization/solidification, Environment International, 126 (2019) 336-345.

[55] S.A. Walling, J.L. Provis, Magnesia-Based Cements: A Journey of 150 Years, and Cements for the Future?, Chemical Reviews, 116 (2016) 4170-4204.

[56] M. Jianli, Z. Youcai, W. Jinmei, W. Li, Effect of magnesium oxychloride cement on stabilization/solidification of sewage sludge, Construction and Building Materials, 24 (2010) 79-83.

[57] Y.-S. Wang, J.-G. Dai, L. Wang, D.C. Tsang, C.S. Poon, Influence of lead on stabilization/solidification by ordinary Portland cement and magnesium phosphate cement, Chemosphere, 190 (2018) 90-96.

[58] Y. Su, J. Yang, D. Liu, S. Zhen, N. Lin, Y. Zhou, Effects of municipal solid waste incineration fly ash on solidification/stabilization of Cd and Pb by magnesium potassium phosphate cement, Journal of Environmental Chemical Engineering, 4 (2016) 259-265.

[59] Z.-h. Qian, X.-y. Liu, Y.-b. Qiao, S. Wang, Q. Qin, L.-q. Shi, H.-h. Peng, Effect of fluorine on stabilization/solidification of radioactive fluoride liquid waste in magnesium potassium phosphate cement, Journal of Radioanalytical and Nuclear Chemistry, 319 (2019) 393-399.

[60] L. Wang, L. Chen, D.-W. Cho, D.C. Tsang, J. Yang, D. Hou, K. Baek, H.W. Kua, C.-S. Poon, Novel synergy of Si-rich minerals and reactive MgO for stabilisation/solidification of contaminated sediment, Journal of Hazardous Materials, 365 (2019) 695-706.

[61] A. Viani, A.F. Gualtieri, Preparation of magnesium phosphate cement by recycling the product of thermal transformation of asbestos containing wastes, Cement and Concrete Research, 58 (2014) 56-66.

[62] S. Fan, B. Chen, Experimental study of phosphate salts influencing properties of magnesium phosphate cement, Construction and Building Materials, 65 (2014) 480-486.

[63] X.-F. Chen, S.-C. Kou, F. Xing, Effect of Agriculture and Construction Wastes on the Properties of Magnesium Oxychloride Cement Mortar with Tourmaline Powder, Materials, 12 (2019) 115.

[64] F.-J. Zhang, X.-Y. Sun, X. Li, D. Zhang, W.-J. Xie, J. Liu, W.-C. Oh, F.-J. Zhang, X.-Y. Sun, X. Li, Study on Water Resistance of Environmentally Friendly

Magnesium Oxychloride Cement for Waste Wood Solidification, Journal of the Korean Ceramic Society, 55 (2018) 446-451.

[65] P. He, C.S. Poon, D.C. Tsang, Comparison of glass powder and pulverized fuel ash for improving the water resistance of magnesium oxychloride cement, Cement and Concrete Composites, 86 (2018) 98-109.

[66] I. Navarro-Blasco, A. Duran, R. Sirera, J. Fernández, J.I. Alvarez, Solidification/stabilization of toxic metals in calcium aluminate cement matrices, Journal of Hazardous Materials, 260 (2013) 89-103.

[67] S. Lamberet, Durability of ternary binders based on Portland cement, calcium aluminate cement and calcium sulfate, EPFL, 2004.

[68] P. Swift, H. Kinoshita, N. Collier, C. Utton, Phosphate modified calcium aluminate cement for radioactive waste encapsulation, Advances in Applied Ceramics, 112 (2013) 1-8.

[69] H. Fryda, G. Vetter, R. Ollitrault-Fichet, P. Boch, A. Capmas, Formation of chabazite in mixes of calcium aluminate cement and silica fume used for caesium immobilization, Advances in Cement Research, 8 (1996) 29-39.

[70] R.C. Ewing, Long-term storage of spent nuclear fuel, Nature Materials, 14 (2015) 252-257.

[71] W. Lee, M. Ojovan, M. Stennett, N. Hyatt, Immobilisation of radioactive waste in glasses, glass composite materials and ceramics, Advances in Applied Ceramics, 105 (2006) 3-12.

[72] M. Chrysochoou, D. Dermatas, Evaluation of ettringite and hydrocalumite formation for heavy metal immobilization: literature review and experimental study, Journal of Hazardous Materials, 136 (2006) 20-33.

[73] M. Lupsea, L. Tiruta-Barna, N. Schiopu, Leaching of hazardous substances from a composite construction product–An experimental and modelling approach for fibre-cement sheets, Journal of Hazardous Materials, 264 (2014) 236-245.

[74] E.-T. Tolonen, T. Hu, J. Rämö, U. Lassi, The removal of sulphate from mine water by precipitation as ettringite and the utilisation of the precipitate as a sorbent for arsenate removal, Journal of Environmental Management, 181 (2016) 856-862.

[75] X. Qiu, K. Sasaki, Y. Takaki, T. Hirajima, K. Ideta, J. Miyawaki, Mechanism of boron uptake by hydrocalumite calcined at different temperatures, Journal of Hazardous Materials, 287 (2015) 268-277.

[76] A. Moore, H. Taylor, Crystal structure of ettringite, Acta Crystallographica Section B: Structural Crystallography and Crystal Chemistry, 26 (1970) 386-393.

[77] B. Guo, K. Sasaki, T. Hirajima, Characterization of the intermediate in formation of selenate-substituted ettringite, Cement and Concrete Research, 99 (2017) 30-37.

[78] B. Guo, Y. Xiong, W. Chen, S.A. Saslow, N. Kozai, T. Ohnuki, I. Dabo, K. Sasaki, Spectroscopic and First-Principles Investigations of Iodine Species Incorporation into Ettringite: Implications for Iodine Migration in Cement Waste Forms, Journal of Hazardous Materials, (2019) 121880.

[79] S. Periyasamy, N. Viswanathan, Hydrothermal synthesis of hydrocalumite assisted biopolymeric hybrid composites for efficient Cr(VI) removal from water, New Journal of Chemistry, 42 (2018) 3371-3382.

[80] K.S. You, J.W. Ahn, H.C. Cho, G.C. Han, D.Y. Han, K.H. Cho, Competing ion effect of stabilization by Cr (III) & Cr (VI) in ettringite crystal structure, Solid State Phenomena, Trans Tech Publ, 2007, pp. 1629-1632.

[81] A. Kindness, A. Macias, F. Glasser, Immobilization of chromium in cement matrices, Waste Management, 14 (1994) 3-11.

[82] A.B. Nasr, K. Walha, F. Puel, D. Mangin, R.B. Amar, C. Charcosset, Precipitation and adsorption during fluoride removal from water by calcite in the presence of acetic acid, Desalination and Water Treatment, 52 (2014) 2231-2240.

[83] L. Delgadillo-Velasco, V. Hernández-Montoya, M.A. Montes-Morán, R.T. Gómez, F.J. Cervantes, Recovery of different types of hydroxyapatite by precipitation of phosphates of wastewater from anodizing industry, Journal of Cleaner Production, 242 (2020) 118564.

[84] M. Le Rouzic, T. Chaussadent, G. Platret, L. Stefan, Mechanisms of k-struvite formation in magnesium phosphate cements, Cement and Concrete Research, 91 (2017) 117-122.

[85] M. Lasheras-Zubiate, I. Navarro-Blasco, J.M. Fernández, J.I. Alvarez, Encapsulation, solid-phases identification and leaching of toxic metals in cement

systems modified by natural biodegradable polymers, Journal of Hazardous Materials, 233 (2012) 7-17.

[86] F. Ziegler, A.M. Scheidegger, C.A. Johnson, R. Dähn, E. Wieland, Sorption mechanisms of zinc to calcium silicate hydrate: X-ray absorption fine structure (XAFS) investigation, Environmental Science & Technology, 35 (2001) 1550-1555.

[87] Y.E. Fakhreldin, Durability of Portland cement with and without metal oxide weighting material in a CO_2/H_2S environment, North Africa Technical Conference and Exhibition, Society of Petroleum Engineers, 2012.

[88] Y. Su, J. Yang, D. Liu, S. Zhen, N. Lin, Y. Zhou, Y. Su, J. Yang, D. Liu, S. Zhen, Solidification/stabilization of simulated cadmium-contaminated wastes with magnesium potassium phosphate cement, Environmental Engineering Research, 21 (2015) 15-21.

[89] Y.-J. Du, M.-L. Wei, K.R. Reddy, F. Jin, H.-L. Wu, Z.-B. Liu, New phosphate-based binder for stabilization of soils contaminated with heavy metals: Leaching, strength and microstructure characterization, Journal of Environmental Management, 146 (2014) 179-188.

[90] J.D. Ortego, Y. Barroeta, F.K. Cartledge, H. Akhter, Leaching effects on silicate polymerization. An FTIR and silicon-29 NMR study of lead and zinc in portland cement, Environmental Science & Technology, 25 (1991) 1171-1174.

[91] B. Johannesson, P. Utgenannt, Microstructural changes caused by carbonation of cement mortar, Cement and Concrete Research, 31 (2001) 925-931.

[92] D. Bonen, S.L. Sarkar, The effects of simulated environmental attack on immobilization of heavy metals doped in cement-based materials, Journal of Hazardous Materials, 40 (1995) 321-335.

[93] B.-T. Huang, Q.-H. Li, S.-L. Xu, Fatigue deformation model of plain and fiber-reinforced concrete based on Weibull function, Journal of Structural Engineering, 145 (2019) 04018234.

[94] W. Chen, J. Hong, C. Xu, Pollutants generated by cement production in China, their impacts, and the potential for environmental improvement, Journal of Cleaner Production, 103 (2015) 61-69.

[95] C. Chen, G. Habert, Y. Bouzidi, A. Jullien, Environmental impact of cement production: detail of the different processes and cement plant variability evaluation, Journal of Cleaner Production, 18 (2010) 478-485.

[96] G.S. Ryu, Y.B. Lee, K.T. Koh, Y.S. Chung, The mechanical properties of fly ash-based geopolymer concrete with alkaline activators, Construction and Building Materials, 47 (2013) 409-418.

[97] P. Rożek, M. Król, W. Mozgawa, Spectroscopic studies of fly ash-based geopolymers, Spectrochimica Acta Part A: Molecular and Biomolecular Spectroscopy, 198 (2018) 283-289.

[98] H.Y. Zhang, V. Kodur, B. Wu, L. Cao, F. Wang, Thermal behavior and mechanical properties of geopolymer mortar after exposure to elevated temperatures, Construction and Building Materials, 109 (2016) 17-24.

[99] G. Roviello, L. Ricciotti, C. Ferone, F. Colangelo, O. Tarallo, Fire resistant melamine based organic-geopolymer hybrid composites, Cement and Concrete Composites, 59 (2015) 89-99.

[100] J.G. Jang, S.M. Park, H.-K. Lee, Physical barrier effect of geopolymeric waste form on diffusivity of cesium and strontium, Journal of Hazardous Materials, 318 (2016) 339-346

[101] Y.-M. Liew, C.-Y. Heah, H. Kamarudin, Structure and properties of clay-based geopolymer cements: A review, Progress in Materials Science, 83 (2016) 595-629.

[102] P. Duxson, A. Fernández-Jiménez, J.L. Provis, G.C. Lukey, A. Palomo, J.S. van Deventer, Geopolymer technology: the current state of the art, Journal of Materials Science, 42 (2007) 2917-2933.

[103] J. Davidovits, Properties of geopolymer cements, First international conference on alkaline cements and concretes, Kiev State Technical University, Ukraine: Scientific Research Institute on Binders and Materials, 1994, pp. 131-149.

[104] H. Zain, M.M.A.B. Abdullah, K. Hussin, N. Ariffin, R. Bayuaji, Review on various types of geopolymer materials with the environmental impact assessment, MATEC Web of Conferences, EDP Sciences, 2017, pp. 01021.

[105] S. Ahmari, L. Zhang, Durability and leaching behavior of mine tailings-based geopolymer bricks, Construction and Building Materials, 44 (2013) 743-750.

[106] J. He, Y. Jie, J. Zhang, Y. Yu, G. Zhang, Synthesis and characterization of red mud and rice husk ash-based geopolymer composites, Cement and Concrete Composites, 37 (2013) 108-118.

[107] P. Duxson, J.L. Provis, Designing precursors for geopolymer cements, Journal of the American Ceramic Society, 91 (2008) 3864-3869.

[108] L. Tchadjie, S. Ekolu, Enhancing the reactivity of aluminosilicate materials toward geopolymer synthesis, Journal of Materials Science, 53 (2018) 4709-4733.

[109] A. Elimbi, H. Tchakoute, D. Njopwouo, Effects of calcination temperature of kaolinite clays on the properties of geopolymer cements, Construction and Building Materials, 25 (2011) 2805-2812.

[110] M. Abdullah, H. Kamarudin, M. Bnhussain, I. Khairul Nizar, A.R. Rafiza, Y. Zarina, The relationship of NaOH molarity, Na_2SiO_3/NaOH ratio, fly ash/alkaline activator ratio, and curing temperature to the strength of fly ash-based geopolymer, Advanced Materials Research, Trans Tech Publ, 2011, pp. 1475-1482.

[111] R. Abdul Rahim, T. Rahmiati, K.A. Azizli, Z. Man, M.F. Nuruddin, L. Ismail, Comparison of using NaOH and KOH activated fly ash-based geopolymer on the mechanical properties, Materials Science Forum, Trans Tech Publ, 2015, pp. 179-184.

[112] Z. Ji, Y. Pei, Bibliographic and visualized analysis of geopolymer research and its application in heavy metal immobilization: A review, Journal of Environmental Management, 231 (2019) 256-267.

[113] U. EPA, Method 1311. Toxicity characteristic leaching procedure, US Environmental Protection Agency Washington, DC, USA, 1992.

[114] X. Guo, W. Hu, H. Shi, Microstructure and self-solidification/stabilization (S/S) of heavy metals of nano-modified CFA–MSWIFA composite geopolymers, Construction and Building Materials, 56 (2014) 81-86.

[115] B. El-Eswed, R. Yousef, M. Alshaaer, I. Hamadneh, S. Al-Gharabli, F. Khalili, Stabilization/solidification of heavy metals in kaolin/zeolite based geopolymers, International Journal of Mineral Processing, 137 (2015) 34-42.

[116] R.A.A.B. Santa, C. Soares, H.G. Riella, Geopolymers with a high percentage of bottom ash for solidification/immobilization of different toxic metals, Journal of Hazardous Materials, 318 (2016) 145-153.

[117] X. Guo, L. Zhang, J. Huang, H. Shi, Detoxification and solidification of heavy metal of chromium using fly ash-based geopolymer with chemical agents, Construction and Building Materials, 151 (2017) 394-404.

[118] Y. Wang, F. Han, J. Mu, Solidification/stabilization mechanism of Pb (II), Cd (II), Mn (II) and Cr (III) in fly ash based geopolymers, Construction and Building Materials, 160 (2018) 818-827.

[119] Q. Li, Z. Sun, D. Tao, Y. Xu, P. Li, H. Cui, J. Zhai, Immobilization of simulated radionuclide $^{133}Cs^{+}$ by fly ash-based geopolymer, Journal of Hazardous Materials, 262 (2013) 325-331.

[120] Q. Yu, S. Li, H. Li, X. Chai, X. Bi, J. Liu, T. Ohnuki, Synthesis and characterization of Mn-slag based geopolymer for immobilization of Co, Journal of Cleaner Production, 234 (2019): 97-104.

[121] Z. Yunsheng, S. Wei, C. Qianli, C. Lin, Synthesis and heavy metal immobilization behaviors of slag based geopolymer, Journal of Hazardous Materials, 143 (2007) 206-213.

[122] T. Sun, J. Chen, X. Lei, C. Zhou, Detoxification and immobilization of chromite ore processing residue with metakaolin-based geopolymer, Journal of Environmental Chemical Engineering, 2 (2014) 304-309.

[123] A. Al-Mashqbeh, S. Abuali, B. El-Eswed, F.I. Khalili, Immobilization of toxic inorganic anions ($Cr_2O_7^{2-}$, MnO_4^- and $Fe(CN)_6^{3-}$) in metakaolin based geopolymers: A preliminary study, Ceramics International, 44 (2018) 5613-5620.

[124] I. Lancellotti, E. Kamseu, M. Michelazzi, L. Barbieri, A. Corradi, C. Leonelli, Chemical stability of geopolymers containing municipal solid waste incinerator fly ash, Waste Management, 30 (2010) 673-679.

[125] B. Guo, B. Liu, A.A. Volinsky, M. Fincan, J. Du, S. Zhang, Immobilization mechanism of Pb in fly ash-based geopolymer, Construction and Building Materials, 134 (2017) 123-130.

[126] X. Huang, T. Huang, S. Li, F. Muhammad, G. Xu, Z. Zhao, L. Yu, Y. Yan, D. Li, B. Jiao, Immobilization of chromite ore processing residue with alkali-

activated blast furnace slag-based geopolymer, Ceramics International, 42 (2016) 9538-9549.

[127] Q.T. Dinh, Z. Cui, J. Huang, T.A.T. Tran, D. Wang, W. Yang, F. Zhou, M. Wang, D. Yu, D. Liang, Selenium distribution in the Chinese environment and its relationship with human health: a review, Environment International, 112 (2018) 294-309.

[128] S. Etteieb, S. Magdouli, M. Zolfaghari, S. Brar, Monitoring and analysis of selenium as an emerging contaminant in mining industry: A critical review, Science of the Total Environment, (2019) 134339.

[129] Y. Wang, Y. Wang, L. Zhang, L. Chen, Z. Liu, X. Yin, D. Sheng, J. Diwu, J. Wang, N. Liu, Substitutional disorder of SeO_3^{2-}/IO_3^- in the crystalline solid matrix: insights into the fate of radionuclides ^{79}Se and ^{129}I in the environment, Inorganic Chemistry, 56 (2017) 3702-3708.

[130] B. Guo, K. Sasaki, T. Hirajima, Solidification of ettringite after uptaking selenate as a surrogate of radionuclide in glass-ceramics by using industrial by-products, Journal of Materials Science, 52 (2017) 12999-13011.

[131] W. Xie, Q. Liang, T. Qian, D. Zhao, Immobilization of selenite in soil and groundwater using stabilized Fe–Mn binary oxide nanoparticles, Water Research, 70 (2015) 485-494.

[132] L. Twidwell, J. McCloskey, H. Joyce, E. Dahlgren, A. Hadden, Removal of selenium oxyanions from mine waters utilizing elemental iron and galvanically coupled metals, Proceedings of the Jan D. Mill Symposium—Innovations in Natural Resource, Salt Lake City, UT, USA, 2005, pp. 299-313.

[133] R. Li, J.J. Wang, B. Zhou, Z. Zhang, S. Liu, S. Lei, R. Xiao, Simultaneous capture removal of phosphate, ammonium and organic substances by MgO impregnated biochar and its potential use in swine wastewater treatment, Journal of Cleaner Production, 147 (2017) 96-107.

[134] Q. Tian, B. Guo, S. Nakama, L. Zhang, Z. Hu, K. Sasaki, Reduction of undesirable element leaching from fly ash by adding hydroxylated calcined dolomite, Waste Management, 86 (2019) 23-35.

[135] X. Wang, W. Zeng, M. Song, F. Wang, X. Hu, Q. Guo, Y. Liu, Polyetheramine improves the CO_2 adsorption behavior of tetraethylenepentamine-functionalized sorbents, Chemical Engineering Journal, 364 (2019) 475-484.

[136] Z. Jin, Y. Jia, K.-S. Zhang, L.-T. Kong, B. Sun, W. Shen, F.-L. Meng, J.-H. Liu, Effective removal of fluoride by porous MgO nanoplates and its adsorption mechanism, Journal of Alloys and Compounds, 675 (2016) 292-300.

[137] T. Yang, X. Yao, Z. Zhang, Quantification of chloride diffusion in fly ash–slag-based geopolymers by X-ray fluorescence (XRF), Construction and Building Materials, 69 (2014) 109-115.

[138] M. Qiu, M. Wang, Q. Zhao, B. Hu, Y. Zhu, XANES and EXAFS investigation of uranium incorporation on nZVI in the presence of phosphate, Chemosphere, 201 (2018) 764-771.

[139] C. Tang, Y. Huang, Z. Zhang, J. Chen, H. Zeng, Y.H. Huang, Rapid removal of selenate in a zero-valent iron/Fe_3O_4/Fe^{2+} synergetic system, Applied Catalysis B: Environmental, 184 (2016) 320-327.

[140] F. Obiri-Nyarko, S.J. Grajales-Mesa, G. Malina, An overview of permeable reactive barriers for in situ sustainable groundwater remediation, Chemosphere, 111 (2014) 243-259.

[141] C. Tang, Y.H. Huang, H. Zeng, Z. Zhang, Reductive removal of selenate by zero-valent iron: The roles of aqueous Fe^{2+} and corrosion products, and selenate removal mechanisms, Water Research, 67 (2014) 166-174.

[142] A.S. Adeleye, J.R. Conway, K. Garner, Y. Huang, Y. Su, A.A. Keller, Engineered nanomaterials for water treatment and remediation: Costs, benefits, and applicability, Chemical Engineering Journal, 286 (2016) 640-662.

[143] S. Chakraborty, F. Bardelli, L. Charlet, Reactivities of Fe (II) on calcite: selenium reduction, Environmental Science & Technology, 44 (2010) 1288-1294.

[144] S. Myneni, T.K. Tokunaga, G. Brown, Abiotic selenium redox transformations in the presence of Fe (II, III) oxides, Science, 278 (1997) 1106-1109.

[145] A.C. Scheinost, L. Charlet, Selenite reduction by mackinawite, magnetite and siderite: XAS characterization of nanosized redox products, Environmental Science & Technology, 42 (2008) 1984-1989.

[146] A.G. Ilgen, J.N. Kruichak, K. Artyushkova, M.G. Newville, C. Sun, Redox transformations of As and Se at the surfaces of natural and synthetic ferric nontronites: role of structural and adsorbed Fe (II), Environmental Science & Technology, 51 (2017) 11105-11114.

[147] N. Börsig, A.C. Scheinost, S. Shaw, D. Schild, T. Neumann, Retention and multiphase transformation of selenium oxyanions during the formation of magnetite via iron (II) hydroxide and green rust, Dalton Transactions, 47 (2018) 11002-11015.

[148] Q. Tian, K. Sasaki, Characterizations of calcium silicate hydrates derived from coal fly ash and their mechanisms for phosphate removal, Desalination and Water Treatment, 156 (2019) 78-86.

[149] Q. Tian, K. Sasaki, Application of fly ash-based materials for stabilization/solidification of cesium and strontium, Environmental Science and Pollution Research, (2019) 1-13.

[150] Q. Tian, K. Sasaki, Structural characterizations of fly ash-based geopolymer after adsorption of various metal ions, Environmental Technology, (2019) 1-11.

[151] Q. Tian, S. Nakama, K. Sasaki, Immobilization of cesium in fly ash-silica fume based geopolymers with different Si/Al molar ratios, Science of the Total Environment, 687 (2019) 1127-1137.

Chapter 2

Methodology

2.1 Characterizations

2.1.1 Solution analysis

The concentrations of elements in solutions were determined using an inductively coupled plasma optical emission spectrometry (ICP-OES, Perkin Elmer, Optima 8300, US) and an inductively coupled plasma mass spectrometry (ICP-MS, Agilent 7500ce, US).

2.1.2 X-ray diffraction

X-ray diffraction (XRD) was used to characterize the phases of the samples, and the XRD patterns were collected on a Rigaku Ultima IV XRD (Akishima, Japan): Cu Kα (40 kV, 40 mA) with a Ni filter at a scanning speed of 2° min^{-1} and scanning step of 0.02°. According to the database from the International Centre for Diffraction Data (ICDD-PDF), the phase identifies were achieved using diffraction analysis software PDXL (Rigaku).

2.1.3 X-ray fluorescence spectroscopy

X-ray fluorescence (XRF) was adopted to determine the elemental compositions of the samples using a Rigaku ZSX Primus II (Akishima, Japan) in the wavelength dispersive mode: Rh-anode (3 or 4 kV, 60 kV).

2.1.4 Scanning electron microscope and Energy-dispersive X-ray spectroscopy

The morphologies and elemental distributions of the prepared samples were observed on a scanning electron microscopy (SEM, VE-9800, Keyence), with the accelerating voltage of 20 kV. As for the sample preparation, the sample was firstly

fixed on carbon tape, then Au or C coating was conducted through the magnetron sputtering machine.

2.1.5 X-ray photoelectron spectroscopy

X-ray photoelectron spectroscopy (XPS) was adopted to determine the chemical states of solid samples, conducted on an ESCA 5800 (ULVAC-PHI, Inc., Kanagawa, Japan) using a monochromated Al Kα X-ray source. The binding energy of C1s = 284.6 eV for adventitious carbon was adopted to calibrate the binding energies. The Casa XPS software (version 2.3.12.8) was used for the data analysis.

2.1.6 Fourier Transform Infrared Spectrometer and Raman

The chemical bonds of the prepared samples were indicated by the Fourier transform infrared (FTIR) spectra (4000–400 cm^{-1}) which was recorded by an FTIR spectrometer (JASCO 670 Plus, Japan) with a resolution of 4 cm^{-1} using samples diluted with KBr. In addition, Raman spectra were collected using a DXR Smart Raman spectrometer (Thermo Scientific, US) in the of 4000-100 cm^{-1} region, utilizing a 532 nm light source.

2.1.7 Nitrogen adsorption-desorption isotherm

N_2 adsorption-desorption curves were measured using a high-precision surface area and pore size distribution analyzer (BEL-Max, BEL, Japan) at – 196 ℃. Pretreatment under vacuum at certain temperatures for several hours was conducted to remove adsorbed gas and water. The specific surface areas were calculated based on

Brunauer-Emmett-Teller method (BET method), and pore size distributions were calculated based on Barrett-Joyner-Halenda method (BJH method).

2.1.8 Thermogravimetric analysis

Thermogravimetric analysis (TG-DTA, 2000 SA thermal balance, Bruker, Germany) or was used to determine the weight loss of the samples. Heating rate and nitrogen flows were 10 °C/min and 100 $mL \cdot min^{-1}$, respectively.

2.1.9 Solid State Nuclear Magnetic Resonance

^{27}Al solid-state nuclear magnetic resonance (NMR) spectra of geopolymer samples were collected on an ECA 800 (JEOL Ltd., Akishima, Japan) spectrometer at 18.80 T (B_0) using 3.2 nm multi-quantum magic angle spinning (MQMAS) probes and a single pulse method, yielding a resonance frequency of 208.5 MHz. Typical acquisition parameters involved a spinning speed of 250 kHz, a pulse length of 13 μs, and a relaxation delay of 1 s. ^{29}Si NMR spectra of geopolymer samples were acquired on an ECA 400 (JEOL Ltd., Akishima, Japan) equipped with a 3.2 mm cross-polarization (CP) MAS. The field strength and resonance frequency were 9.39 T and 79.4 MHz, respectively. Moreover, the relaxation delay was 10 s and a π/2-pulse length of 3.375 μs was also used.

2.1.10 X-ray absorption fine structure

X-ray absorption fine structure (XAFS) spectra of Se-K edge of solid residues were collected on a beamline-06 in the SAGA Light Source (Saga, Japan). The energy range of the light source is 2.1–23 keV, and the typical photon flux is 10^{10} photons/s.

The electron storage ring operated at an energy of 1.4 GeV, and a silicon (111) double-crystal monochromator was used to obtain the incident X-ray beam. The Se-K edge was collected in the transmission mode and the absorption edge of each Se K-edge spectrum was calibrated to 12675 eV. Each sample was measured in three loops to increase the data quality. Meanwhile, XAFS spectra of known reference materials including Na_2SeO_3 and Na_2SeO_4 were also measured on the beamline. Data processing was carried out on the ATHENA [1-4].

2.2 Leaching methods

To evaluate the immobilization performance of Se in geopolymer, the toxicity characteristic leaching procedure (TCLP) was used [5]. Specifically, acetic acid solutions (pH = 2.88 and 4.93) required in TCLP and another two extractants including pure water and sulfuric acid-nitric acid solution (pH=3.2) were adopted for the leaching tests. The liquid/solid ratio was fixed to 20:1 (L:kg), shaking at 30 rpm for 18 h.

References

[1] B. Ravel, M. Newville, ATHENA and ARTEMIS: interactive graphical data analysis using IFEFFIT, Physica Scripta, 115 (2005) 537–541

[2] M. Newville, IFEFFIT: interactive XAFS analysis and FEFF fitting, Journal of synchrotron radiation, 8 (2001) 322-324.

[3] B. Ravel, M. Newville, ATHENA, ARTEMIS, HEPHAESTUS: data analysis for X-ray absorption spectroscopy using IFEFFIT, Journal of synchrotron radiation, 12 (2005) 537-541.

[4] A. Ankudinov, B. Ravel, J. Rehr, S. Conradson, Real-space multiple-scattering calculation and interpretation of x-ray-absorption near-edge structure, Physical Review B, 58 (1998) 7565.

[5] U. EPA, Method 1311. Toxicity characteristic leaching procedure, US Environmental Protection Agency Washington, DC, USA, 1992.

Chapter 3

Immobilization mechanism of Se oxyanions in geopolymer: Effects of alkaline activators and calcined hydrotalcite additive

3.1 Introduction

Geopolymer has been attracted increasing attention as a new civil engineering material [1]. It has been viewed as the new kind of cement following lime and ordinary Portland cement (OPC) because of its higher strength, better heat resistance, better resistance to acids and sulfate, less CO_2 emission [2, 3]. S/S using geopolymer as the binder has been widely applied to cationic pollutants including Cs^{+}, Pb^{2+}, Sr^{2+}, Co^{2+}, Cd^{2+}, Zn^{2+}, Cu^{2+}, Cr^{3+}, etc. [4-9]. However, there are few reports about the immobilization of anionic species using geopolymer. Al-Mashqbeh, et al. [10] utilized metakaolin-based geopolymers to immobilize the inorganic anions ($Cr_2O_7^{2-}$, MnO_4^{-} and $Fe(CN)_6^{3-}$) and concluded that the geopolymer had limited capacity for the immobilization of metal anions. Nikolić, et al. [11] employed fly ash-based geopolymers to immobilize Cr(VI) and found that geopolymer pastes containing 0.5–2.0% Cr cannot meet the requirement of landfill due to the high leaching concentration. The permanent negative charge of geopolymer structure always has the repulsive force to these anionic species, and this could be the main reason for the poor performance of S/S of anionic species using geopolymers. Traditionally, the S/S process is implemented using OPC as the binder [12, 13]. The hydration products including ettringite and hydrocalumite are the main holders to immobilize anionic species in the cement-based S/S process [14-18]. Consequently, it would definitely extend the application of geopolymer in the S/S of anionic pollutants if the anionic-intercalated phases could be incorporated into geopolymer pastes. Layered double hydroxides (LDHs) have been widely investigated for adsorption/immobilization of anions including $B(OH)_4^{-}$, AsO_3^{3-}, AsO_4^{3-}, SeO_3^{2-}, SeO_4^{2-}, etc. [19-22]. Based on the main components of geopolymer (Si and Al), MgAl-LDH could be the possible candidate

which might be formed in geopolymer paste. On the other hand, the precursor for geopolymer synthesis is mainly silicon/aluminum oxides in an amorphous form (e.g. metakaolin). Thus, based on the above hypothesis, the calcined hydrotalcite was added into the precursor for geopolymer synthesis. In this investigation, two kinds of activators (NaOH and Na_2SiO_3) were adopted for geopolymer synthesis. Leaching performance was evaluated by the toxicity characteristic leaching procedure (TCLP). Furthermore, XRD, FTIR, TG, NMR, XAFS, and N_2 adsorption-desorption isotherm were used to indicate specific immobilization mechanisms.

3.2 Experimental

3.2.1 Materials

Metakaolin (MK) was obtained by calcining kaolin (purchased from Wako, Osaka, Japan) at 700 ℃ for 12 h, and the silica fume was purchased from Tomoe company in Japan. The amorphous aluminosilicate in metakaolin was quantified by the quantitative X-ray diffraction (QXRD) to be 71.40%. In addition, the calcined hydrotalcite (CHT) was obtained by calcination of hydrotalcite ($Mg_6Al_2(OH)_{16}CO_3 \cdot 4H_2O$, Wako) at 500 ℃ for 3 h. The mineralogical and elemental compositions of them are shown in **Fig. 3.1** and **Table 3.1**, respectively. The chemicals used in this study included sodium hydroxide (97%, Wako), sodium silicate solution (17.5% Na_2O, 37% SiO_2, Chameleon), sodium selenite (97%, Wako), sodium selenate (97%, Wako).

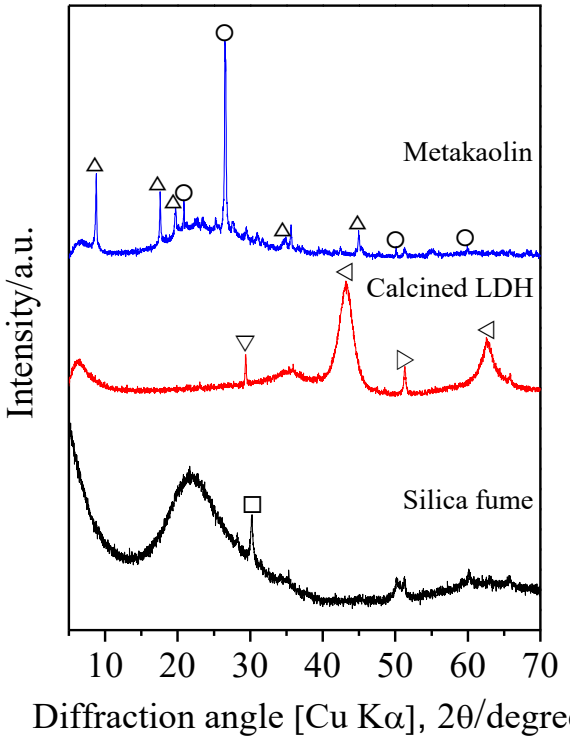

Fig. 3.1 XRD patterns of raw materials used for geopolymer synthesis. Symbols: ○, Quartz (SiO_2); △, Muscovite ($(K_{0.82}Na_{0.18})(Fe_{0.03}Al_{1.97})(AlSi_3)O_{10}(OH)_2$); ◁, Magnesium aluminum oxide ($MgAl_2O_4$); ▽, Magnesium oxide (MgO); ▷, Aluminum oxide (Al_2O_3); □, Zirconium oxide (ZrO_2).

Table 3.1 Chemical compositions of raw materials (by XRF, %).

Sample	SiO_2	Al_2O_3	K_2O	Fe_2O_3	MgO	Others
Metakaolin	52.04	43.97	2.42	1.09	0.25	0.24
Silica fume	96.67	0.33	0.04	0.40	-	2.56
Calcined hydrotalcite	-	29.82	-	-	70.18	-

3.2.2 Sample preparation

Metakaolin was used for geopolymer synthesis, and the Si/Al molar ratio of geopolymer was adjusted to 2 by adding silica fume. Two kinds of activated solutions were prepared by deionized water (18.2 Ω): 10 M NaOH solution and sodium silicate solution (SiO_2: 22.89%, Na_2O: 17.91%, adjusted by NaOH). According to the composition of precursor powder in **Table 3.2**, the geopolymer samples (named as S1~S12) were prepared as the following procedure: firstly, precursor powder and

activator were mechanically mixed and stirred for 10 min. Then, the mixture was cast into the cylindrical mold with a diameter of 2 cm and a height of 4 cm, vibrated for 5 min to remove bubbles inside the slurry. Thereafter, the prepared samples were sealed and cured for 24 h at room temperature, and then demolded. Subsequently, these pastes were moved to an incubator with a humidity of 93±2% and temperature of 25 ± 2 ℃ for another 27 days. Afterward, the geopolymer samples were firstly measured in terms of uniaxial compressive strength, and after that stored for further analysis.

Table 3.2 Mixture formulations (g) for geopolymer pastes.

Sample	MK	Silica fume	CHT	Activitor 1	Activitor 2	Na_2SeO_3	Na_2SeO_4
S1	8.5720	3.4280	-	9.60	-	-	-
S2	7.7148	3.0852	1.20	9.60	-	-	-
S3	8.5720	3.4280	-	9.60	-	0.5419	-
S4	7.7148	3.0852	1.20	9.60	-	0.5419	-
S5	8.5720	3.4280	-	9.60	-		0.5920
S6	7.7148	3.0852	1.20	9.60	-		0.5920
S7	10.1984	1.8016	-	-	9.60	-	-
S8	9.3412	1.4587	1.20	-	9.60	-	-
S9	10.1984	1.8016	-	-	9.60	0.5419	-
S10	9.3412	1.4587	1.20	-	9.60	0.5419	-
S11	10.1984	1.8016	-	-	9.60		0.5920
S12	9.3412	1.4587	1.20	-	9.60		0.5920

Note: Activator 1, 10 M NaOH solution; Activator 2, Na_2SiO_3 solution (SiO_2: 22.89%, Na_2O: 17.91%).

3.2.3 Leaching test and solid characterizations

To evaluate the immobilization performance of Se in geopolymer, the TCLP test was conducted [23]. Specifically, acetic acid solutions (pH 2.88 and 4.93) required in TCLP and another two extractants including pure water and sulfuric acid-nitric acid solution (pH 3.2) were adopted for the leaching tests with the liquid/solid ratio of 20:1 (L: kg). Then, supernatants were taken and filtered through 0.2 μm filters after shaking

at 30 rpm for 18 h under room temperature, and stored to determine the remaining Se concentration using an ICP-OES (Optima 8300, US).

The compressive strengths of the obtained specimens were determined using a 200 kN capacity CLP-200KNS1 testing machine (Osaka, Japan). XRD patterns of geopolymer samples were collected on a Rigaku Ultima IV multipurpose diffractometer with a scanning speed of 2 °min^{-1}. FTIR spectra of the samples after diluting by KBr were recorded using a JASCO670 spectrometer with a resolution of 4 cm^{-1}. The thermogravimetric characteristics of geopolymers were studied using a 2000SA thermal balance (TG-DTA, Germany) with the N_2 flow and heating rate of 100 mL/min and 10 ℃/min, respectively. α-Al_2O_3 was adopted as the reference material.

^{27}Al NMR spectra of geopolymer samples were collected on an ECA 800 (Akishima, Japan) spectrometer at 18.80 T (B_0) yielding a resonance frequency of 208.5 MHz. Typical acquisition parameters involved a spinning speed of 250 kHz, a pulse length of 13 μs, and a relaxation delay of 1 s. ^{29}Si NMR spectra of geopolymer samples were recorded on an ECA 400 (Akishima, Japan). The field strength and resonance frequency were 9.39 T and 79.4 MHz, respectively. Moreover, the relaxation delay was 10 s and a π/2-pulse length of 3.375 μs was also used.

X-ray absorption fine structure (XAFS) spectroscopy was adopted to study the associations of Se in geopolymers. The spectra of the Se-K edge of geopolymers and reference materials were recorded in the SAGA Light Source (beamline-06, Tosu, Japan) with the energy range of 2.1-23 keV and typical photon flux of 10^{10} photons/s. Fluorescence mode was used for collecting Se-K edge spectra. Data processing was conducted using ATHENA [24-26].

3.3 Results and discussion

3.3.1 Leaching results

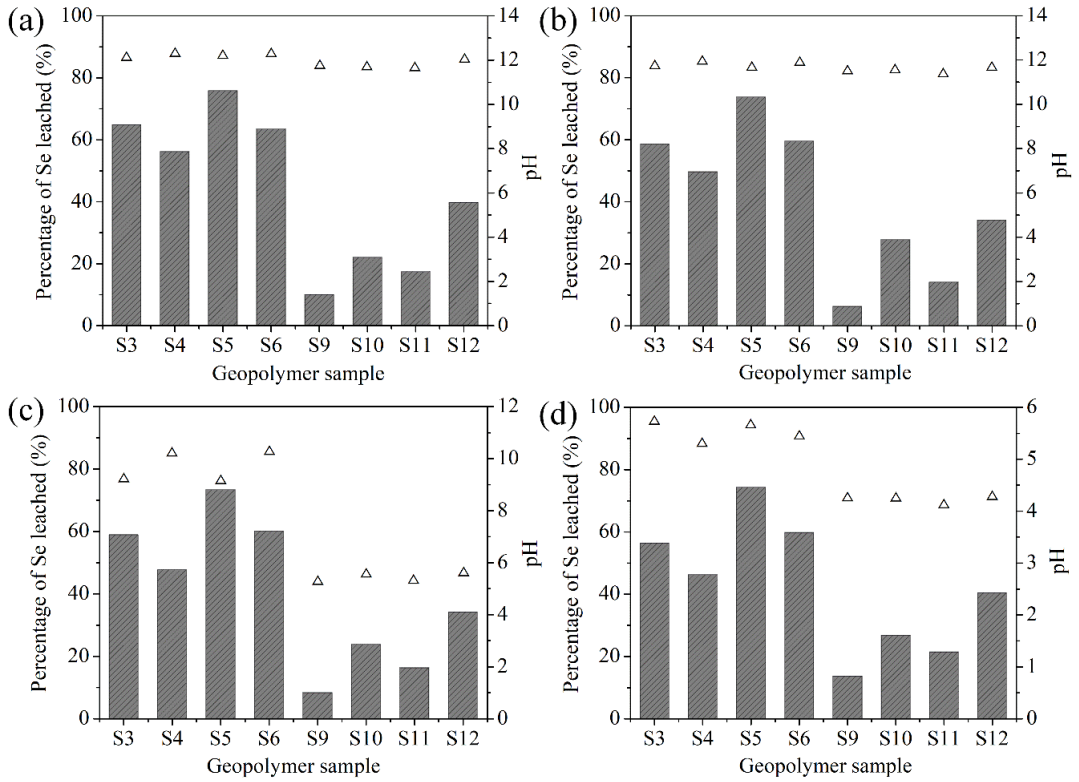

Fig. 3.2 Leaching percentages of Se species from geopolymer samples in the different extracting solutions (left axis for bars) and the final pH (right axis for △): (a) water, (b) sulfuric acid-nitric acid solution (pH 3.2), (c) acetic acid solution (pH 4.93), (d) acetic acid solution (pH 2.88). The error is within ±5%.

The leaching results of Se species from geopolymer samples are shown in **Fig. 3.2**. Obviously, the leaching amount of Se did not present a large variation with regard to different extractants, indicating that the immobilized parts of SeO_3^{2-} and SeO_4^{2-} in geopolymers were very stable in a range of pH from 2.88 to natural pH. As a whole, the leaching fractions of SeO_4^{2-} are a bit higher than that of SeO_3^{2-} in all cases. Na_2SiO_3-based geopolymers showed much lower leaching percentages of SeO_3^{2-} and SeO_4^{2-} (approximately 10% and 18% for S9 and S11, respectively). While, much higher leaching percentages of SeO_3^{2-} and SeO_4^{2-} (approximately 58% and 74% for S3 and S5, respectively) occurred to NaOH-based geopolymers. But the addition of CHT always

decreased leaching percentages of SeO_3^{2-} and SeO_4^{2-} to approximately 50% and 60% for NaOH-activated geopolymers (S4 and S6). By contrast, after adding CHT into the matrixes activated by Na_2SiO_3 (S10 and S12), the leaching percentages of SeO_3^{2-} and SeO_4^{2-} unexpectedly increased to approximately 25% and 37% respectively by comparison with S9 and S11 (without CHT). This might suggest different immobilization mechanisms behind the NaOH- and Na_2SiO_3-geopolymers.

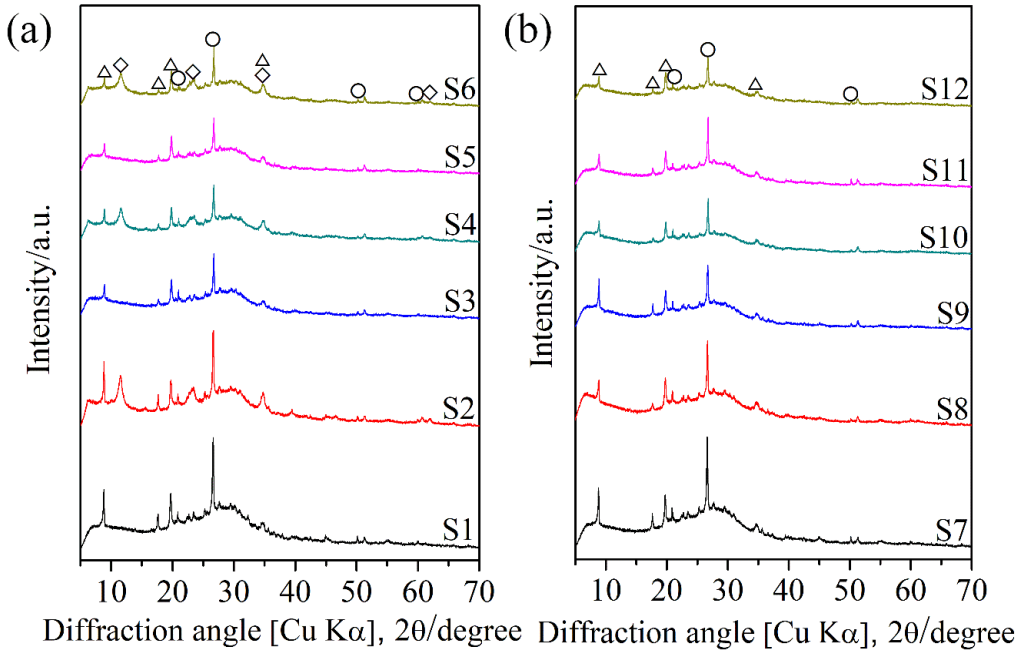

Fig. 3.3 XRD patterns of geopolymer samples (a) S1~S6, (b) S7~S12. Symbol: ○, Quartz (SiO_2); △, Muscovite ($(K_{0.82}Na_{0.18})(Fe_{0.03}Al_{1.97})(AlSi_3)O_{10}(OH)_2$);◇, hydrotalcite-like mineral ($(Mg_{2\sim3}Al(OH)_{6\sim8}(CO_3, SeO_3, SeO_4)_{0.5}.xH_2O$).

3.3.2 Solid characterizations

PXRD patterns of ground geopolymer samples were collected to indicate the phase formations as shown in **Fig. 3.3**. It can be clearly found that quartz and muscovite derived from kaolin exist in all of the samples. The broad peaks at approximately 25-30 degree/2-theta indicated the formation of amorphous geopolymer [8, 27]. The most conspicuous difference between NaOH-based geopolymers (S1~S6)

and Na_2SiO_3-based geopolymers (S7~S12) should be the formation of hydrotalcite. Obviously, the peaks belonging to hydrotalcite appeared in the XRD patterns of S2, S4, and S6 with CHT (**Fig. 3.3a**), and this is definitely the most reasonable evidence for the explanation for the decreased leaching amount of Se. However, there is no additional peak in the XRD patterns of S8, S10, and S12 with CHT (**Fig. 3.3b**). Most of Mg and Al in CHT might be involved in the formations of magnesium silicate hydrate (amorphous) and geopolymer. In addition, there is no new peak assigned to the Se-related phase that appeared in the XRD patterns, which indicates that SeO_3^{2-} or SeO_4^{2-} might exist in other association modes.

The FTIR spectra for each sample are presented in **Fig. 3.4**, and the peak assignments are referred to previous studies [27, 28]. The maximum absorbance in the region of approximately 900-1200 cm^{-1} is assigned to the Si-O-T (T = Si or Al) asymmetric stretching vibration mode. The bending vibration of the OH group is located at approximately 1600-1700 cm^{-1}. The vibrations of Se-O bond in selenite and selenate could be observed at approximately 700-800 cm^{-1} and 900 cm^{-1}, respectively (standard spectra in **Fig. 3.5**). As for the NaOH-based geopolymers, it can be apparently found that there are two peaks of CO_3^{2-} vibration modes at 1470 cm^{-1} (assigned to Na_2CO_3) and at 1388 cm^{-1} (assigned to CO_2^{3-} in LDH) [29, 30]. The band assigned to Na_2CO_3 existed in all of the NaOH-based geopolymers, which was mainly caused by CO_2 contamination. However, there is no clear peak assigned to carbonate ion in the spectra of Na_2SiO_3-based geopolymers without CHT addition. This implies that Na_2SiO_3-activated geopolymers have a higher resistance to CO_2 contamination. For those with the addition of CHT, a broad peak appeared around the position of

carbonate vibrations. This might indicate that there is a part of CO_3^{2-} adsorbed through electrostatic force instead of the formation of Na_2CO_3.

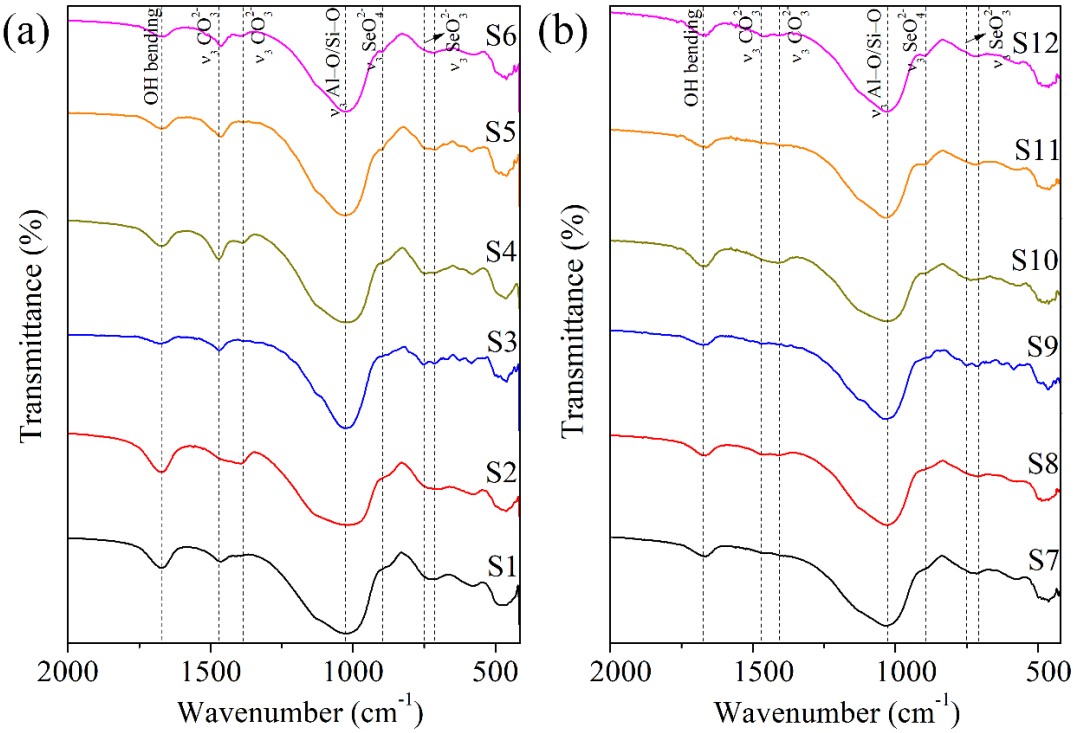

Fig. 3.4 FTIR spectra of geopolymer samples (a) S1~S6, (b) S7~S12.

In order to get an understanding of Se associations in these geopolymers, TG data were collected as presented in **Fig. 3.6**. Apparently, there are several weight losses appeared in the TG curves of NaOH-activated geopolymers (**Fig. 3.6(a, b, c)**): 25-200 ℃ (volatilization of free water), 360-450 ℃ (decomposition of hydroxide layer), 600-750 ℃ (SeO_3^{2-} elimination) and 640-800 ℃ (SeO_4^{2-} elimination) [31, 32]. However, only the weight loss of free water volatilization obviously appeared in the TG curves of Na_2SiO_3-activated geopolymers (**Fig. 3.6(d, e, f)**). XRD results have shown that LDHs are not formed in the Na_2SiO_3-activated geopolymers. Therefore, it is natural to find the non-appearance of weight loss for hydroxide layer decomposition. The absence of the DTG peak for Se elimination seems that most of Se (SeO_3^{2-} or SeO_4^{2-})

might have been encapsulated in the geopolymer structure and then cannot be volatilized.

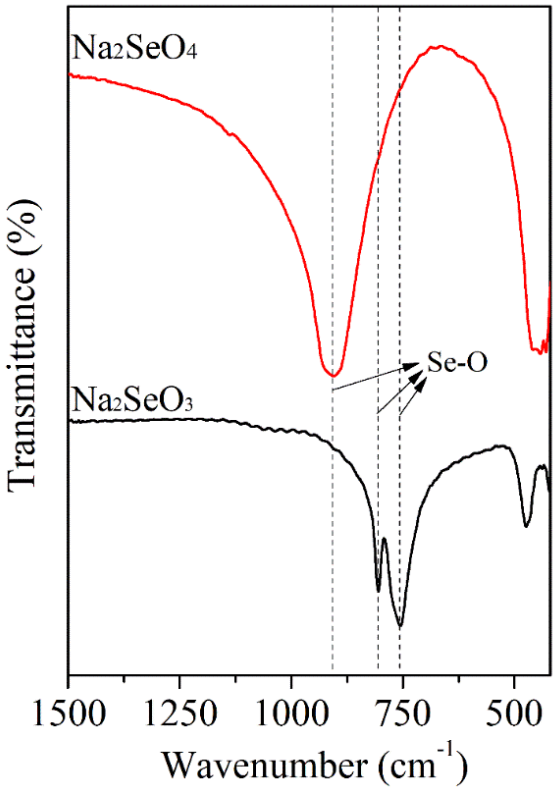

Fig. 3.5 FTIR spectra of sodium selenite and selenate.

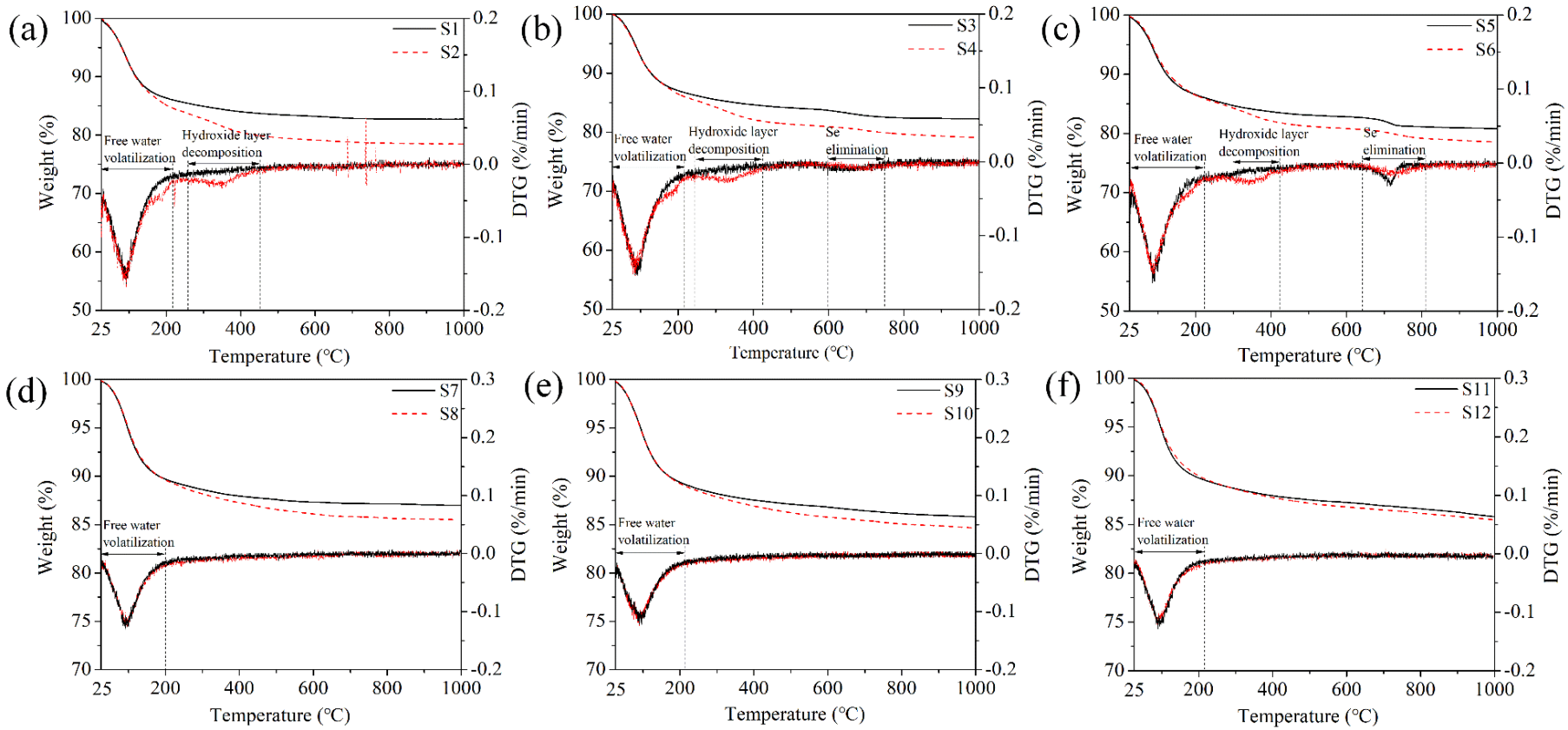

Fig. 3.6 TG-DTG curves of geopolymer samples (a) S1 and S2, (b) S3 and S4, (c) S5 and S6, (d) S7 and S8, (e) S9 and S10, (f) S11 and S12.

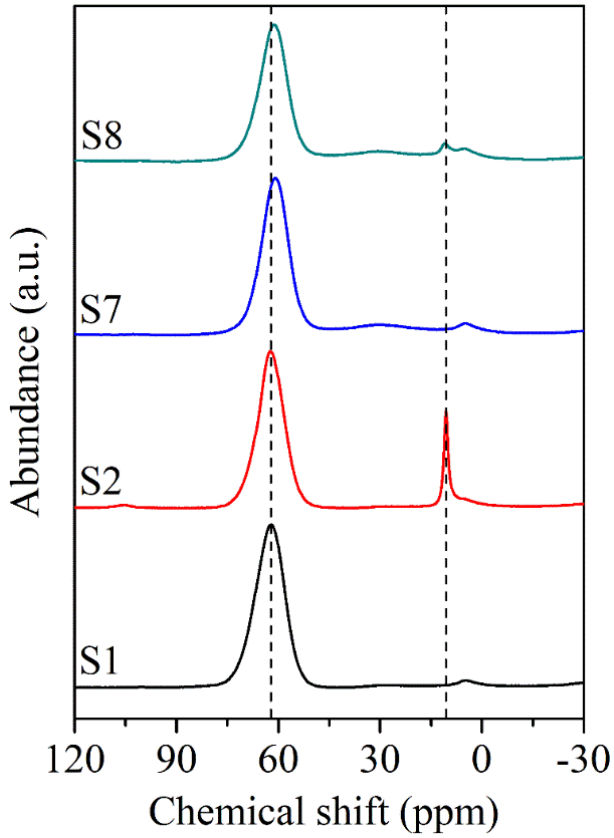

Fig. 3.7 ^{27}Al MAS NMR spectra of geopolymer samples.

^{27}Al and ^{29}Si NMR spectroscopies are extremely useful techniques to explore the coordination of Al or Si in aluminosilicate materials. **Fig. 3.7** represents the ^{27}Al NMR spectra of S1, S2, S7, and S8. Noticeably, a strong resonance signal at 62~60 ppm attributed to the Al in tetrahedral coordination appeared in both NaOH-activated geopolymers (S1 and S2) and Na_2SiO_3-activated geopolymers (S7 and S8). Specifically, the signal at 62~60 ppm represents that most of Al should be coordinated with three or four Si tetrahedrons [33]. Furthermore, it can be clearly seen that the chemical shifts for S7 and S8 at 60.71 and 61.18 ppm were lower than that for S1 and S2 at 62.12 and 62.35 ppm, and this indicated that a larger amount of Al coordinated with four Si tetrahedrons was produced in Na_2SiO_3-activated geopolymers. On the other hand, the distinctive peak at 10.90 ppm in the spectrum of S2 can be assigned to the Al in the octahedral coordination, and this is consistent with the fact of the

existence of LDH in S2 confirmed by XRD (**Fig. 3.3a**). For the sample of S8, there is only a very weak peak assigned to the six-coordinated Al in the spectrum, indicating that most of Al in CHT has been already involved in the formation of geopolymer as the above speculation.

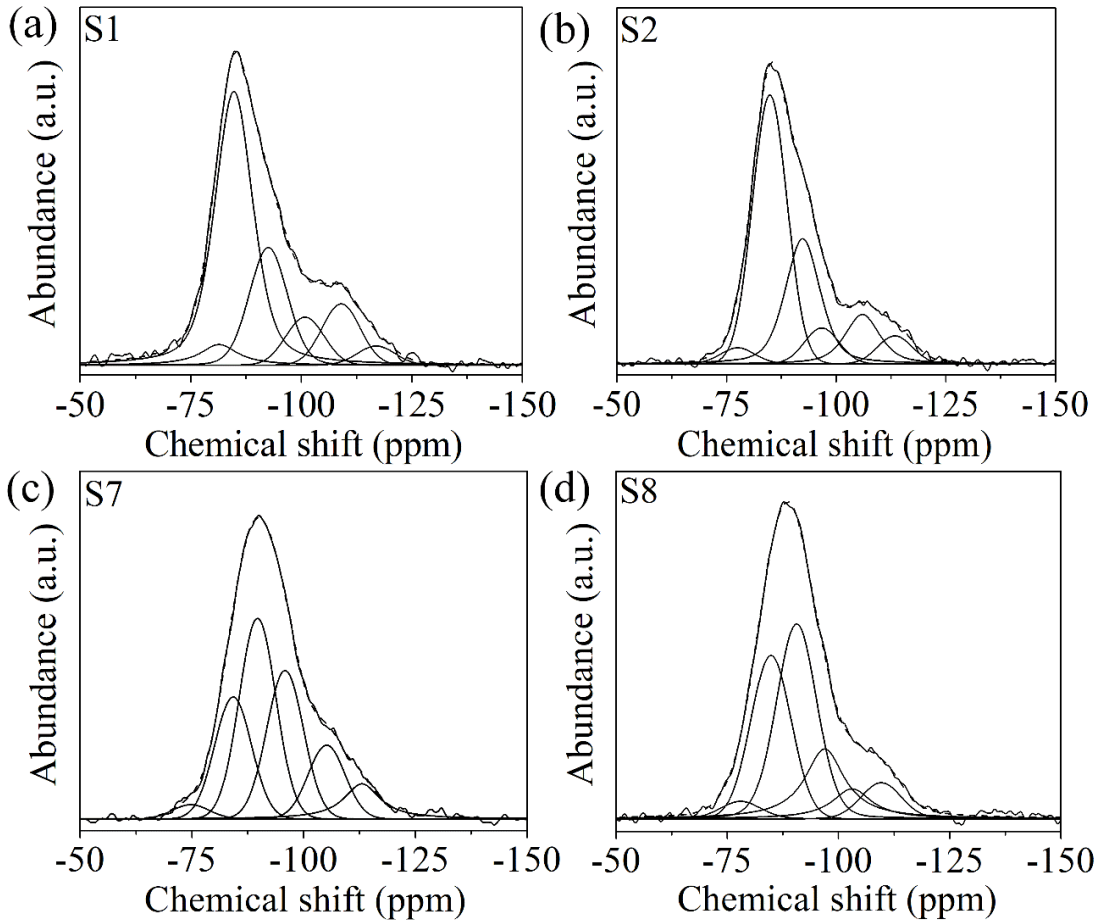

Fig. 3.8 ^{29}Si MAS NMR spectra of geopolymer samples (a) S1, (b) S2, (c) S7, (d) S8. From left to right, there peaks can be assigned to Q^0(or Q^2(1Al)), Q^4(4Al), Q^4(3Al), Q^4(2Al), Q^4(1Al) and Q^4(0Al), respectively.

^{29}Si NMR spectra and their deconvolutions of sample S1, S2, S7, and S8 are shown in **Fig. 3.8**. According to the literatures [34, 35], the peaks centered at approximately – 75~82, – 83~84, – 89~92, – 95~101, – 103~109 and – 105~117 ppm could be assigned to Q^0(or Q^2(1Al)), Q^4(4Al), Q^4(3Al), Q^4(2Al), Q^4(1Al) and Q^4(0Al), respectively. Then, the relative amount of each species is summarized in **Fig. 3.9**. It

can be found that there are large amounts of Q^4(4Al) and Q^4(3Al) existed in the NaOH-activated geopolymers (S1 and S2). However, the fraction of Q^4(4Al) decreased, and the fractions of Q^4(3Al) and Q^4(2Al) greatly increased in Na_2SiO_3-activated geopolymers. Therefore, the Na_2SiO_3-activated geopolymers can be seen as "Si-rich" gels with the comparison with NaOH-activated geopolymers. Furthermore, this can also imply that soluble silicate can be much easier to participate in the formation of geopolymer gel. Generally, the Si-rich gels including Q^4(0Al) and Q^4(1Al) are hardly formed because of the high Al content in MK [1]. Therefore, the fractions of Q^4(0Al) and Q^4(1Al) should be mainly caused by quartz and muscovite. An increase in the fraction of Q^4(0Al) for Na_2SiO_3-activated geopolymers should be due to the soluble silicate in activated solutions.

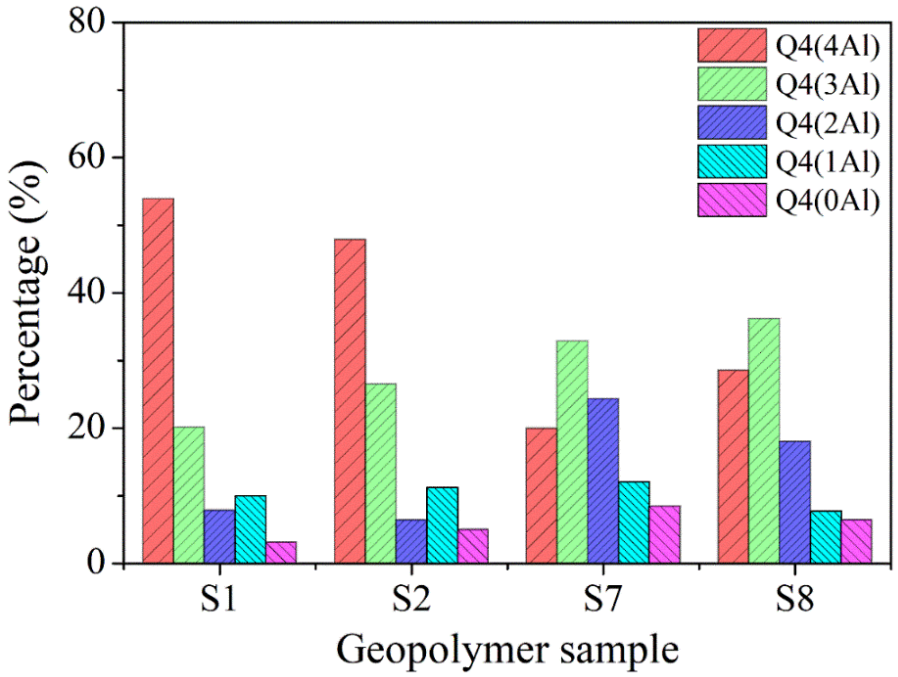

Fig. 3.9 Normalized summary of Q^4(mAl) Si coordination environments in geopolymer samples identified in the deconvoluted ^{29}Si NMR spectra.

3.3.3 Se immobilization mechanisms

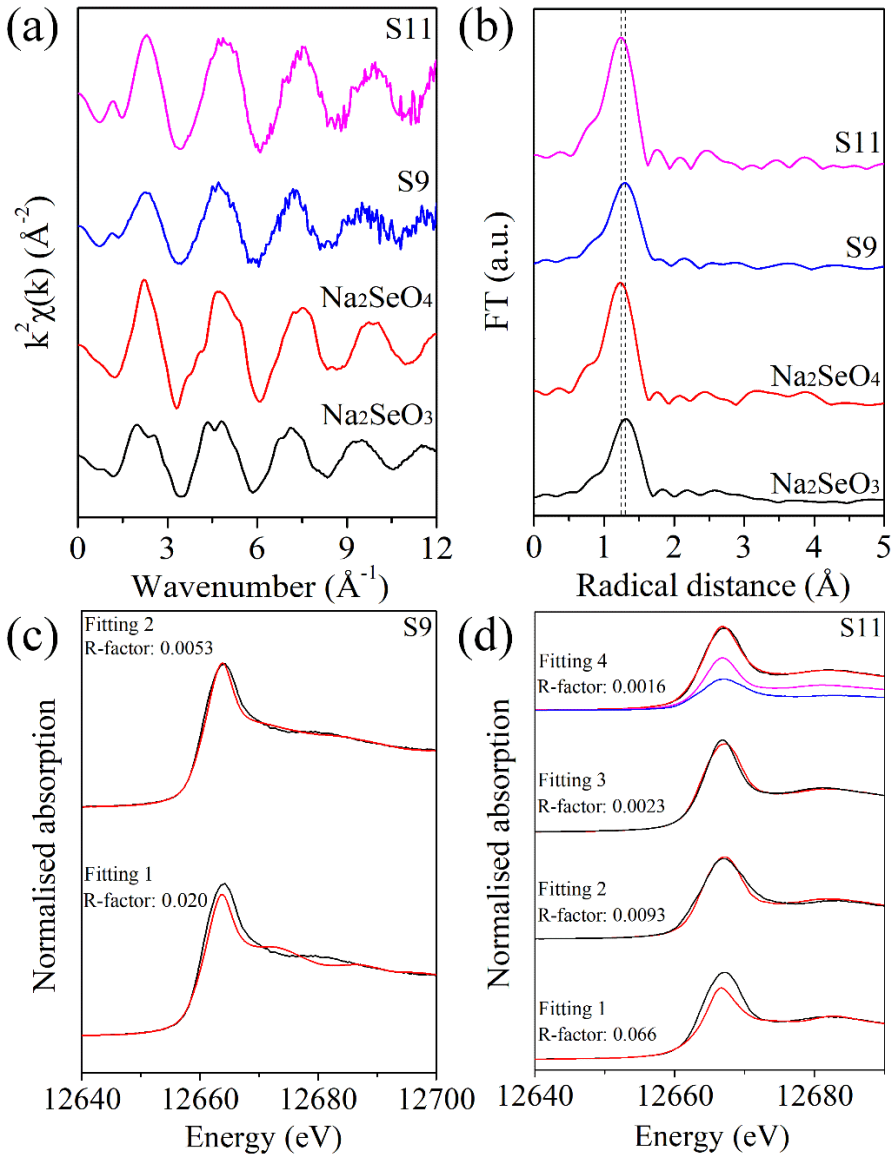

Fig. 3.10 X-ray absorption spectra of S9, S11 and references: Se K-edge EXAFS spectra in k space (a) and R space (b); (c) LCF results for sample S9. Here, the references used in Fitting 1 and Fitting 2 are Na_2SeO_3 and MgFe-Se(IV)-LDH, respectively. (d) LCF results for sample S11. Here, the references used in Fitting 1, 2 and 3 are Na_2SeO_4, Se(VI)-cancrinite and MgAl-Se(VI)-LDH, respectively. In Fitting 4, both Se(VI)-cancrinite and MgAl-Se(VI)-LDH are used for LCF: bule line, Se(VI)-cancrinite; pink line: MgAl-Se(VI)-LDH.

Based on the leaching results, it has been known that Na_2SiO_3-activated geopolymer can achieve much better leaching performance than NaOH-activated geopolymer. Most of SeO_3^{2-} or SeO_4^{2-} has been immobilized in Na_2SiO_3-activated

geopolymers. Moreover, the leaching results have already shown that the CHT additive reduces the Se immobilization ability of geopolymers activated by Na_2SiO_3. In order to further improve the immobilization efficiency, the exploration of the Se immobilization mechanism in Na_2SiO_3-activated geopolymers without CHT addition should be needed. Based on the elemental composition of geopolymer paste (Al, Si, and Na), there should be only three possible associations of SeO_3^{2-} or SeO_4^{2-} including sodium selenite or selenate, electrostatic interaction or connection with Si (or Al) tetrahedron by sharing oxygen in Na_2SiO_3-activated geopolymers without CHT addition. Generally, it is extremely difficult for SeO_3^{2-} or SeO_4^{2-} to connect with the Al or Si tetrahedron even though under high-temperature conditions, due to their distinct structures and charges [36]. Furthermore, the EXAFS spectra of S9, S11 and reference materials in k and R spaces are respectively presented in **Fig. 3.10(a)** and **3.10(b)**. Obviously, the EXAFS spectra of S9 and S11 did not show any evidence of direct coordination of SeO_3^{2-} or SeO_4^{2-} and Na^+ with the comparison of the spectra of Na_2SeO_3 and Na_2SeO_4. In order to further understand immobilization mechanisms of Se, linear combination fitting (LCF) was performed on S9 and S11 (**Fig. 3.10c** and **3.10d**) since the XANES fingerprinting effect can represent the local coordination environment [37, 38]. It can be clearly seen that there are extremely large deviations in the fitting between the spectra of Na_2SeO_3 or Na_2SeO_4 and experimental spectra for S9 and S11, respectively. Thus, it can be excluded that Se (SeO_3^{2-}or SeO_4^{2-}) in S9 and S11 exists in the occurrence of Na_2SeO_3 or Na_2SeO_4. Most of SeO_3^{2-} and SeO_4^{2-} should occur in the association mode of electrostatic interaction in geopolymer samples. The MgAl-LDH and cancrinite containing SeO_4^{2-} were adopted as the reference materials for LCF, and noticeably the existence of SeO_4^{2-} is driven by electrostatic adsorption in these materials

[27, 36]. In **Fig. 3.10d**, it can be clearly seen that both of them show much better fit to the data of S11, which definitely proves that most of SeO_4^{2-} in S11 exist depending on electrostatic interaction. In the case of SeO_3^{2-}, the better fitting result was also obtained using LDH as the reference material, and this can indicate that electrostatic interaction is the main occurrence mode for most of SeO_3^{2-} and SeO_4^{2-} in S9 and S11, respectively. In addition, the fitting curves were not perfectly in agreement with the observed curves using one kind of material as the reference (reflected by R-factor). When both LDH and cancrinite were adopted to fit the observed data of S11 (**Fig. 3.10d**), it showed much better fitting result (R-factor: 0.0016) than the single fitting (R-factor: 0.0093 and 0.0023), with the percentages of 61.30% and 38.70% for each fraction (LDH and cancrinite). This might imply that the SeO_4^{2-} in S11 can be divided into more than two fractions with different electrostatic interaction modes (coordination environment). This might be due to the disordered structure of geopolymer which could consist of various microstructures including rings, cages, etc., leading to different coordination environments [8]. This can be applied to the case of SeO_3^{2-} in S9 as well.

On the other hand, it has been noted that LDHs are formed in the NaOH-activated geopolymer and show suppressive effects on the Se leaching, even though the total dissolved amounts were relatively high (approximately 50%). In detail, The XRD patterns of S4 and S6 (**Fig. 3.3a**) have shown the presence of d_{003} peaks at the position of 11.64 and 11.54 degree/2θ with interlayer spacings of 7.60 and 7.66 Å which correspond to the carbonated-bearing hydrotalcite [39]. It seems that SeO_3^{2-} or SeO_4^{2-} is not immobilized in the interlayers of the formed LDHs in geopolymers. Then, the XRD patterns of S4 and S6 before and after water-leaching were compared in **Fig. 3.11**. It can be found that a small shift occurred to the 003 peaks for S4 and S6 after leaching.

This strongly suggests that the LDHs in geopolymers adsorb SeO_3^{2-} or SeO_4^{2-} during the leaching process. Therefore, the suppressive effect by LDHs is mainly due to its ion-exchange reaction during the leaching process, rather than direct immobilization of SeO_3^{2-} or SeO_4^{2-} in LDHs.

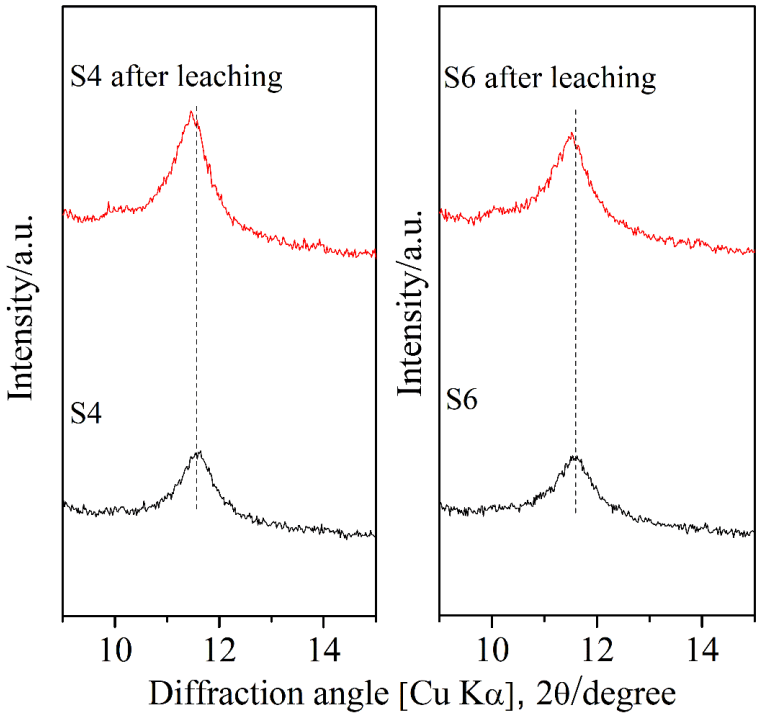

Fig. 3.11 XRD patterns of S4 and S6 before and after water-leaching.

Besides, as for the main associations of SeO_3^{2-} or SeO_4^{2-} in NaOH-activated geopolymers, there are also only several possible associations that are similar to the case for Na_2SiO_3-activated geopolymers. Apparently, the association mode that SeO_3^{2-} or SeO_4^{2-} is involved in aluminosilicate structure can be excluded. Then, TG results were compared to distinguish another two possible associations including sodium salts and electrostatic interaction. Specifically, the TG result of pure sodium selenite (**Fig. 3.12a**) clearly shows that the main weight loss occurs at approximately 700 and 800 ℃, which is inconsistent with that of S3. As for the SeO_4^{2-}, the indication from TG curve of S5 is also markedly different from the TG result for Na_2SeO_4 which has the main

weight loss closed to 800 ℃ (**Fig. 3.12b**). Therefore, for both SeO_3^{2-} and SeO_4^{2-}, their main associations should not be in the form of Na_2SeO_3 or Na_2SeO_4. Consequently, electrostatic interaction should be also the main immobilization mode of SeO_3^{2-} and SeO_4^{2-} in NaOH-activated geopolymers.

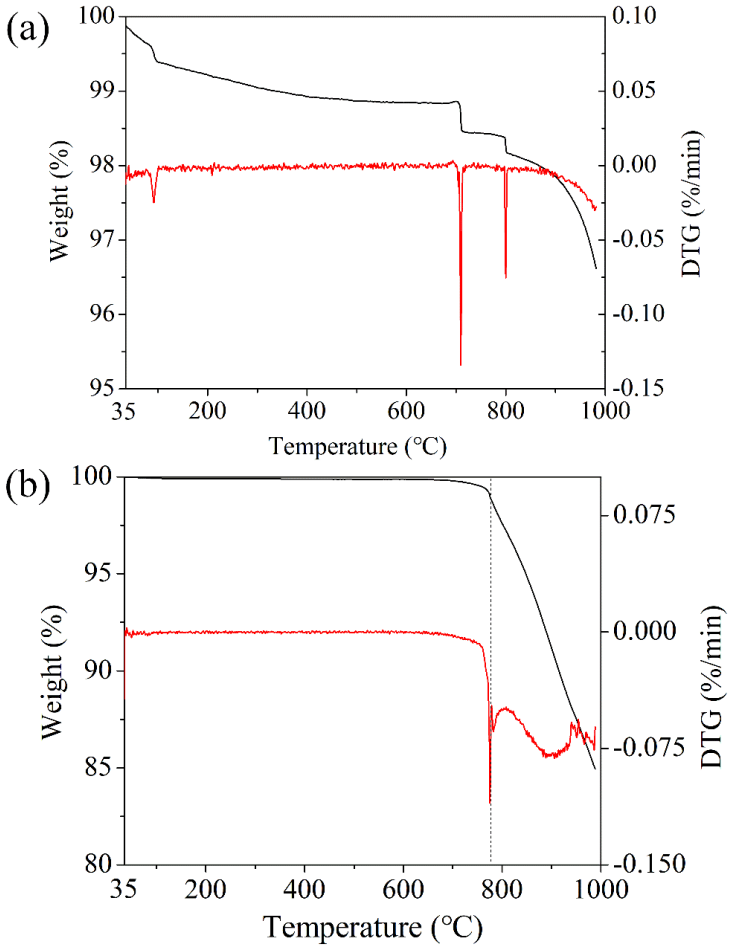

Fig. 3.12 TG results of pure (a) sodium selenite and (b) sodium selenate.

It has been known that electrostatic interaction is the main association mode for SeO_3^{2-} and SeO_4^{2-} in both NaOH- and Na_2SiO_3-activated geopolymers. However, large differences in the leaching results indicate the various properties of them. The leaching performance has a closed relationship with the specific surface area and pore structure of the sample. Hence, N_2 adsorption and desorption isotherms of geopolymer samples (**Fig. 3.13**) were collected with the control of particle size by 1 mm sieve. Obviously,

the pore volumes of Na_2SiO_3-activated geopolymers are much smaller than that of NaOH-activated geopolymers (**Table 3.3**), suggesting that the geopolymer activated by Na_2SiO_3 is more compact. Furthermore, the specific surface areas of S9 and S11 are 2.4 and 1.3 m^2/g, respectively, which are also much smaller than that of S3 and S5 (4.7 and 3.4 m^2/g) under the same granularity condition. This might account for the low Se leaching amount from Na_2SiO_3-activated geopolymers. In addition, all of geopolymers with CHT addition (S4, S6, S10, and S12) contained mesopores, suggested by the hysteresis loops between desorption and adsorption curves [40]. Moreover, for both NaOH- and Na_2SiO_3-activated geopolymers, the specific surface areas and pore volumes for the samples with CHT additive simultaneously increased compared to the samples without CHT addition (**Table 3.3**). This might be because the newly formed phases (LDH and possibly magnesium silicate hydrate) can destroy the continuous structure of geopolymer which is alternately connected by Si and Al tetrahedrons [41]. This can be also the most reasonable explanation for the increased Se leaching for S10 and S12. For NaOH-activated geopolymers, the formation of LDHs in S4 and S6 seems to overcome the disadvantage of the increased surface area and pore volume, leading to the decreased Se leaching amount. But for the geopolymers with CHT addition, the total leaching amounts of SeO_3^{2-} or SeO_4^{2-} from S4 and S6 were still larger than that from S10 and S12. This could be because Na_2SiO_3-activated geopolymers (S10 and S12) are still more compact than NaOH-activated geopolymers (S4 and S6), indicated by the total pore volumes. In addition, ^{27}Al and ^{29}Si NMR results have also shown that the Na_2SiO_3-activated geopolymers have higher geopolymeration degree than NaOH-activated geopolymers. Therefore, the compactness of geopolymer is critical for the immobilization of Se species.

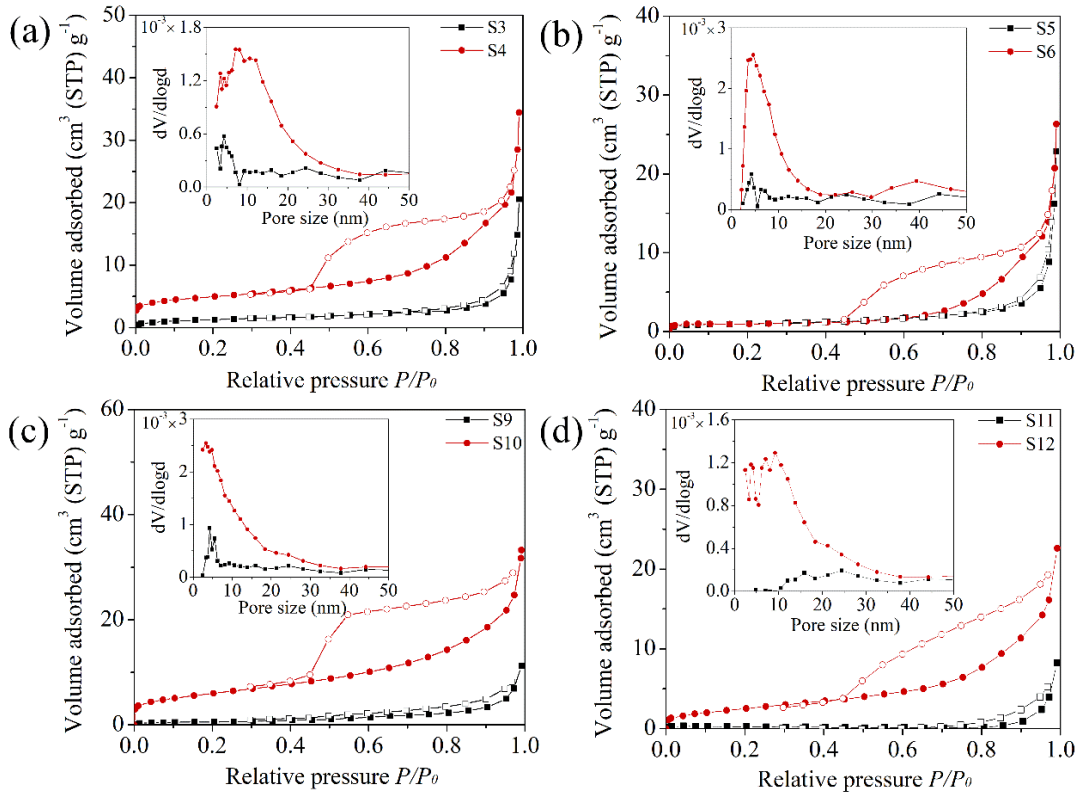

Fig. 3.13 Nitrogen adsorption–desorption isotherms of (a) S3 and S4, (b) S5 and S6, (c) S9 and S10, and (d) S11 and S12. Filled and empty symbols represent adsorption and desorption branches, respectively. The inset shows the corresponding pore size distribution curves determined by the BJH method using adsorption isotherm. Particle sizes of all samples are controlled by 1 mm sieve.

Table 3.3 Specific surface area and pore volume of geopolymer samples.

Sample	S_{BET}(m^2/g)	Pore volume (cm^3/g)
S3	4.7	0.0314
S4	11.9	0.0505
S5	3.4	0.0348
S6	4.1	0.0416
S9	2.4	0.0178
S10	20.9	0.0486
S11	1.3	0.0124
S12	9.1	0.0354

3.3.4 Compressive strength

Compressive strength is an important factor in the S/S of radioactive wastes, and **Fig. 3.14** shows the observed compressive strength of each geopolymer sample.

Na_2SiO_3-activated geopolymers have much higher compressive strengths (higher than 25 MPa) than that of NaOH-activated geopolymers (lower than 15 MPa). Previous reports have also shown that sodium silicate can significantly improve the mechanical strength of geopolymer paste [42, 43]. Theoretically, it can be explained well by the fact that higher amounts of Q^4(3Al) and Q^4(2Al) exist in Na_2SiO_3-activated geopolymers. In addition, there is relatively little effect on the compressive strengths of geopolymer samples with and without the addition of CHT for both NaOH- and Na_2SiO_3-activated geopolymers. As a whole, the compressive strength values of both NaOH- and Na_2SiO_3-activated geopolymers can meet the requirements of standard (GB14569.1-1993) [44]. Considering that the low Se leaching concentration is obtained from Na_2SiO_3-activated geopolymers, they might be able to be the promising materials for immobilization of Se oxyanions.

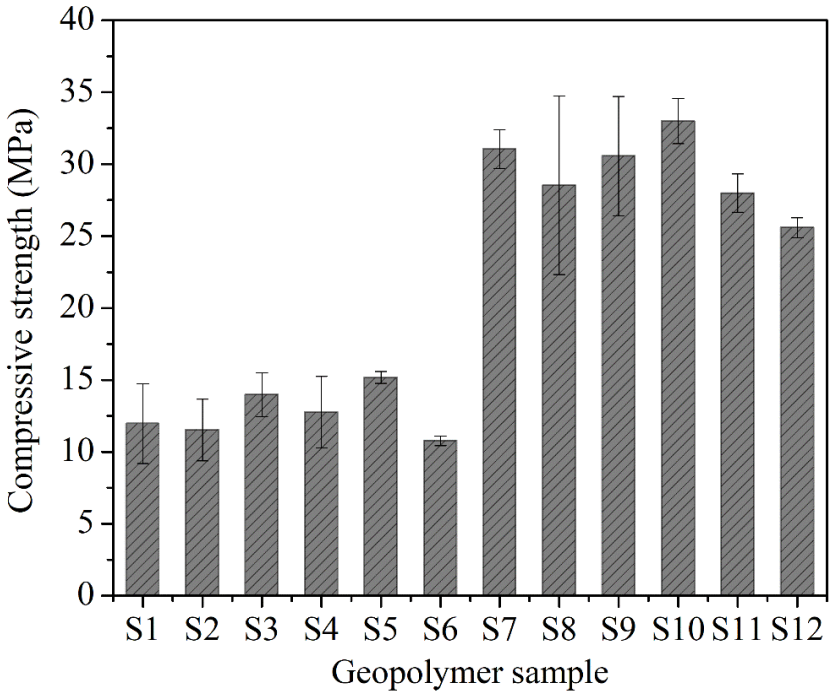

Fig. 3.14 Compressive strengths of geopolymer samples after 28 d curing.

3.4 Conclusions

The immobilization of SeO_3^{2-} and SeO_4^{2-} was explored using geopolymers activated by different alkaline solutions. The effect of calcined hydrotalcite on their leaching performances was also studied. It has been found that lower leaching percentages of SeO_3^{2-} and SeO_4^{2-} (approximately 10% and 18%) can be achieved in Na_2SiO_3-activated geopolymers (S9 and S11) with the comparison of NaOH-activated geopolymers (approximately 58% and 74% for S3 and S5, respectively). Based on the LCF and TG results, it has been proven that electrostatic interaction is the main association mode of SeO_3^{2-} and SeO_4^{2-} in both NaOH- and Na_2SiO_3-activated geopolymers. Therefore, the leaching behaviors of SeO_3^{2-} and SeO_4^{2-} should have a close relationship with the compactness of geopolymer. According to the BET results, the addition of CHT can increase the specific surface areas and pore sizes of both NaOH- and Na_2SiO_3-geopolymers. This can be the main reason why the Se leaching amount greatly increased from Na_2SiO_3-activated geopolymers (S10 and S12) where LDHs were not formed. While the leaching percentages of SeO_3^{2-} and SeO_4^{2-} decreased to approximately 50% and 60%, respectively, after the CHT was added into NaOH-activated geopolymers (S4 and S6), and this was mainly because of the formation of LDHs in these pastes. In addition, Na_2SiO_3-activated geopolymers showed much higher compressive strength (> 25 MPa) than NaOH-activated geopolymers (< 15 MPa). Therefore, Na_2SiO_3-activited geopolymer can be the promising material for the immobilization of Se oxyanions.

References

[1] Z. Li, S. Zhang, Y. Zuo, W. Chen, G. Ye, Chemical deformation of metakaolin based geopolymer, Cement and Concrete Research, 120 (2019) 108-118.

[2] T.A. Aiken, W. Sha, J. Kwasny, M.N. Soutsos, Resistance of geopolymer and Portland cement based systems to silage effluent attack, Cement and Concrete Research, 92 (2017) 56-65.

[3] A. Bakri, H. Kamarudin, M. Binhussain, I.K. Nizar, A. Rafiza, Y. Zarina, Comparison of geopolymer fly ash and ordinary portland cement to the strength of concrete, Advanced Science Letters, 19 (2013) 3592-3595.

[4] L. Zheng, W. Wang, W. Qiao, Y. Shi, X. Liu, Immobilization of Cu^{2+}, Zn^{2+}, Pb^{2+}, and Cd^{2+} during geopolymerization, Frontiers of Environmental Science & Engineering, 9 (2015) 642-648.

[5] H. Fansuri, I.I.M. Anisatun, A. Fatmawati, W.P. Utomo, W. Supriadi, R. Bayuaji, Cd^{2+} and Cr^{3+} Cation Immobilization by Using Geopolymer Based on PT. IPMOMI Fly Ash, Materials Science Forum, Trans Tech Publ, 2016, pp. 186-192.

[6] E. Joussein, M. Soubrand, G. Pascaud, A. Cogulet, S. Rossignol, Immobilization of Pb from mine sediments in metakaolin-based geomaterials, Environmental Science and Pollution Research, 26 (2019) 14473-14482.

[7] Q. Yu, S. Li, H. Li, X. Chai, X. Bi, J. Liu, T. Ohnuki, Synthesis and characterization of Mn-slag based geopolymer for immobilization of Co, Journal of Cleaner Production, 234 (2019): 97-104.

[8] Q. Tian, S. Nakama, K. Sasaki, Immobilization of cesium in fly ash-silica fume based geopolymers with different Si/Al molar ratios, Science of the Total Environment, 687 (2019) 1127-1137.

[9] C. Fernández-Pereira, Y. Luna-Galiano, M. Pérez-Clemente, C. Leiva, F. Arroyo, R. Villegas, L. Vilches, Immobilization of heavy metals (Cd, Ni or Pb) using aluminate geopolymers, Materials Letters, 227 (2018) 184-186.

[10] A. Al-Mashqbeh, S. Abuali, B. El-Eswed, F.I. Khalili, Immobilization of toxic inorganic anions ($Cr_2O_7^{2-}$, MnO_4^- and $Fe(CN)_6^{3-}$) in metakaolin based geopolymers: A preliminary study, Ceramics International, 44 (2018) 5613-5620.

[11] V. Nikolić, M. Komljenović, N. Džunuzović, T. Ivanović, Z. Miladinović, Immobilization of hexavalent chromium by fly ash-based geopolymers, Composites Part B: Engineering, 112 (2017) 213-223.

[12] W. Li, P. Ni, Y. Yi, Comparison of reactive magnesia, quick lime, and ordinary Portland cement for stabilization/solidification of heavy metal-contaminated soils, Science of the Total Environment, 671 (2019) 741-753.

[13] B. Guo, B. Liu, J. Yang, S. Zhang, The mechanisms of heavy metal immobilization by cementitious material treatments and thermal treatments: A review, Journal of Environmental Management, 193 (2017) 410-422.

[14] M. Zhang, Incorporation of Oxyanionic B, Cr, Mo, and Se into Hydrocalumite and Ettringite: Application to Cementitious Systems, The University of Waterloo 2000.

[15] Q. Tian, B. Guo, S. Nakama, L. Zhang, Z. Hu, K. Sasaki, Reduction of undesirable element leaching from fly ash by adding hydroxylated calcined dolomite, Waste Management, 86 (2019) 23-35.

[16] B. Guo, S. Nakama, Q. Tian, N.D. Pahlevi, Z. Hu, K. Sasaki, Suppression processes of anionic pollutants released from fly ash by various Ca additives, Journal of Hazardous Materials, 371 (2019) 474-483.

[17] B. Guo, K. Sasaki, T. Hirajima, Characterization of the intermediate in formation of selenate-substituted ettringite, Cement and Concrete Research, 99 (2017) 30-37.

[18] B. Guo, Y. Xiong, W. Chen, S.A. Saslow, N. Kozai, T. Ohnuki, I. Dabo, K. Sasaki, Spectroscopic and First-Principles Investigations of Iodine Species Incorporation into Ettringite: Implications for Iodine Migration in Cement Waste Forms, Journal of Hazardous Materials, (2019) 121880.

[19] K.-H. Goh, T.-T. Lim, Z. Dong, Application of layered double hydroxides for removal of oxyanions: a review, Water Research, 42 (2008) 1343-1368.

[20] H. Ji, W. Wu, F. Li, X. Yu, J. Fu, L. Jia, Enhanced adsorption of bromate from aqueous solutions on ordered mesoporous Mg-Al layered double hydroxides (LDHs), Journal of Hazardous Materials, 334 (2017) 212-222.

[21] L.V. Constantino, J.N. Quirino, A.M. Monteiro, T. Abrão, P.S. Parreira, A. Urbano, M.J. Santos, Sorption-desorption of selenite and selenate on Mg-Al

layered double hydroxide in competition with nitrate, sulfate and phosphate, Chemosphere, 181 (2017) 627-634.

[22] G. Mishra, B. Dash, S. Pandey, Layered double hydroxides: A brief review from fundamentals to application as evolving biomaterials, Applied Clay Science, 153 (2018) 172-186.

[23] U. EPA, Method 1311. Toxicity characteristic leaching procedure, US Environmental Protection Agency Washington, DC, USA, 1992.

[24] A. Ankudinov, B. Ravel, J. Rehr, S. Conradson, Real-space multiple-scattering calculation and interpretation of x-ray-absorption near-edge structure, Physical Review B, 58 (1998) 7565–7576.

[25] M. Newville, IFEFFIT: interactive XAFS analysis and FEFF fitting, Journal of synchrotron radiation, 8 (2001) 322-324.

[26] B. Ravel, M. Newville, ATHENA and ARTEMIS: interactive graphical data analysis using IFEFFIT, Physica Scripta, 2005 (2005) 1007.

[27] Q. Tian, K. Sasaki, A novel composite of layered double hydroxide/geopolymer for co-immobilization of Cs^+ and SeO_4^{2-} from aqueous solution, Science of the Total Environment, 695 (2019) 133799.

[28] C.A. Rees, J.L. Provis, G.C. Lukey, J.S. Van Deventer, In situ ATR-FTIR study of the early stages of fly ash geopolymer gel formation, Langmuir, 23 (2007) 9076-9082.

[29] S. Joshi, S. Kalyanasundaram, V. Balasubramanian, Quantitative analysis of sodium carbonate and sodium bicarbonate in solid mixtures using Fourier transform infrared spectroscopy (FT-IR), Applied Spectroscopy, 67 (2013) 841-845.

[30] R.-C. Zeng, Z.-G. Liu, F. Zhang, S.-Q. Li, H.-Z. Cui, E.-H. Han, Corrosion of molybdate intercalated hydrotalcite coating on AZ31 Mg alloy, Journal of Materials Chemistry A, 2 (2014) 13049-13057.

[31] M. Ebert, D. Havlíček, Magnesium selenites, Chem. zvestí, 34 (1980) 441-451.

[32] M. González, I. Pavlovic, R. Rojas-Delgado, C. Barriga, Removal of Cu^{2+}, Pb^{2+} and Cd^{2+} by layered double hydroxide–humate hybrid. Sorbate and sorbent comparative studies, Chemical Engineering Journal, 254 (2014) 605-611.

[33] M. Haouas, F. Taulelle, C. Martineau, Recent advances in application of ^{27}Al NMR spectroscopy to materials science, Progress in Nuclear Magnetic Resonance Spectroscopy, 94-95 (2016) 11-36.

[34] G. Engelhardt, D. Michel, High-resolution solid-state NMR of silicates and zeolites, 1987.

[35] C. Dupuy, A. Gharzouni, I. Sobrados, N. Texier-Mandoki, X. Bourbon, S. Rossignol, ^{29}Si, ^{27}Al, ^{31}P and ^{11}B magic angle spinning nuclear magnetic resonance study of the structural evolutions induced by the use of phosphor- and boron–based additives in geopolymer mixtures, Journal of Non-Crystalline Solids, 521 (2019) 119541.

[36] N.D. Pahlevi, B. Guo, K. Sasaki, Immobilization of selenate in cancrinite using a hydrothermal method, Ceramics International, 44 (2018) 8635-8642.

[37] S.R. Bare, XANES measurements and interpretation, EXAFS Data Collection and Analysis Course, Advanced Photon Source, July, 26 (2005) 29.

[38] A. Owens, XANES fingerprinting: a technique for investigating CCD surface structures and measuring dead layer thicknesses, Nuclear Instruments and Methods in Physics Research Section A: Accelerators, Spectrometers, Detectors and Associated Equipment, 526 (2004) 391-398.

[39] J.T. Kloprogge, D. Wharton, L. Hickey, R.L. Frost, Infrared and Raman study of interlayer anions CO_3^{2-}, NO_3^-, SO_4^{2-} and ClO_4^- in Mg/Al-hydrotalcite, American Mineralogist, 87 (2002) 623-629.

[40] W. Luo, J. Ouyang, P. Antwi, M. Wu, Z. Huang, W. Qin, Microwave/ultrasound-assisted modification of montmorillonite by conventional and gemini alkyl quaternary ammonium salts for adsorption of chromate and phenol: Structure-function relationship, Science of the Total Environment, 655 (2019) 1104-1112.

[41] M. Xia, J. Sanjayan, Method of formulating geopolymer for 3D printing for construction applications, Materials & Design, 110 (2016) 382-390.

[42] E. Mohseni, Assessment of Na_2SiO_3 to NaOH ratio impact on the performance of polypropylene fiber-reinforced geopolymer composites, Construction and Building Materials, 186 (2018) 904-911.

[43] M. Morsy, S. Alsayed, Y. Al-Salloum, T. Almusallam, Effect of sodium silicate to sodium hydroxide ratios on strength and microstructure of fly ash geopolymer binder, Arabian journal for science and engineering, 39 (2014) 4333-4339.

[44] J.F. Li, J.L. Wang, Solidification of 30% TBP-OK waste by calcium sulfoaluminate cement, Advanced Materials Research, Trans Tech Publ, 2013, pp. 2782-2785.

Chapter 4

Influence of silicate on the structural memory effect of layered double hydroxides for the immobilization of selenium

4.1 Introduction

Layered double hydroxides (LDHs) have been viewed as good adsorbents/stabilizers for adsorption/stabilization of Se oxyanions due to its high sorption capacity, low economic cost, and long-term stability [1-4]. Normally, the structure of LDHs can be expressed as $[M(II)_{1-x}M(III)_x(OH)_2]^{x+}\ (A^{n-})_{x/n} \cdot mH_2O$, where *M(II)* and *M(III)* are the divalent and trivalent metallic cations, and A^{n-} is the interlayer anion [5, 6]. There is a special property of LDHs called "memory effect" which means that the metal oxides collected by calcining LDHs (CLDHs) at the temperature above 400 ℃ can be regenerated into LDH structure again when exposed to the solution containing anionic species [7]. The removals of anionic species including F^-, AsO_4^{3-}, SeO_3^{2-}, SeO_4^{2-}, etc. by calcined products of LDHs have been widely studied and conducted, due to their good properties such as tunable composition, high stability and easy regeneration [8-10]. Furthermore, the effects of organic matters such as humic acids and inorganic ions including Cl^-, SO_4^{2-}, etc. on the regeneration of LDHs from CLDHs have been comprehensively explored [11-14]. In the previous study [3], we proposed that the incorporation of the LDH phase in the geopolymer paste might overcome this drawback. Thus, calcined hydrotalcite was incorporated into the geopolymer paste, and it was found that soluble silicate had an adverse effect on the regeneration of LDH [15]. However, the exact reaction mechanism is still unknown. In addition, silicate is the most abundant substance in natural environments, being the main constituent of minerals such as zeolite, kaolinite, quartz [16, 17]. Under geological conditions (e.g. alkali condition), silicate could be slowly dissolved from these minerals. Thus, silicate might also affect the metal uptake and phase transformation of CLDHs when they are applied in the practical conditions. Therefore,

it is imperative and meaningful to understand the effect of silicate ion on the phase transformation and sorption ability of CLDHs. Therefore, in the present study, five kinds of CLDHs were obtained from the calcinations of Mg_2Al-LDH, $Mg_2Al_{0.75}Fe_{0.25}$-LDH, $Mg_2Al_{0.5}Fe_{0.5}$-LDH, $Mg_2Al_{0.25}Fe_{0.75}$-LDH, and Mg_2Fe-LDH, respectively. Solid residues collected after reaction were characterized by XRD, SEM, FTIR, NMR, XPS, and N_2 adsorption-desorption isotherm, to make clear the specific reaction mechanism.

4.2 Experimental

4.2.1 Materials

Carbonate forms of LDHs were synthesized using a co-precipitation method as reported previously [18]. In detail, the Mg^{2+}, Al^{3+}, and Fe^{3+} solutions were prepared by dissolving $Mg(NO_3)_2{\cdot}6H_2O$ (98%, Wako), $Al(NO_3)_3{\cdot}9H_2O$ (97%, Wako) and $Fe(NO_3)_3{\cdot}9H_2O$ (99%, Wako), respectively. The molar ratio of divalent ion (Mg^{2+})/trivalent ion(s) (Al^{3+} + Fe^{3+}) was controlled to 2, and the molar ratios of Al^{3+}/Fe^{3+} were adjusted to 3:1, 1:1 and 1:3 for the synthesis of different ternary compounds in addition to the binary compounds (Mg_2Al-LDH and Mg_2Fe-LDH). Then, the prepared divalent and trivalent ion solutions were simultaneously added in drops to the solution containing 0.5 M Na_2CO_3 with a pH of 10.5 controlled by adding 10 M NaOH. After stirring for 30 min, the obtained slurries were moved to 100 mL autoclaves, aged at 100 ℃ for 20 h. The solid residues were obtained after centrifuging, washing and freeze-drying, and named as LDH-1 (Mg_2Al-LDH), LDH-2 ($Mg_2Al_{0.75}Fe_{0.25}$-LDH), LDH-3 ($Mg_2Al_{0.5}Fe_{0.5}$-LDH), LDH-4 ($Mg_2Al_{0.25}Fe_{0.75}$-LDH) and LDH-5 (Mg_2Fe-LDH), respectively. Accordingly, the calcination products were

acquired by calcining them at 500 ℃ for 3 h, named as CLDH-1, CLDH-2, CLDH-3, CLDH-4, and CLDH-5, respectively.

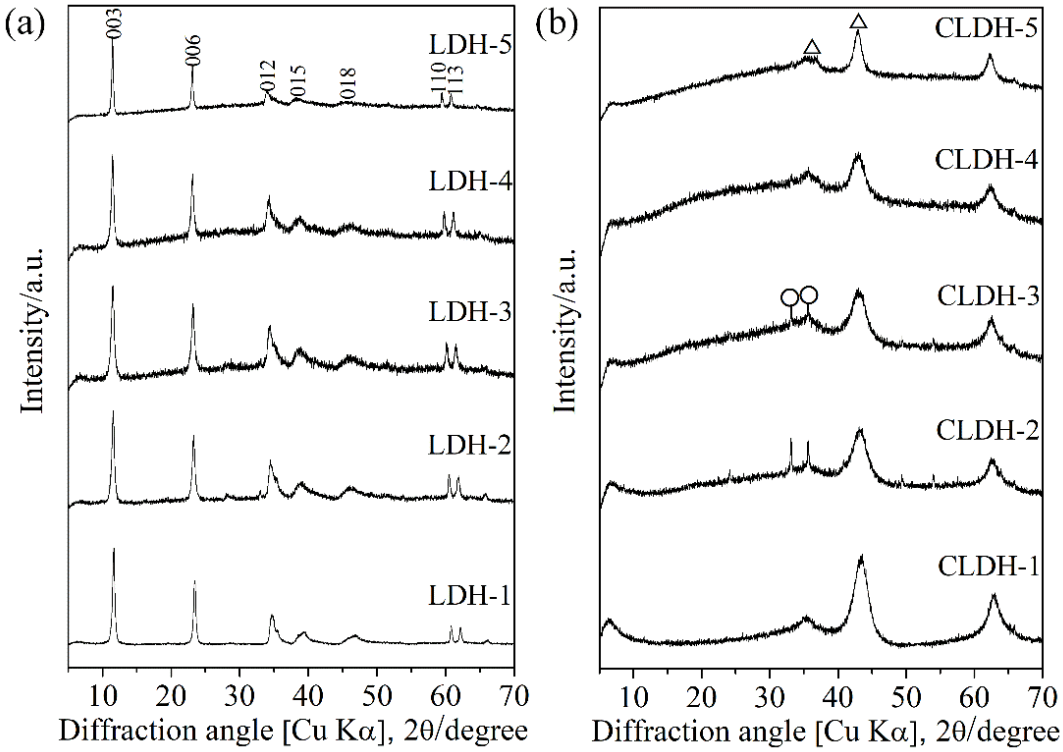

Fig. 4.1 XRD patterns of (a) LDHs and (b) CLDHs. Symbol: △, $MgAl_3O_4$; ○, Fe_2O_3.

The XRD patterns of synthesized LDHs and the calcined products (CLDHs) are shown in **Fig. 4.1**. All of the pure LDHs present the characteristic peaks of LDHs as previously reported [3, 5, 19]. After calcination, the main peaks of the products (approximately 35°, 43°, and 62°/2θ) can be attributed to the formation of metal oxides, and two sharp peaks assigned to Fe_2O_3 appeared in the patterns of CLDH-2 and CLDH-3. This is also consistent with the previous studies [20, 21]. The elemental compositions of CLDHs were determined by ICP-OES after dissolving in nitric acid solution, and the results were given in **Table 4.1**. The elemental analysis indicated that the Mg/(Al+Fe) and Al/Fe molar ratios of each CLDH were extremely closed to the theoretical values.

Besides, the selenite and selenate solutions were prepared from dissolutions of Na_2SeO_3 (97%, Wako) and Na_2SeO_4 (97%, Wako), respectively. Sodium metasilicate nonahydrate (98%, Sigma) was used as the silicate source. Moreover, the deionized water used in this study was decarbonated through boiling and N_2 bubbling simultaneously.

Table 4.1 Elemental compositions of calcined layered double hydroxides (determined by ICP-OES).

Sample	Elemental concentration (mmol/g)			Elemental molar ratio	
	Mg	Al	Fe	Mg/(Al+Fe)	Al/Fe
CLDH-1	9.17	4.89	-	1.87	-
CLDH-2	8.59	3.33	0.88	2.04	3.78
CLDH-3	8.42	2.08	1.98	2.08	1.05
CLDH-4	8.15	0.99	3.14	1.97	0.32
CLDH-5	8.33	-	4.24	1.96	-

3.2.2 Sorption experiments

Five kinds of CLDHs were used as adsorbents/stabilizers for the immobilization of Se oxyanions from solutions. In order to make clear comparisons between these CLDHs, the experimental conditions were fixed. Thus, adsorption thermodynamics and dynamics analysis were not included in the present study, as other reports did [3, 22, 23]. Specifically, a certain amount of each CLDH was added into the solutions containing 1.267 mM Se (SeO_3^{2-} or SeO_4^{2-}) separately with and without the addition of 3.560 mM silicate ions. The initial solution pH for batch tests was adjusted to 10 and 13, respectively by adding 10 M NaOH or HNO_3. Then, these mixtures were stirred at 400 rpm for 24 h to reach the equilibrium under ambient condition and then separated by membrane filtration. The obtained solid residues were collected and dried in a vacuum dryer, and the solutions were stored for further analysis of elemental concentration. Noticeably, the ratio of solid/liquid was kept at 1 g/L in all of the cases.

4.2.3 Characterizations

An ICP-OES (Optima 8300, US) was adopted to determine the concentrations of Se and Si in the supernatant. XRD patterns (scanning range: 5–70 2θ/degree) of solid residues were collected on a Rigaku Ultima IV XRD (Akishima, Japan) using Cu Kα (40 kV, 40 mA) at a scanning speed of 2° min^{-1} and scanning step of 0.02°. Microscopic observation was achieved on a VE-9800 (Osaka, Japan) with the acceleration voltages of 20 kV. In addition, the FTIR spectra (400–4000 cm^{-1}) of the samples diluted by KBr were collected on a JASCO 670 Plus (Japan) spectrometer at a resolution of 4 cm^{-1}. The N_2 adsorption-desorption curves of calcined products were recorded on a high-precision surface area and pore size distribution analyzer (BEL-Max, BEL, Japan) at –196 ℃, with the pretreatment under vacuum at 150 ℃ for 6 h. XPS spectra including wide scans and narrow scans for Si were acquired on an ESCA 5800 (Kanagawa, Japan) with the utilization of a mono-chromated Al Kα X-ray source, and the binding energy of C1s (284.6 eV) for adventitious carbon was used for the energy calibration. Furthermore, ^{29}Si NMR spectra were collected on an ECA 400 (Akishima, Japan), with the field strength and resonance frequency of 9.39 T and 79.4 MHz, respectively. In addition, the relaxation delay of 10 s and a π/2-pulse length of 3.375 μs were used for the measurement.

4.3 Results and discussion

4.3.1 Sorption results

The sorption amounts of SeO_3^{2-} and SeO_4^{2-} by CLDHs are shown in **Fig. 4.2a** and **4.2b**, respectively. Under the initial pH of 10 without silicate, the sorption capacity of SeO_3^{2-} by CLDH-1 reached up to approximately 1 mmol/g. However, the sorption

amount slowly decreased with the increase of Fe content in CLDHs (-2, -3 and -4). Extremely low sorption capacity of SeO_3^{2-} (approximately 0.15 mmol/g) was obtained by CLDH-5, and a similar trend can also be found in the case of SeO_4^{2-} (**Fig. 4.2b**). Both pH and silicate have significant effects on the sorption of SeO_3^{2-} and SeO_4^{2-} by CLDHs. The sorption amount of them decreased to lower than 0.3 mmol/g at pH 13 without silicate ion. When the silicate ions exist, the sorption amounts of them dramatically decreased whether the pH is 10 or 13. However, compared to the binary metal oxides (CLDH-1, -5), the ternary metal oxides (CLDH-2, -3, -4) have more resistance to the effects of high pH and silicate for the sorption of Se oxyanions, especially in the case of SeO_4^{2-}. In addition, the sorption amounts of silicate were also determined and shown in **Fig. 4.2c** and **Fig. 4.2d**. Similarly, higher sorption amounts of silicate were achieved by the ternary metal oxides (CLDH-2, -3, -4). Noticeably, the sorption capacities of silicate ions were higher at pH 10 than that at pH 13 for CLDH-2, -3, -4 and -5. CLDH-5 can only sorb extremely less amount of silicate at pH 13. However, the opposite trend was found only in the case of CLDH-1. This should be because of their various properties. Furthermore, it can be found that the reaction pH was not changeable as for the initial pH of 13. For the initial pH of 10, the pH after reaction became higher (from 10.5 to 11.5 approximately), mainly due to the hydroxylation of metal oxides.

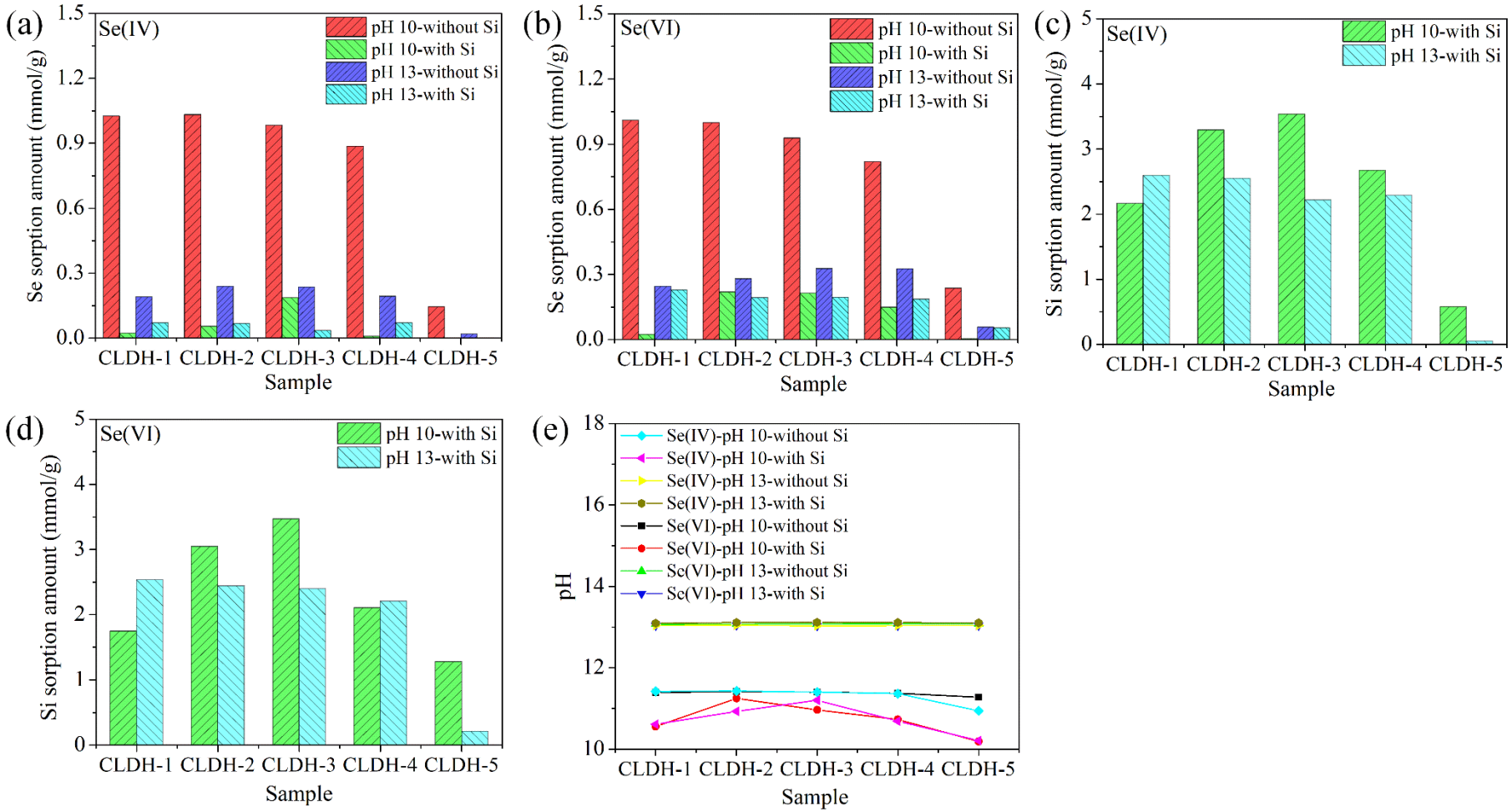

Fig. 4.2 Sorption results and solution pH after reactions of CLDHs: (a) Se(IV) sorption results, (b) Se(VI) sorption results, (c) Si sorption amounts in the presence of Se(IV), (d) Si sorption amounts in the presence of Se(VI), (e) solution pH after reaction. The error is within 5%.

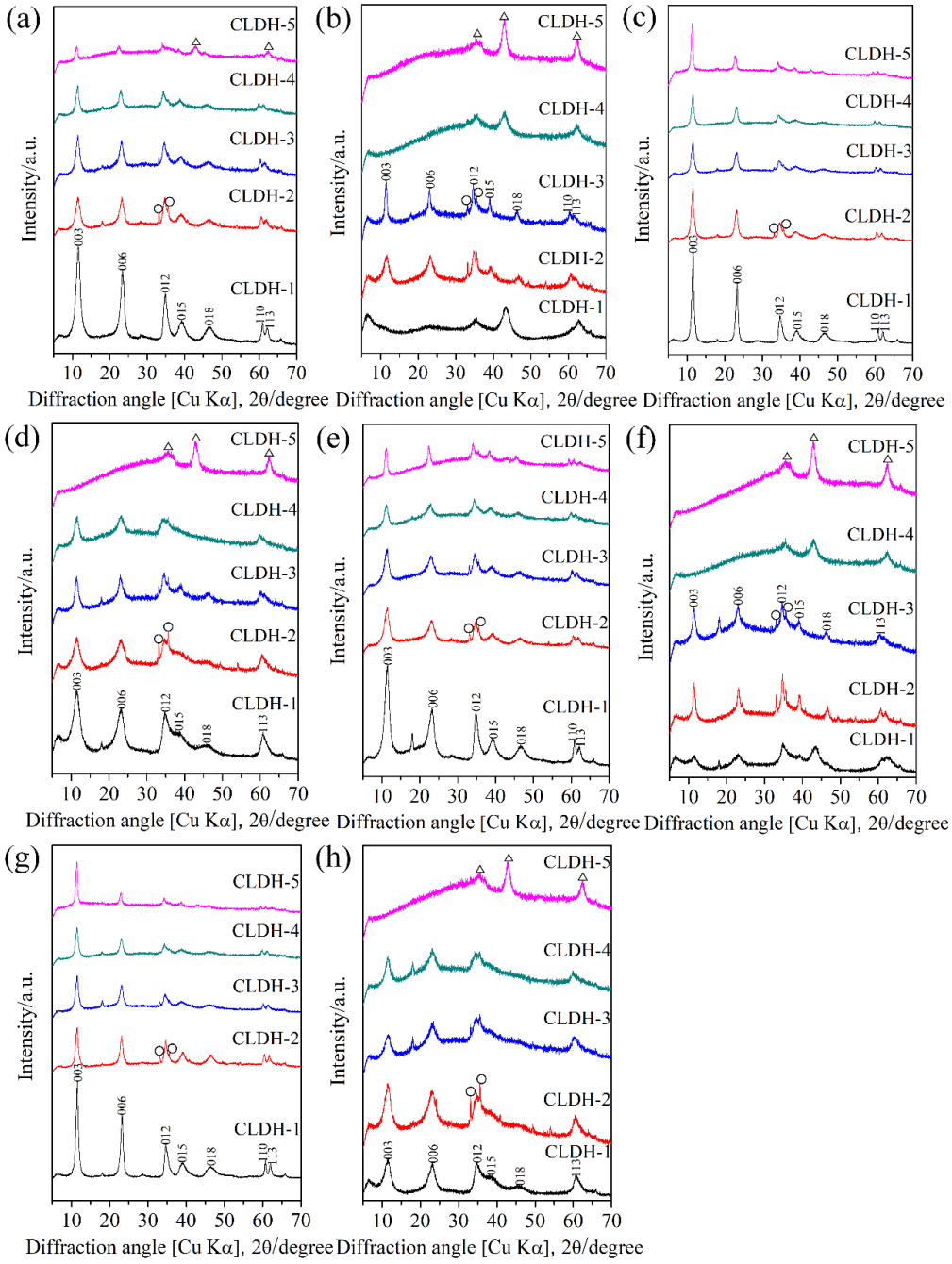

Fig. 4.3 XRD patterns of solid residues after reactions: (a) Se(IV) sorption without Si at pH 10, (b) Se(IV) sorption with Si at pH 10, (c) Se(IV) sorption without Si at pH 13, (d) Se(IV) sorption with Si at pH 13, (e) Se(VI) sorption without Si at pH 10, (f) Se(VI) sorption with Si at pH 10, (g) Se(VI) sorption without Si at pH 13, (h) Se(VI) sorption with Si at pH 13. Symbol: △, $MgAl_3O_4$; ○, Fe_2O_3.

4.3.2 Solid characterizations

The XRD patterns of solid residues were collected to understand the memory effect of LDHs as given in **Fig. 4.3**. At the initial pH of 10, the LDHs were regenerated

for corresponding CLDHs in the absence of silicate (**Fig. 4.3a** and **Fig. 4.3e**). Obviously, there is still a part of unreacted CLDH-5 that existed in the solid residue, and this should be due to the lower dissolution rate of MgFe oxide than MgAl oxide. However, the crystallinities of the formed LDHs at pH 13, especially LDH -5 (**Fig. 4.3c** and **Fig. 4.3g**), seems to be much higher than the products obtained at pH 10. This is mainly because the higher supersaturation of Mg^{2+} is easily achieved at higher pH, which is favorable to the nucleation [24, 25]. It can be noticed that LDH-2 and -3 appeared after reaction with silicate at pH 10, but there was no LDH formed for CLDH-1, -4, and -5 under the same condition (**Fig. 4.3b** and **4.3f**). This suggests that silicate has less effect on the hydroxylation processes of ternary oxides. Interestingly, the regenerations of LDH-1 and LDH-4 occurred at pH 13 in the presence of silicate, and the CLDH-5 still remained as the metal oxides after the reaction (**Fig. 4.3d** and **4.3h**). It seems that pH and silicate ion have synergistic influences on the generation of LDHs as to binary and ternary metal oxides. Besides, the interlayer spacings (d_{003} values) of raw LDHs and the regenerated LDHs were calculated as presented in **Table 4.2**. The d_{003} values of raw LDHs are varied from 7.58 to 7.70 Å which exactly corresponds to the carbonate-type LDHs [26, 27]. Typically, the d_{003} value increases with the increase of Fe content in these LDHs (from LDH-1 to LDH-5), mainly due to the different lattice parameters of MgAl-LDH and MgFe-LDH [26, 27]. As for the regenerated LDHs from CLDHs, the interlayer spacings just increase slightly and the corresponding 2θ values are approximately 11.50°, indicating the occupation of CO_3^{2-} in the interlayer of LDHs. This should be caused by the residual carbonate in the CLDHs after calcination and the atmospheric CO_2 which was not completely removed from deionized water [13]. In addition, the slight increase of the interlayer spacings of

regenerated LDHs implies that the adsorbed SeO_3^{2-} and SeO_4^{2-} have been incorporated into their interlayers because both of them possess spatial configurations, and CO_3^{2-} has a planar structure, even though the radii of them are smaller than that of CO_3^{2-} [28].

Table 4.2 The interlayer spaces (Å) of the formed LDHs under different conditions.

Experimental condition	CLDH-1	CLDH-2	CLDH-3	CLDH-4	CLDH-5
Raw LDH	7.5833	7.6362	7.6758	7.7019	7.7020
Se(IV)-pH 10-without Si	7.6356	7.6620	7.7147	7.7422	7.8811
Se(IV)-pH 10-with Si	-	7.5579	7.7018	-	-
Se(IV)-pH 13-without Si	7.6354	7.6881	7.6489	7.7014	7.7965
Se(IV)-pH 13-with Si	7.6886	7.7425	7.7027	7.5959	-
Se(VI)-pH 10-without Si	7.6880	7.6881	7.5552	7.8655	7.9357
Se(VI)-pH 10-with Si	7.8234	7.7013	7.6758	-	-
Se(VI)-pH 13-without Si	7.6487	7.6752	7.7284	7.7151	7.7556
Se(VI)-pH 13-with Si	7.5440	7.5322	7.5712	7.7676	-

Fig. 4.4 presents XPS wide-scan results of samples after sorption with SeO_3^{2-} in the presence of silicate. Obviously, the elemental components of CLDHs (e.g. Mg, Al, Fe) can be detected in the corresponding samples. Furthermore, the Si 2p peak can be found at E_B=102 eV in each sample, which suggests the interactions between silicate and CLDHs (e.g. Mg, or Al). The SEM images of CLDHs after reaction under different conditions are presented in **Fig. 4.5.** All of the regenerated LDHs were broken and irregular. A sheet structure can be observed for CLDH-1 after reaction (**Fig. 4.5a** and **4.5b**). With the increase of Fe content in CLDHs, the morphologies of them, especially CLDH-5, became trashier and more irregular. This indicated the decrease of their crystallinities, which was consistent with the XRD results (**Fig. 4.3**). In the presence of silicate (**Fig. 4.5c** and **4.5d**), the SEM images of solid residues did not show significant differences from the samples reacted without silicate, even though the LDHs were not formed after the reaction of CLDH-5. The FTIR spectra of raw LDHs and the hydrated products of CLDHs were collected to know the chemical bonds in

the products, presented in **Fig. 4.6**. According to the previous studies [15, 19, 29], the peaks at approximately 3480 and 1660 cm^{-1} can be assigned to the stretching and bending vibrations of OH groups, respectively. The vibration mode of CO_3^{2-} can be found at approximately 1380 cm^{-1}. The absorbance in the regions of 700-800 and 900 cm^{-1} are attributed to the vibrations of Se-O bond in selenite and selenate, respectively. Due to the different sorption densities of CLDHs under various conditions, the vibrations of them can only be obviously seen in the spectra of CLDHs with high sorption amount of selenium at pH 10 (**Fig. 4.6b** and **Fig. 4.6f**). In addition, the vibration of Si-O can be observed at approximately 1020 cm^{-1}, which suggests that the silicate has been immobilized in the CLDHs after the reaction.

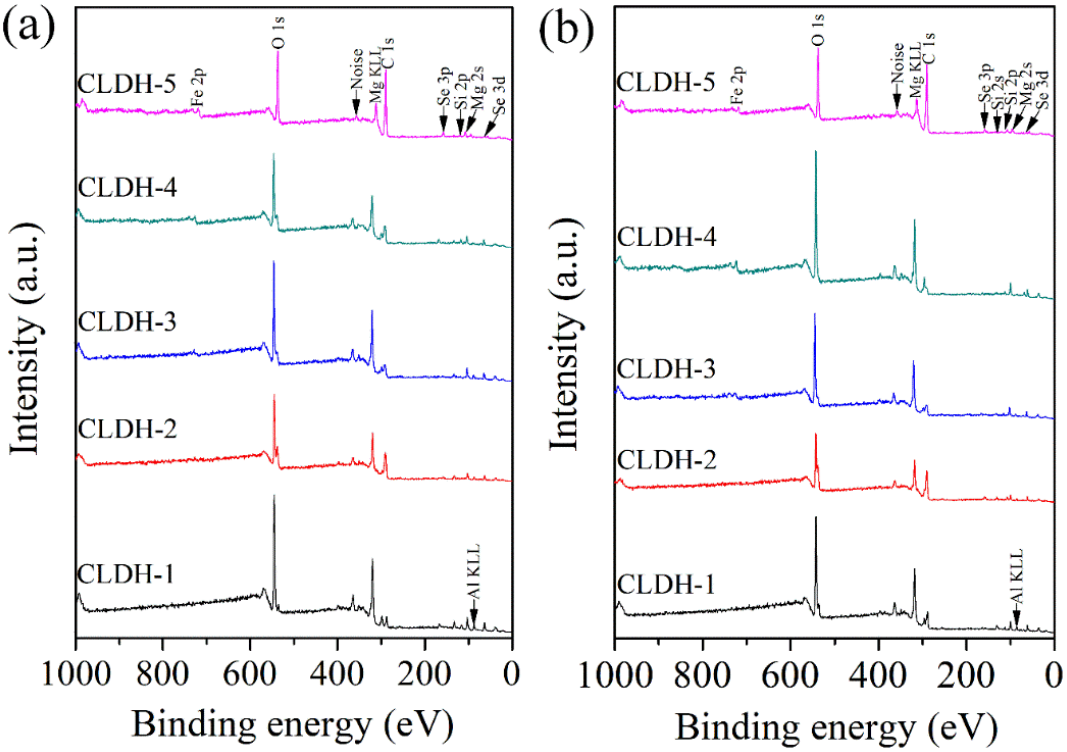

Fig. 4.4 XPS wide-scans of CLDHs after reaction: (a) Se(IV) sorption with Si at pH 10, (b) Se(IV) sorption with Si at pH 13.

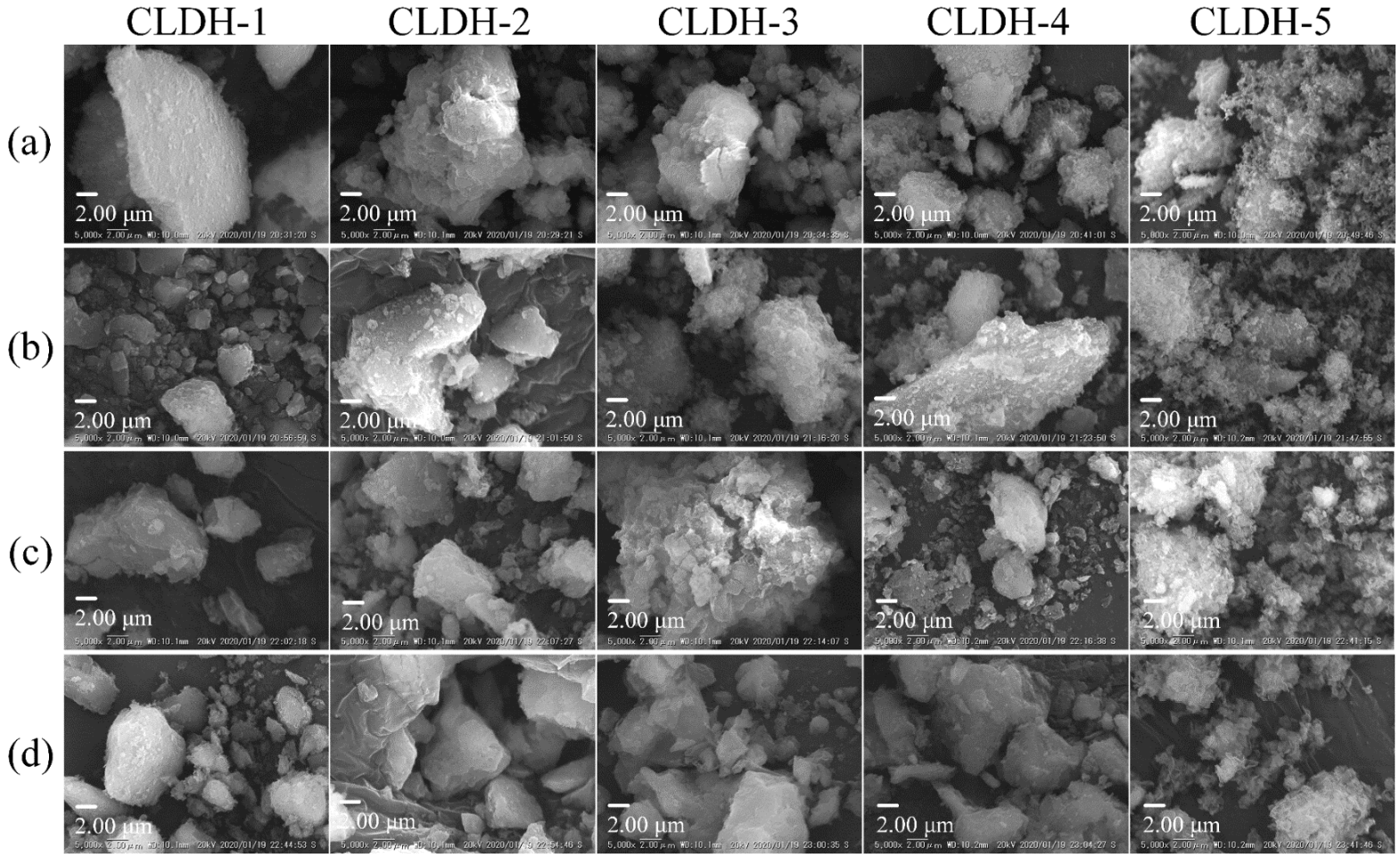

Fig. 4.5 SEM images of CLDHs after reaction in the presence of Se(IV): (a) without Si at pH 10, (b) without Si at pH 13, (c) with Si at pH 10, (d) with Si at pH 13.

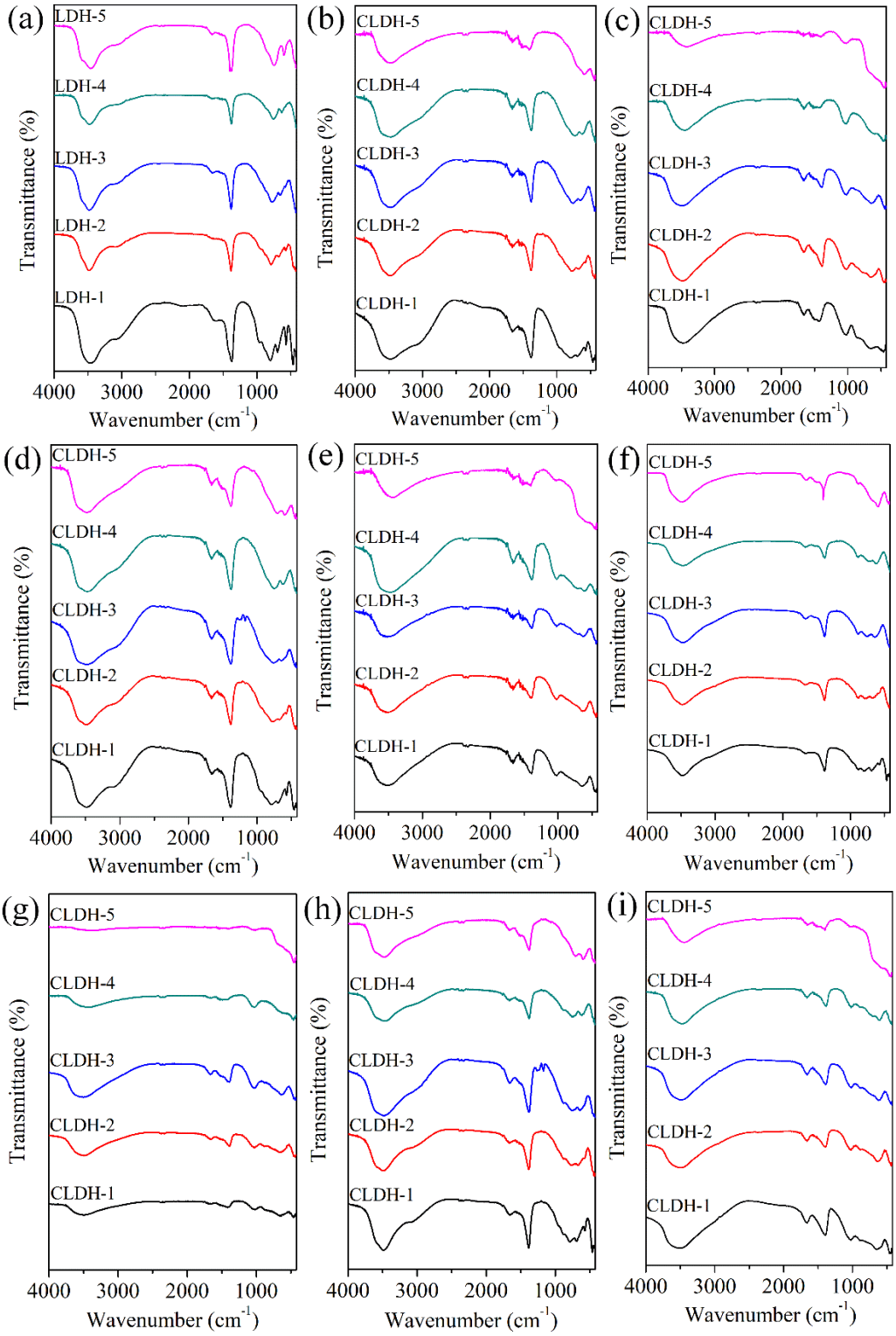

Fig. 4.6. FTIR spectra of solid residues after reactions: (a) raw LDH (b) Se(IV) sorption without Si at pH 10, (c) Se(IV) sorption with Si at pH 10, (d) Se(IV) sorption without Si at pH 13, (e) Se(IV) sorption with Si at pH 13, (f) Se(VI) sorption without Si at pH 10, (g) Se(VI) sorption with Si at pH 10, (h) Se(VI) sorption without Si at pH 13, (i) Se(VI) sorption with Si at pH 13.

4.3.3 Reaction mechanisms

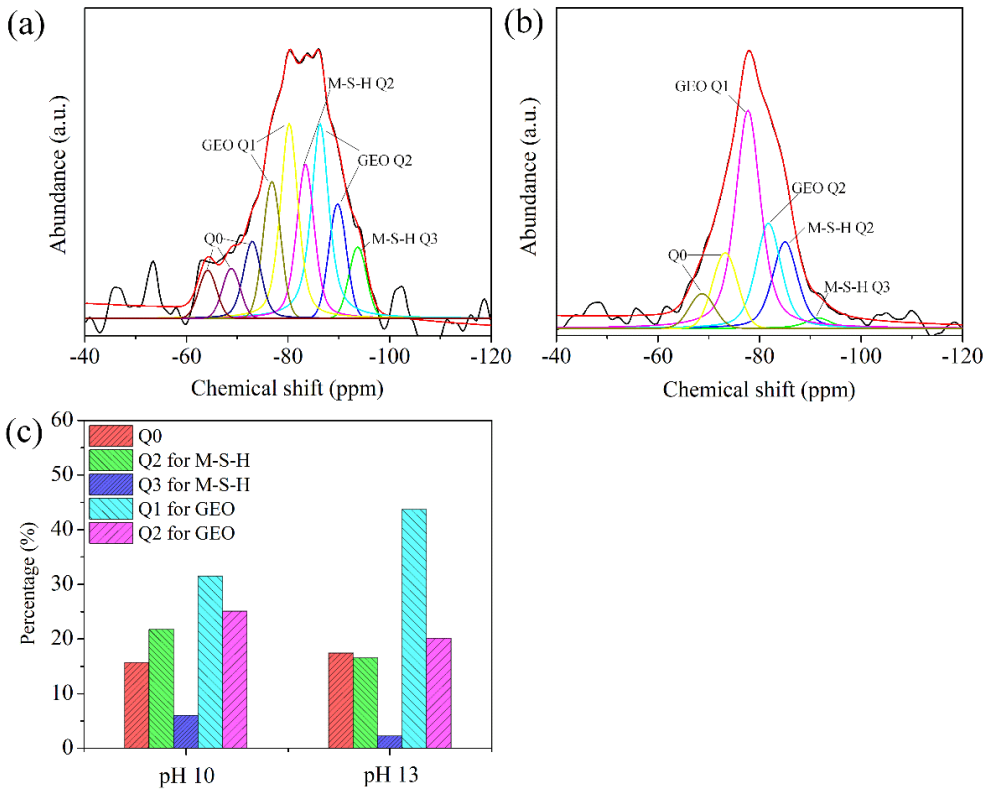

Fig. 4.7 ^{29}Si MAS NMR spectra for: (a) solid residue of CLDH-1 after sorption of Se(IV) at pH 10, (b) solid residue of CLDH-1 after sorption of Se(IV) at pH 13, (c) normalized summary of Si coordination environments in samples accordingly identified in the deconvoluted ^{29}Si NMR spectra.

According to the above analysis, both pH and silicate ion have significant effects on the regeneration of LDHs from CLDHs and the immobilization of Se oxyanions. As for higher pH, the surface charge of LDH would decrease because of more OH^- existed in the solution, and there is also an increased competition between Se oxyanions and OH^- into LDH interlayer, leading to less sorption amounts of Se by LDHs which were accordingly regenerated from CLDHs [30, 31]. However, the effect of silicate on the regeneration of LDHs and Se immobilization is still unclear. As we all know, Mg-based LDHs can be viewed as the structure of $Mg(OH)_2$ sheet where Al^{3+} or Fe^{3+} partially substituted for Mg^{2+}, and the regeneration of LDH structure should be mainly controlled by the hydroxylation of MgO in the synthesized binary or

ternary metal oxides [32, 33]. In the presence of silicate, the hydroxylation of MgO might be influenced, and some other phases should be possibly generated [34]. In order to confirm the hypothesis, the coordinations of Si in the solid residues are needed for a better understanding of the reactions.

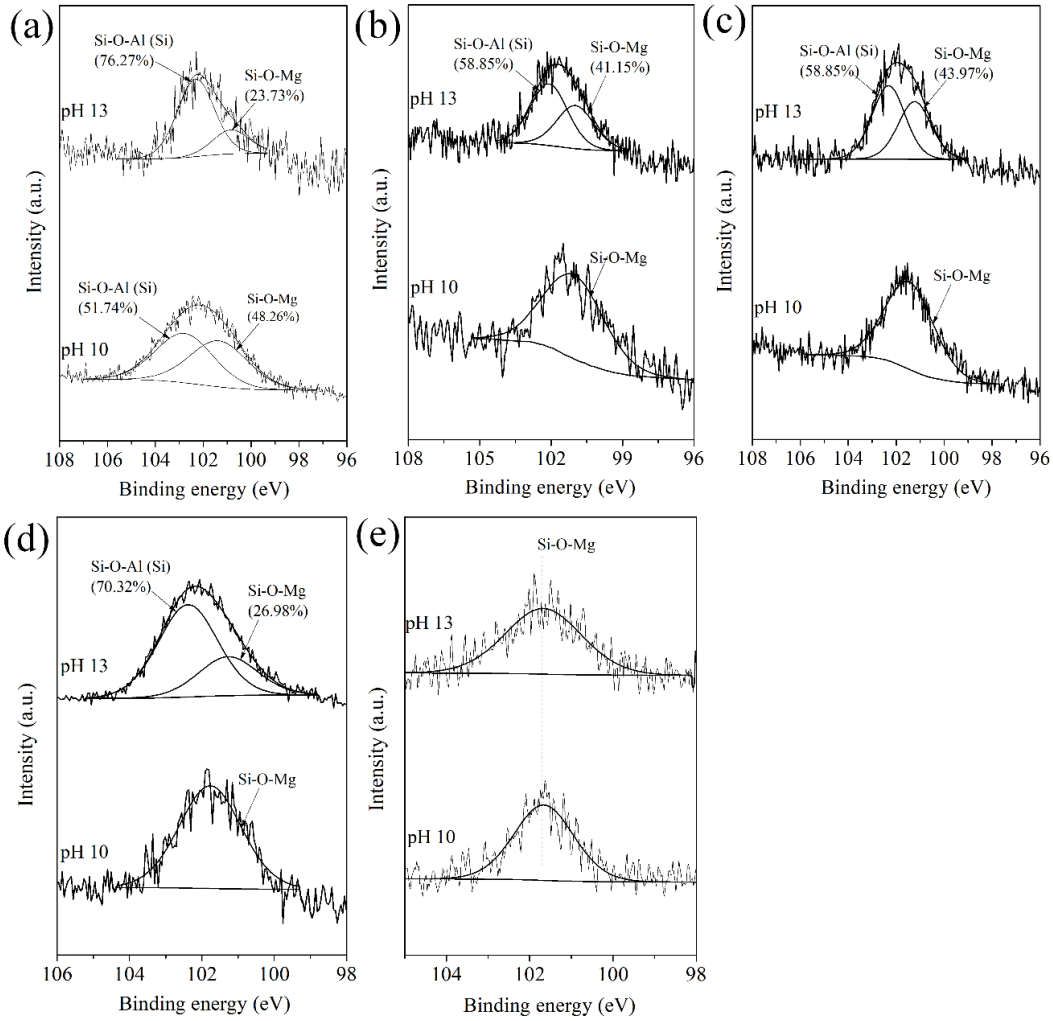

Fig. 4.8 XPS Si 2p spectra of (a) CLDH-1, (b) CLDH-2, (c) CLDH-3, (d) CLDH-4 and (e) CLDH-5 after sorption of Se(IV) at pH 10 and 13, respectively.

^{29}Si NMR spectroscopy is an extremely useful technique to get a better understanding of the Si coordination in the solid residues. However, the high content of Fe in the sample would influence the NMR measurement. Therefore, the ^{29}Si MAS NMR spectra of CLDH-1 after sorption of SeO_3^{2-} at pH 10 and 13 in the presence of

silicate were collected. The spectra and their corresponding deconvolutions are presented in **Fig. 4.7**. Based on the elemental composition of CLDHs (**Table 4.1**), the soluble silicate ions can react with MgO to generate magnesium silicate hydrate (M-S-H) and be polymerized with themselves or aluminate ions (geopolymer-like structure, GEO). According to the previous studies [35-38], the chemical shifts centered at approximately – 85~88 and – 92~96 ppm can be assigned to Q^2 and Q^3 for M-S-H, respectively. As for the reaction products of CLDH-1 at pH 10 with silicate ions (**Fig. 4.7a**), it can be clearly seen that there are two bands at – 86.3 and – 93.7 ppm which can be assigned to Q^n (n = 2 and 3) for M-S-H as stated above. While, the chemical shifts centered at – 64.2, – 68.8, and – 73.0 ppm ascribing to Q^0 have also been separated from the spectra, and this also suggests the existence of different coordination environments of Si tetrahedrons [39]. The chemical shifts at – 76.8 and – 80.2 ppm can be caused by the presence of Q^1 for geopolymer-like substance, and Q^2 (or Q^4(4Al) and Q^4(3Al)) can be given to the chemical shifts at – 83.4 and – 89.8 ppm [39]. The existence of different positions of Q^1 and Q^2 confirms that the geopolymer-like substance was not homogeneously formed during the reaction. Furthermore, it can be obviously found that there is a chemical shift at – 77.7 ppm assigned to Q^1 in the spectra of CLDH-1 after reaction at pH 13 (**Fig. 4.7b**). This is mainly caused by the polymerization of silicate ions, rather than the formation of M-S-H because the peak intensity of Q^1 for M-S-H is generally very low compared to Q^2 and Q^3 [40]. Thus, the chemical shifts at – 81.8 ppm could be attributed to the substitution of aluminum in the silicate connection (Q^2(1Al)) [15]. In addition, the Q^2 and Q^3 for M-S-H are presented at – 85.0 and – 91.6 ppm, respectively. It can be clearly seen that there was a larger amount of Q^1 (GEO) existed in the solid residue after

reaction at pH 13, while the percentages of Q^2 (M-S-H) and Q^3 (M-S-H) greatly decreased (**Fig. 4.7c**). This indicated that higher pH enhanced the formation of geopolymer-like substance and suppressed the reaction between silicate ion and MgO. This phenomenon can also be supported by surface analysis. **Fig. 4.8** presents XPS narrow scans of Si 2p for solid residues after sorption of Se(IV) on CLDHs at pH 10 and 13, respectively. Obviously, the bonds assigned to Si-O-Mg and Si-O-Al (Si) can be observed for the CLDH-1 after reaction at pH 10 (**Fig. 4.8a**) [41-43]. The percentage of Si-O-Al (Si) increased from 51.74 to 76.27% for CLDH-1 after reaction at pH 13, while the amount of Si-O-Mg decreased from 48.26 to 23.73%. Therefore, the pH-depending mechanisms should be the main reasons for the diverse phase transformations of CLDH-1 reacted at pH 10 and 13 in the presence of silicate (**Fig. 4.9**). At pH 10, the newly formed M-S-H and geopolymer-like substance would cover on the surface of particles, and blocked the hydroxylation of MgAl-oxide, resulting in the disappearance of LDH after CLDH-1 reacted at pH 10 in the presence of silicate. The proposed mechanism can also be applied for the CLDH-4 and CLDH-5 because the M-S-H was found on the surfaces of them, indicated by the XPS results (**Fig. 4.8d** and **Fig. 4.8e**). When pH increased to 13, the interaction between MgO and silicate was suppressed. Thus, less silicate ions would not cover on the surface of MgO at pH 13. On the other hand, higher pH promoted the dissolution of Al from CLDHs to enhance the formation of geopolymer-like substance, and consequently the more fresh surface of MgO can be produced. Therefore, hydroxylation of MgO was then much highly enhanced, resulting in the formation of LDHs for CLDH-1 and CLDH-4 reacted at pH 13 in the presence of silicate ions. However, as for CLDH-5, the LDH was still not regenerated at pH 13 in the presence of silicate ion. This should be mainly because

Fe-oxide in CLDH-5 does not have a good solubility as Al-oxide, and it cannot react with silicate ion. Moreover, although higher pH suppressed the sorption of silicate ions onto the surface of MgO, the existence of Si-O-Mg can still be detected in the XPS spectrum, which indicated that the surface of CLDH-5 was still covered by M-S-H (**Fig. 4.9**). Thus, the Al-oxide in CLDH plays a critical role in the regeneration of LDHs from CLDHs at higher pH with silicate.

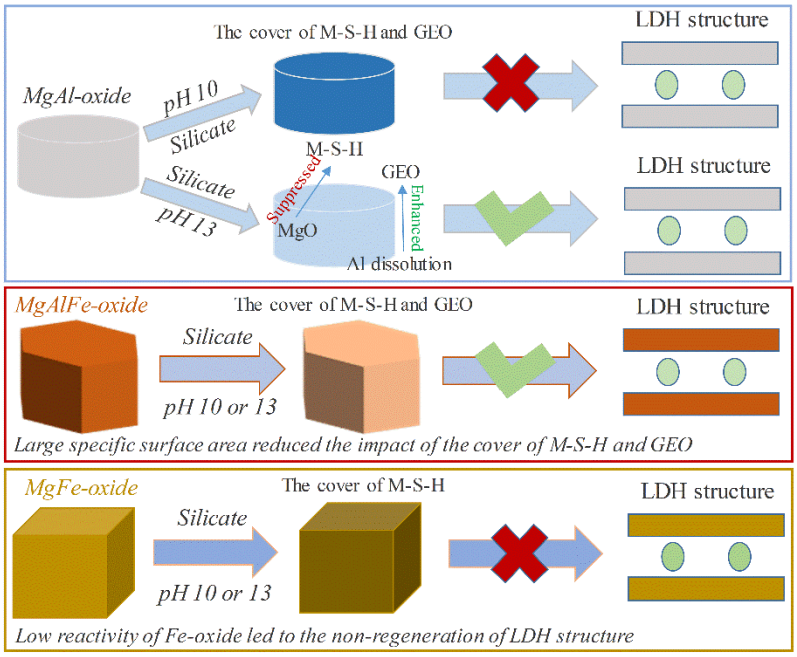

Fig. 4.9 Schematic illustration for the reaction processes of binary and ternary oxides.

On the other hand, it has been observed that pH did not have any effect on the regeneration of LDHs from CLDH-2 and CLDH-3 even though silicate ions existed. LDHs were generated from CLDH-2 and CLDH-3 after reaction at pH 10 in the presence of silicate ions, which was totally different from CLDH-1, -4, and -5. These CLDHs have similar elemental compositions, but with different contents as refer to Al and Fe. Furthermore, the reactions between silicate ion and the compositions of CLDHs have been clear as stated above. The existence of the Si-O-Mg structure can be suggested in the Si 2p spectra of all CLDHs (**Fig. 4.8**). Thus, the distinct

phenomenon that occurred to CLDH-2 and CLDH-3 might be caused by the physical properties, rather than the chemical properties of CLDHs. Among them, the specific surface area is an important property of CLDHs which can have significant effects on the reaction rate, or even reaction direction [50, 51]. Therefore, the N_2 adsorption-desorption curves of CLDHs were collected and shown in **Fig. 4.10**. All of the curves belong to type III according to the International Union of Pure and Applied Chemistry. The biggest difference between CLDH-2, -3, and other samples is that the main pore size of CLDH-2 and CLDH-3 is much smaller than that of other CLDHs, indicated by BJH pore size distribution. Accordingly, the calculated specific surface areas of CLDH-2 and CLDH-3 are 127.7 and 158.2 m^2/g, respectively, which is much higher than that of CLDH-1, -4, and -5 (**Fig. 4.11**). This suggests that larger surface areas of CLDH-2 and CLDH-3 can benefit for the reaction. Since the concentration of silicate ion was fixed to 3.56 mM/L (100 mg/L Si), the average concentration of silicate ion around the surfaces of CLDH-2 and CLDH-3 would be lower than that of other CLDHs. Thus, there are high possibilities for CLDH-2 and CLDH-3 to proceed the hydroxylation of metal oxides. In order to further confirm it, the higher concentration of silicate was used for the reaction with CLDH-2 and CLDH-3, respectively. The XRD patterns (**Fig. 4.12**) indicated that the LDHs were not regenerated as well as the cases for CLDH-1, -4, and -5. Similarly, the surfaces of CLDH-2 and CLDH-3 particles should be also covered by the formed phases (M-S-H) when the silicate concentration becomes higher. Thus, it can be concluded that specific surface areas of CLDHs play a critical role in the phase transformation. On the other hand, for CLDH-2 and CLDH-3, the final solution pHs after reaction at the initial pH of 10 increased up to approximately 11 which was higher than the pHs for other CLDHs (**Fig. 4.2e**),

and the phenomenon might also benefit from the larger surface areas of CLDH-2 and CLDH-3. Meanwhile, it is definitely in favor of the LDH regeneration from CLDHs, as indicated earlier.

4.4 Conclusions

The effect of silicate on the phase transformations of calcined layered double hydroxides for the immobilization of SeO_3^{2-} and SeO_4^{2-} was explored at pH 10 and 13, respectively. It has been found that both pH and silicate have significant effects on the immobilization of SeO_3^{2-} and SeO_4^{2-} using CLDHs. The sorption amounts of them dramatically decreased when pH became higher. This is mainly because there is a larger amount of OH^- in the solution with a higher pH, thereby leading to the less positive surface charge of regenerated LDHs and increased competition between Se oxyanions and OH^- into LDH interlayers. On the other hand, silicate ion could react with the MgO and Al_2O_3 in CLDHs to accordingly generate magnesium silicate hydrate and geopolymer-like substance, certified by NMR and XPS results. These substances covered on the surface of CLDHs and blocked the hydroxylation of metal oxides, resulting in the non-regeneration of LDHs particularly for CLDH-1 and CLDH-4 after reaction at pH 10 in the presence of silicate. However, higher pH can suppress the interaction between MgO and silicate and enhance the formation of geopolymer-like substance, which relatively promotes the regeneration of LDHs. Al in CLDHs plays a critical role in the regeneration of LDHs. Overall, the ternary oxides (CLDH-2 and CLDH-3) have more resistance to the effect of silicate, mainly because they possess much larger specific surface areas (127.7 and 158.2 m^2/g) than binary oxides.

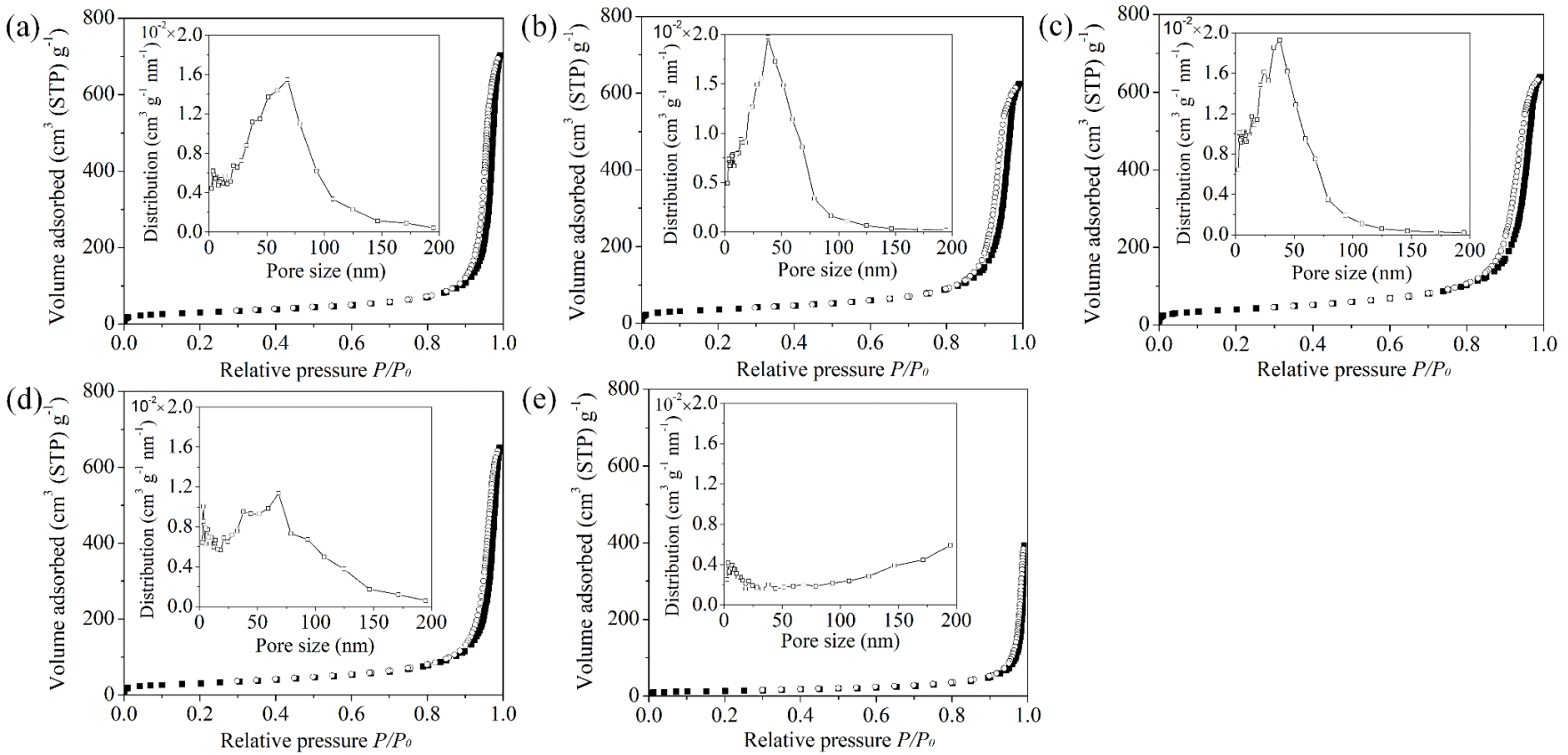

Fig. 4.10 Nitrogen adsorption–desorption isotherms of (a) CLDH-1, (b) CLDH-2, (c) CLDH-3, (d) CLDH-4, and (e) CLDH-5. Filled and empty symbols represent adsorption and desorption branches, respectively. The inset shows the corresponding pore size distribution curves determined by the BJH method using adsorption isotherm.

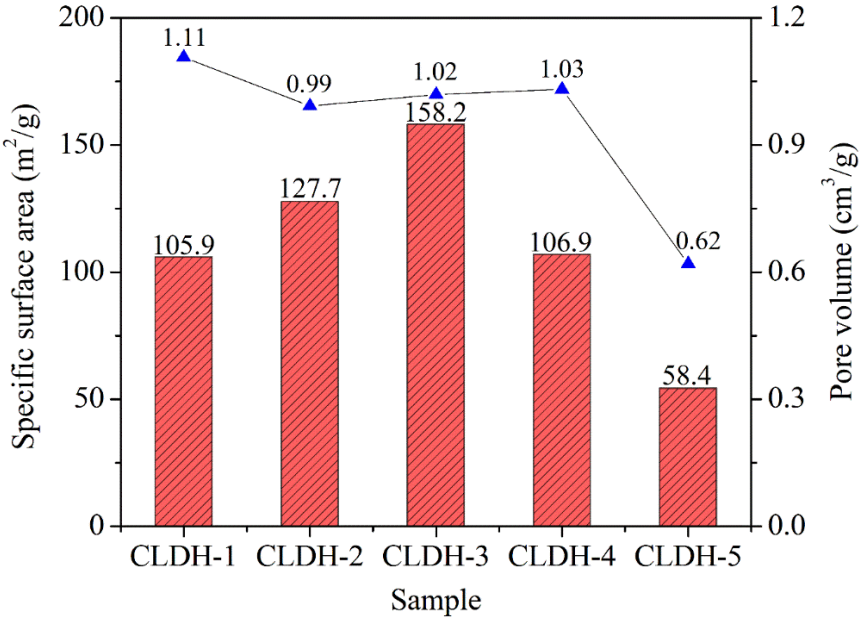

Fig. 4.11 Specific surface areas and pore volumes of calcined layered double hydroxides.

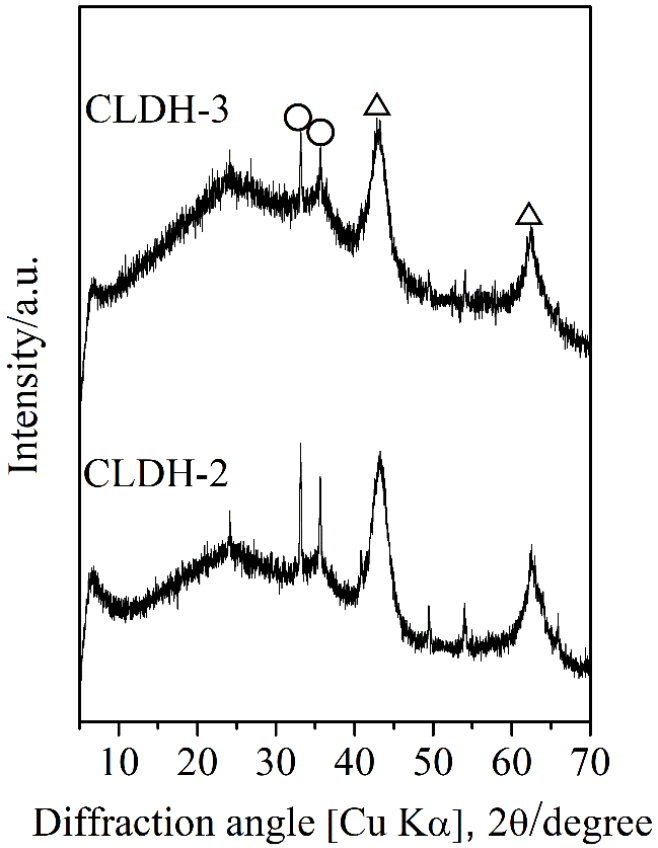

Fig. 4.12 XRD patterns of CLDH-2 and CLDH-3 after reaction. Experimental condition: 1.267 mM SeO_3^{2-}, 17.80 mM silicate ions, initial pH: 10.

References

[1] H. Asiabi, Y. Yamini, M. Shamsayei, Highly selective and efficient removal of arsenic (V), chromium (VI) and selenium (VI) oxyanions by layered double hydroxide intercalated with zwitterionic glycine, Journal of Hazardous Materials, 339 (2017) 239-247.

[2] K.-H. Goh, T.-T. Lim, Z. Dong, Application of layered double hydroxides for removal of oxyanions: a review, Water Research, 42 (2008) 1343-1368.

[3] Q. Tian, K. Sasaki, A novel composite of layered double hydroxide/geopolymer for co-immobilization of Cs^{+} and SeO_4^{2-} from aqueous solution, Science of the Total Environment, 695 (2019) 133799.

[4] P. Koilraj, Y. Kamura, K. Sasaki, Synergetic co-immobilization of SeO_4^{2-} and Sr^{2+} from aqueous solution onto multifunctional graphene oxide and carbon-dot based layered double hydroxide nanocomposites and their mechanistic investigation, Journal of Materials Chemistry A, 6 (2018) 10008-10018.

[5] P. Zhong, Q. Yu, J. Zhao, S. Xu, X. Qiu, J. Chen, Degradation of bisphenol A by Fe-Al layered double hydroxides: A new synergy of homo- and heterogeneous Fenton systems, Journal of Colloid and Interface Science, 552 (2019) 122-133.

[6] P. Koilraj, Y. Kamura, K. Sasaki, Cosorption characteristics of SeO_4^{2-} and Sr^{2+} radioactive surrogates using 2D/2D graphene oxide-layered double hydroxide nanocomposites, ACS Sustainable Chemistry & Engineering, 6 (2018) 13854-13866.

[7] S.H.J. Eiby, D.J. Tobler, S. Nedel, A. Bischoff, B.C. Christiansen, A.S. Hansen, H.G. Kjaergaard, S.L.S. Stipp, Competition between chloride and sulphate during the reformation of calcined hydrotalcite, Applied Clay Science, 132 (2016) 650-659.

[8] P. Wu, L. Xia, Y. Liu, J. Wu, Q. Chen, S. Song, Simultaneous sorption of arsenate and fluoride on calcined Mg–Fe–La hydrotalcite-like compound from water, ACS Sustainable Chemistry & Engineering, 6 (2018) 16287-16297.

[9] L.V. Constantino, J.N. Quirino, A.M. Monteiro, T. Abrão, P.S. Parreira, A. Urbano, M.J. Santos, Sorption-desorption of selenite and selenate on Mg-Al layered double hydroxide in competition with nitrate, sulfate and phosphate, Chemosphere, 181 (2017) 627-634.

[10] M. Wu, J. Zhang, Y. Peng, J. Zhou, X. Ruan, J. Liu, Q. Liu, Y. Xi, R. Frost, G. Qian, An investigation into mechanism of cation adsorption by reconstruction of calcined layered double hydroxide, Microporous and Mesoporous Materials, 242 (2017) 182-189.

[11] L. Zhang, X. Qiu, J. Chen, Influence of humic acid on the structure memory effect of hydrocalumite and its performance in the adsorption cycles of bisphenol A, Journal of Water Process Engineering, 32 (2019) 100987.

[12] L. Fang, W. Li, H. Chen, F. Xiao, L. Huang, P.E. Holm, H.C.B. Hansen, D. Wang, Synergistic effect of humic and fulvic acids on Ni removal by the calcined Mg/Al layered double hydroxide, RSC Advances, 5 (2015) 18866-18874.

[13] L. Fang, J. Hou, C. Xu, Y. Wang, J. Li, F. Xiao, D. Wang, Enhanced removal of natural organic matters by calcined Mg/Al layered double hydroxide nanocrystalline particles: Adsorption, reusability and mechanism studies, Applied Surface Science, 442 (2018) 45-53.

[14] L.V. Constantino, J.N. Quirino, T. Abrão, P.S. Parreira, A. Urbano, M.J. Santos, Sorption–desorption of antimony species onto calcined hydrotalcite: Surface structure and control of competitive anions, Journal of Hazardous Materials, 344 (2018) 649-656.

[15] Q. Tian, B. Guo, K. Sasaki, Immobilization mechanism of Se oxyanions in geopolymer: Effects of alkaline activators and calcined hydrotalcite additive, Journal of Hazardous Materials, 387 (2020) 121994.

[16] J. Li, C. Shi, H. Zhang, X. Zhang, Y. Wei, K. Jiang, B. Zhang, Silicalite-1 zeolite membrane: Synthesis by seed method and application in organics removal, Chemosphere, 218 (2019) 984-991.

[17] J.T. Kloprogge, S. Komarneni, J.E. Amonette, Synthesis of smectite clay minerals: a critical review, Clays and Clay Minerals, 47 (1999) 529-554.

[18] X. Qiu, K. Sasaki, S. Xu, J. Zhao, Double-Edged Effect of humic acid on multiple sorption modes of calcined layered double hydroxides: Inhibition and promotion, Langmuir, 35 (2019) 6267-6278.

[19] S. Xu, J. Zhao, Q. Yu, X. Qiu, K. Sasaki, Understanding how specific functional groups in humic acid affect the sorption mechanisms of different calcinated layered double hydroxides, Chemical Engineering Journal, (2019) 123633.

[20] A.C. Heredia, M.I. Oliva, U. Agú, C.I. Zandalazini, S.G. Marchetti, E.R. Herrero, M.E. Crivello, Synthesis, characterization and magnetic behavior of Mg–Fe–Al mixed oxides based on layered double hydroxide, Journal of Magnetism and Magnetic Materials, 342 (2013) 38-46.

[21] A.C. Heredia, M.I. Oliva, C.I. Zandalazini, U.A. Agú, G.A. Eimer, S.G. Casuscelli, E.R. Herrero, C.F. Pérez, M.E. Crivello, Synthesis, Characterization, and catalytic behavior of Mg–Al–Zn–Fe mixed oxides from precursors layered double hydroxide, Industrial & Engineering Chemistry Research, 50 (2011) 6695-6703.

[22] M. Li, B. Zhang, S. Zou, Q. Liu, M. Yang, Highly selective adsorption of vanadium (V) by nano-hydrous zirconium oxide-modified anion exchange resin, Journal of Hazardous Materials, 384 (2020) 121386.

[23] W. Luo, Q. Huang, P. Antwi, B. Guo, K. Sasaki, Synergistic effect of ClO_4^- and Sr^{2+} adsorption on alginate-encapsulated organo-montmorillonite beads: Implication for radionuclide immobilization, Journal of Colloid and Interface Science, 560 (2020) 338-348.

[24] M. Laska, J. Valtýni, P. Fellner, Influence of pH on the crystal size distribution of $Mg(OH)_2$ prepared by the hydration of MgO, Crystal Research and Technology, 28 (1993) 931-936.

[25] A. Maltseva, V. Shkirskiy, G. Lefèvre, P. Volovitch, Effect of pH on $Mg(OH)_2$ film evolution on corroding Mg by in situ kinetic Raman mapping (KRM), Corrosion Science, 153 (2019) 272-282.

[26] I. Ahmed, M. Gasser, Adsorption study of anionic reactive dye from aqueous solution to Mg–Fe–CO_3 layered double hydroxide (LDH), Applied Surface Science, 259 (2012) 650-656.

[27] L. Lv, Defluoridation of drinking water by calcined MgAl-CO_3 layered double hydroxides, Desalination, 208 (2007) 125-133.

[28] E. Nightingale Jr, Phenomenological theory of ion solvation. Effective radii of hydrated ions, The Journal of Physical Chemistry, 63 (1959) 1381-1387.

[29] B. Guo, Y. Xiong, W. Chen, S.A. Saslow, N. Kozai, T. Ohnuki, I. Dabo, K. Sasaki, Spectroscopic and first-principles investigations of iodine species incorporation

into ettringite: Implications for iodine migration in cement waste forms, Journal of Hazardous Materials, (2019) 121880.

[30] J. Naime Filho, F. Silvério, M. Dos Reis, J. Valim, Adsorption of cholate anions on layered double hydroxides: effects of temperature, ionic strength and pH, Journal of Materials Science, 43 (2008) 6986-6991.

[31] S. Wang, B. Gao, Y. Li, A.R. Zimmerman, X. Cao, Sorption of arsenic onto Ni/Fe layered double hydroxide (LDH)-biochar composites, RSC Advances, 6 (2016) 17792-17799.

[32] Q. Tian, B. Guo, S. Nakama, L. Zhang, Z. Hu, K. Sasaki, Reduction of undesirable element leaching from fly ash by adding hydroxylated calcined dolomite, Waste Management, 86 (2019) 23-35.

[33] Y. Zhu, R. Zhu, Q. Chen, M. Laipan, J. Zhu, Y. Xi, H. He, Calcined Mg/Al layered double hydroxides as efficient adsorbents for polyhydroxy fullerenes, Applied Clay Science, 151 (2018) 66-72.

[34] L. Wang, L. Chen, J.L. Provis, D.C.W. Tsang, C.S. Poon, Accelerated carbonation of reactive MgO and Portland cement blends under flowing CO_2 gas, Cement and Concrete Composites, 106 (2020) 103489.

[35] E. Bernard, B. Lothenbach, C. Cau-Dit-Coumes, I. Pochard, D. Rentsch, Aluminum incorporation into magnesium silicate hydrate (MSH), Cement and Concrete Research, 128 (2020) 105931.

[36] E. Bernard, B. Lothenbach, C. Chlique, M. Wyrzykowski, A. Dauzères, I. Pochard, C. Cau-Dit-Coumes, Characterization of magnesium silicate hydrate (MSH), Cement and Concrete Research, 116 (2019) 309-330.

[37] L. Wang, L. Chen, D.-W. Cho, D.C. Tsang, J. Yang, D. Hou, K. Baek, H.W. Kua, C.-S. Poon, Novel synergy of Si-rich minerals and reactive MgO for stabilisation/solidification of contaminated sediment, Journal of Hazardous Materials, 365 (2019) 695-706.

[38] L. Wang, L. Chen, D.C. Tsang, Y. Zhou, J. Rinklebe, H. Song, E.E. Kwon, K. Baek, Y.S. Ok, Mechanistic insights into red mud, blast furnace slag, or metakaolin-assisted stabilization/solidification of arsenic-contaminated sediment, Environment International, 133 (2019) 105247.

[39] B. Walkley, J. Provis, Solid-state nuclear magnetic resonance spectroscopy of cements, Materials Today Advances, 1 (2019) 100007.

[40] D. Nied, K. Enemark-Rasmussen, E. L'Hopital, J. Skibsted, B. Lothenbach, Properties of magnesium silicate hydrates (M-S-H), Cement and Concrete Research, 79 (2016) 323-332.

[41] S. Lu, J. Hu, C. Chen, X. Chen, Y. Gong, Y. Sun, X. Tan, Spectroscopic and modeling investigation of efficient removal of U(VI) on a novel magnesium silicate/diatomite, Separation and Purification Technology, 174 (2017) 425-431.

[42] J.N. Kuhn, Z. Zhao, L.G. Felix, R.B. Slimane, C.W. Choi, U.S. Ozkan, Olivine catalysts for methane-and tar-steam reforming, Applied Catalysis B: Environmental, 81 (2008) 14-26.

[43] D. Zhu, X. Nai, S. Lan, S. Bian, X. Liu, W. Li, Surface modification of magnesium hydroxide sulfate hydrate whiskers using a silane coupling agent by dry process, Applied Surface Science, 390 (2016) 25-30.

Chapter 5

A novel composite of layered double hydroxide/geopolymer for co-immobilization of Cs^+ and SeO_4^{2-} from aqueous solution

5.1 Introduction

Hydrotalcite-like compounds known as layered double hydroxides (LDHs) could be generally represented as [1]: $[M^{2+}_{1-x}M^{3+}_{x}(OH)_2]^{X+}[(A^{n-})\cdot mH_2O]$, where M^{2+} and M^{3+} represent divalent and trivalent cations in the layers, A the interlayer anion with charge n, x the fraction of the trivalent cation and m the number of structural water. According to Chapter 2, LDHs were formed in the NaOH-activated geopolymers with CHT additive, and they showed a good suppressive effect on the Se leaching. It has been also confirmed that the LDHs in geopolymers adsorb SeO_3^{2-} or SeO_4^{2-} during the leaching process, rather than the incorporation of Se oxyanions into LDH interlayers directly. However, it is not available to observe the interfacial interactions between LDHs and geopolymer, and pollutants (cation + anion) when the solidification blocks are prepared. Thus, based on the observation and hypothesis, the main purposes of this chapter are: (1) to develop a new type of composite of layered double hydroxide/geopolymer for co-immobilization of Cs^+ and SeO_4^{2-} which are model radioactive species; (2) to provide the useful evaluation for the simultaneous immobilization of cationic and anionic pollutants using geopolymer.

5.2 Experimental

5.2.1 Material preparation

The geopolymer gel (GEO) was synthesized by the sol-gel method as proposed by a previous study [2]. Specifically, 50 mL of 0.6 M sodium silicate solution (diluted from sodium silicate solution with 37% SiO_2, Chameleon) and 0.3 M aluminum nitrate solution (dissolved from $Al(NO_3)_3\cdot 9H_2O$, 98%, Wako) were respectively prepared and both of them were regulated the pH ($\geqslant$12.5) by using 10 M NaOH. The Al^{3+} solution

was added in drops to the SiO_3^{2-} solution to provide the appropriate composition (Si/Al ratio: 2). The solution was protected in a controlled N_2 atmosphere to prevent possible contamination by CO_2 and meanwhile placed in an ice bath (2 to 5 ℃). After the gel formed, the slurry was stirred for another 24 h at room temperature and thereafter the precipitate and supernatant were separated by the centrifuge (Suprema 21, Tomy). The obtained solid was then washed using pure water to remove the extra alkaline, and freeze-dried for 24 h to get the powdery geopolymer gel.

The MgAl-NO_3-LDH (LDH) was prepared through co-precipitation at room temperature to make it close to the geopolymer synthesis condition. In detail, 50 mL of the nitrate precursor of a 0.04 M Mg^{2+} (dissolved from $Mg(NO_3)_2{\cdot}6H_2O$, 99%, Wako) and 0.02 M Al^{3+} (dissolved from $Al(NO_3)_3{\cdot}9H_2O$, 98%, Wako) was prepared and added in drops to the 50 mL of 0.2 M $NaNO_3$ (99%, Wako) with the pH of 11 maintained by adding 10 M NaOH. The obtained slurry was then agitated at room temperature for 10 h in an N_2 atmosphere. Thereafter, the solid residues were separated by centrifugation, washed for three times using decarbonized water, and then freeze-dried for 24 h.

The MgAl-NO_3-LDH/geopolymer (LDH/GEO) composite was developed using a solution method. Firstly, 1 g pure geopolymer powder was added in a beaker with 50 mL pure water and ultrasonically vibrated for 30 min. Then, the slurry was stirred at 400 rpm for another 30 min. Further 5 min stirring was conducted after adding 0.8584 g $NaNO_3$. 50 mL of the mixture of 0.01 M Mg^{2+} and 0.005 M Al^{3+} was added in drops to the prepared slurry. Afterward, the solution pH was maintained at 11 and continually stirred for 10 h under N_2 protection. Finally, the solid residue and supernatant were separated by centrifugation, and the obtained solid residue was also

washed using decarbonized water for three times, then freeze-dried for 24 h. The solid product obtained here is referred to as MgAl-NO_3-LDH/geopolymer composite.

5.2.2 Co-sorption of Cs^+ and SeO_4^{2-} onto MgAl-NO_3-LDH/geopolymer

The co-sorption of Cs^+ and SeO_4^{2-} was investigated in batch tests onto GEO, LDH, and LDH/GEO composite by being dispersed in the solution containing 1.267 mM SeO_4^{2-} and 0.752 mM Cs^+. The sorption tests under the same condition with and without each other ion were also conducted in order to make the comparisons with the co-sorption results. The influence of contact time on the cosorption of Cs^+ and SeO_4^{2-} onto adsorbents was performed in the solution as well. The sorption isotherm studies were conducted at room temperature on LDH/GEO composite in the single electrolytic solutions containing 0.1–5.0 mM Cs^+ and SeO_4^{2-}, respectively. The influence of co-existing cations on Cs^+ and SeO_4^{2-} sorption over LDH/GEO composite was studied in 0.752 mM Cs^+ solution containing same molar concentrations of nitrate salts of alkali (Li^+, Na^+, and K^+) and alkaline earth metals (Ca^{2+}, Mg^{2+}, and Sr^{2+}) separately with and without SeO_4^{2-}. Similarly, the effect of co-existing anions was investigated in the mixed solutions containing 1.267 mM SeO_4^{2-} and same molar concentrations of sodium salts of NO_3^-, Cl^-, F^-, SO_4^{2-}, CO_3^{2-}, and $H_2PO_4^-$ separately in the presence and absence of Cs^+. It should be noticeable that the solid/liquid ratio in all sorption tests was maintained at 1 g/L and the mixture was stirred at 400 rpm for 4 h (initial pH = 6.5) at room temperature and separated by membrane filtration.

5.2.3 Characterizations

The residual Mg, Al, and Se concentrations in the supernatant were determined

using an inductively coupled plasma optical emission spectrometry (ICP-OES, Perkin Elmer, Optima 8300, US) and the Cs concentration was measured using an inductively coupled plasma mass spectrometry (ICP-MS, Agilent 7500ce, US). XRD patterns of solid samples were determined on a Rigaku Ultima IV XRD (Akishima, Japan): Cu Kα (40 kV, 40 mA) with a Ni filter at a scanning speed of 2° min^{-1} and scanning step of 0.02°. SEM observations were carried out on a VE-9800 SEM (Keyence, Osaka, Japan) with 20 kV acceleration voltage. The FTIR spectra (400-4000 cm^{-1}) were also recorded by a JASCO 670 Plus FTIR spectrometer with a resolution of 4 cm^{-1} employing samples diluted using KBr. Raman spectra were collected using a DXR Smart Raman spectrometer (Thermo Scientific, US) in the region of 4000-100 cm^{-1}, utilizing a 532 nm light source. In addition, N_2 adsorption-desorption curves were measured using a high-precision surface area and pore size distribution analyzer (BEL-Max, BEL, Japan) at –196 ℃. Pretreatment under vacuum at 120 ℃ for 10 h was conducted to remove adsorbed gas and water.

5.3 Results and discussion

5.3.1 Characterization of MgAl-NO_3-LDH/geopolymer composite

The MgAl-NO_3-LDH/geopolymer composite was synthesized by co-precipitation at room temperature and characterized by different physicochemical analysis. The XRD patterns and SEM images of GEO, LDH, and LDH/GEO composite are presented in **Fig. 5.1**. The swell peak at appropriately 27°/2θ was the characteristic of geopolymer, suggesting its amorphous structure. The MgAl-LDH was crystallized in a hydrotalcite-like structure with the d_{003}-spacing of 8.93 Å, which was reflected by interlayer anions of NO_3^-. The LDH/GEO composite showed both

characteristic peaks of MgAl-LDH and geopolymer, implying that LDH was formed and the structure of geopolymer was maintained as well during the synthesis process. Generally, the presence of a large number of anions in the interlayer galleries for charge compensation could lead to the strong electrostatic repulsive forces that could exert the change in the orientation of anions, thereby leading to larger interlayer spacing [3, 4]. Thus, the d_{003}-spacing of MgAl-LDH in the composite LDH/GEO increased from 8.93 Å to 9.13 Å. SEM images showed that geopolymer had a relatively smooth surface. However, the LDH has smaller particle size with rougher surfaces, and it can be known that the surface of LDH/GEO composite had been covered by LDH. This could be confirmed by zeta potential (**Fig. 5.2a**) as well. The zeta potential of GEO and MgAl-LDH were –35.5 and +24.0 mV, respectively. The negative charge of GEO is caused by the AlO_4 tetrahedrons in its structure. The LDH/GEO composite indicated the positive surface charge of +11.8 mV. This implied that the smaller MgAl-NO_3 crystallites had been well distributed on the surface of GEO. Moreover, the particle size distributions of synthesized GEO, LDH, and LDH/GEO composite are shown in **Fig. 5.2b**. It could be found that the average particle size of LDH was much larger than that of GEO. For LDH/GEO composite, its average particle size was in the range between that of GEO and LDH, which could support the above deduction that GEO as a kind of supporter has been uniformly covered by LDH. SEM-EDX elemental analysis of LDH/GEO composite (**Fig. 5.3**) is nearly same to the LDH and GEO consistent of Mg, Al, Si, O, and N, which confirms the homogeneous nature of the composite.

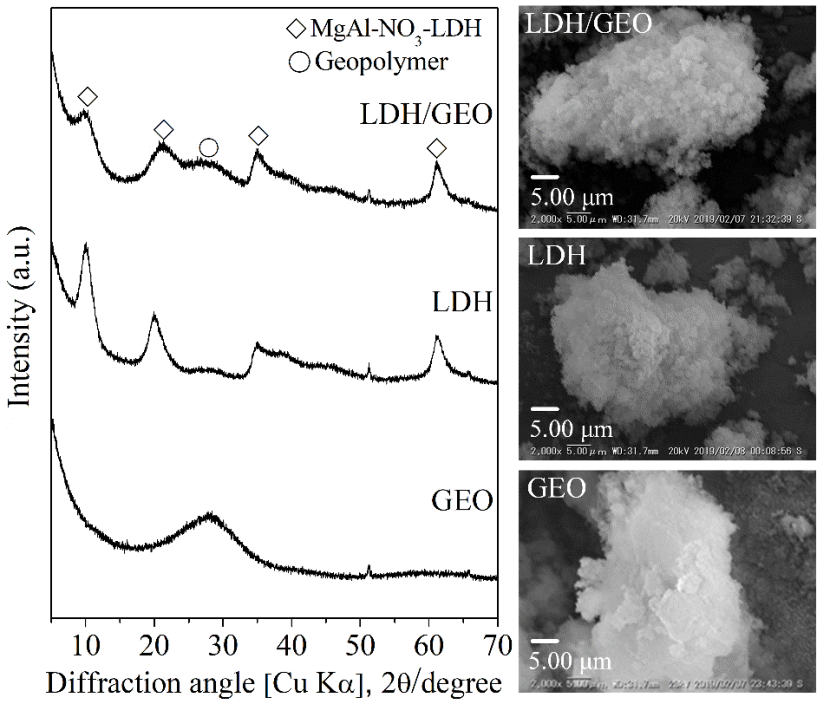

Fig. 5.1 XRD patterns and SEM images of GEO, LDH, and LDH/GEO composite.

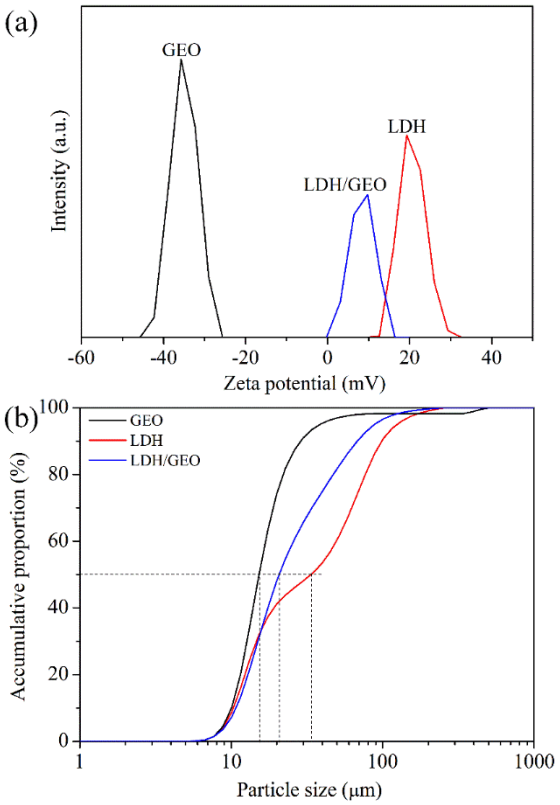

Fig. 5.2 (a) Zeta potential measurements of synthesized GEO, LDH, and LDH/GEO composite (measuring pH: GEO: 9.29, LDH: 9.20, LDH/GEO: 9.38); (b) Particle size distributions of GEO, LDH, and LDH/GEO composite.

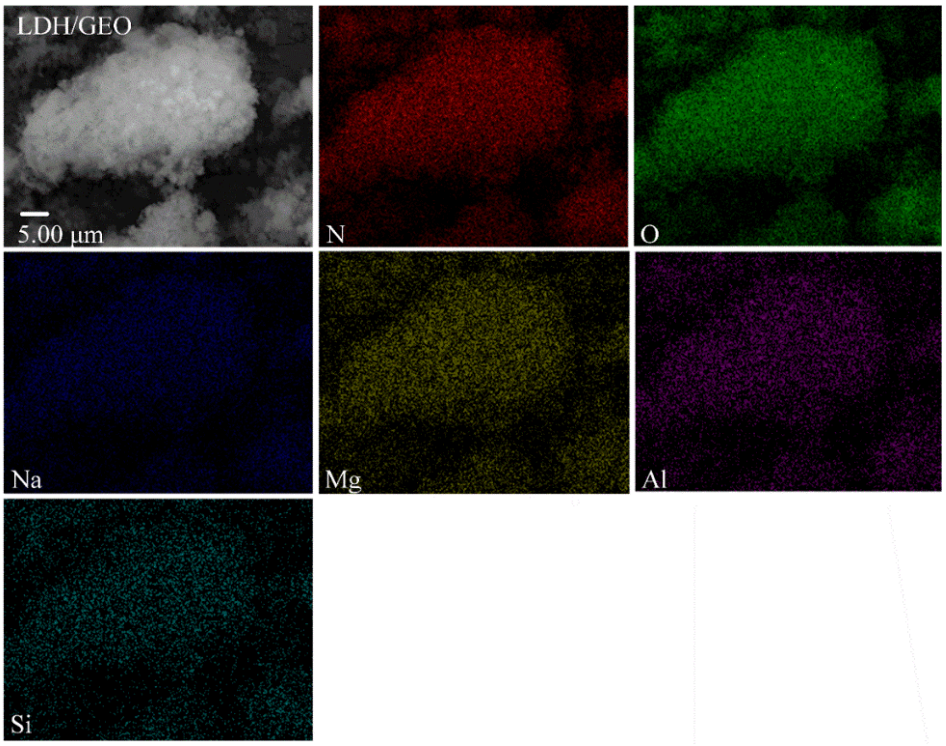

Fig. 5.3 SEM-EDX elemental mapping of MgAl-NO_3-LDH/GEO composite.

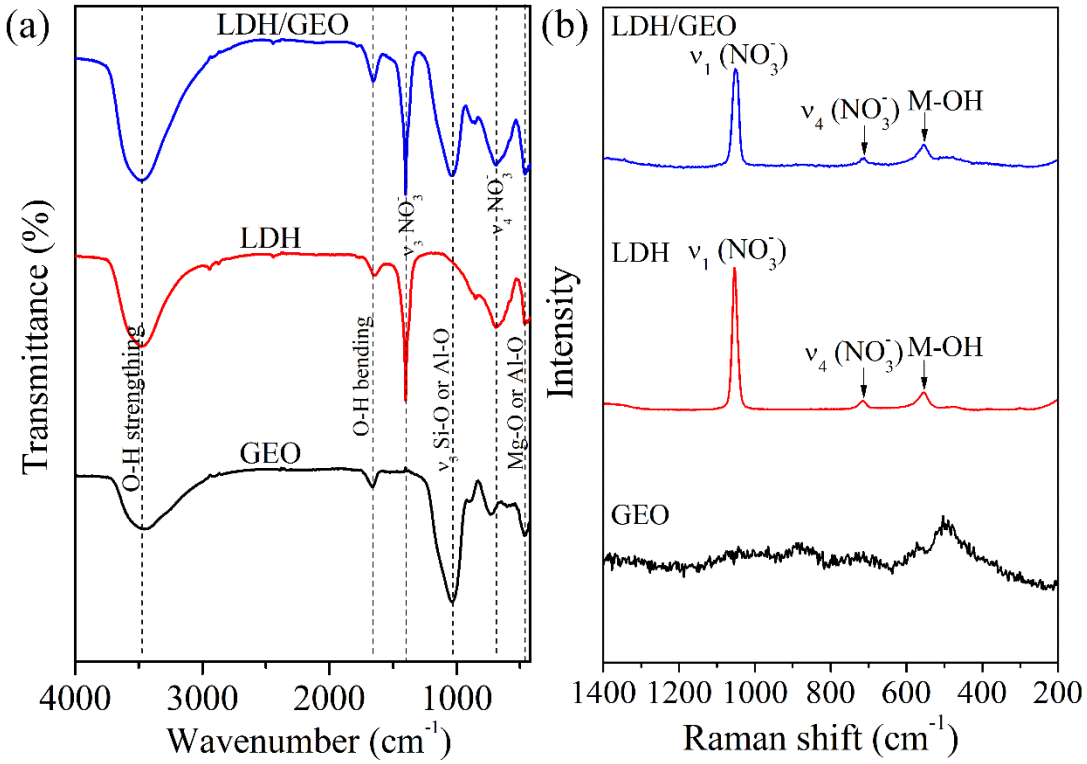

Fig. 5.4 FTIR (a) and Raman (b) spectra of GEO, LDH and LDH/GEO composite.

The FTIR spectra of GEO, LDH, and LDH/GEO composite are presented in **Fig. 5.4a**. The peak at appropriately 3500 cm^{-1} could be assigned to the stretching vibration modes of free and alkoxide OH. Their bending vibrations are located at appropriately 1650 cm^{-1}. All of the synthesized GEO, LDH, and LDH/GEO composite showed the above two characteristic vibrations of OH. The interlayer NO_3^- ions in the MgAl-LDH and its corresponding LDH/GEO composite showed two bands centered at 1401 and 690 cm^{-1} corresponding to asymmetric and symmetric stretching vibrations. The peak at appropriately 1037 cm^{-1} in the spectra of GEO and LDH/GEO composite is ascribed to the asymmetric stretching vibration of Si-O or Al-O in tetrahedrons. The Mg-O or Al-O in octahedrons could be overlapped with the vibration of O-Si-O at appropriately 480 cm^{-1} in FTIR spectra. However, the M-O (M = Mg or Al) band could be observed at 555 cm^{-1} in Raman spectra (**Fig. 5.4b**). Another two peaks at 1051 and 712 cm^{-1} for LDH and LDH/GEO composite are attributed to the symmetric and bending vibrations of NO_3^- ions. In addition, there are only fuzzy peaks representing different vibrations of Si-O or Al-O in tetrahedrons in the GEO spectrum because the Raman signal would be very weak for geopolymer with poor crystallinity.

Elemental analysis indicated that the molar ratios of Si/Al in GEO and Mg/Al in LDH were 1.52 and 2.21, respectively (**Table 5.1**). Geopolymer generally has good physical and chemical stabilities, and when GEO is dispersed in alkaline solution at pH 11 for LDH/GEO composite synthesis, the main component should be maintained. Therefore, the Mg/Al molar ratio of LDH in LDH/GEO composite could be calculated to be 2.73 which presents a deviation from the value of pure MgAl-NO_3-LDH. This might be because of the charge interactions between geopolymer surface and newly formed LDH layer and $Al(OH)_4^-$ species in solution. Based on the elemental

composition of LDH/GEO composite determined by ICP-OES, the content (wt%) of LDH and GEO could also be calculated to be 46.02% and 53.98%, respectively. In addition, the specific surface areas of pure LDH and GEO were 59.2 and 122.6 m^2/g, respectively (**Table 5.1**). It seems that there are more mesoporous pores in the LDH/GEO composite compared to the individuals of GEO and LDH according to the hysteresis on the adsorption-desorption curves of them (**Fig. 5.5**). According to the mass ratio of LDH and GEO in LDH/GEO composite, the expected surface area should be approximately 99.6 m^2/g based on the physically mixing of pure GEO and LDH. However, its surface area was much higher (134.1 m^2/g) than the calculated value. Furthermore, the pore volume from the desorption curve was 0.848 cm^3/g which was lower than the expected value (0.948 cm^3/g). This confirms that the surface of geopolymer has been well covered by MgAl-LDH, which greatly contributes to the surface area of the LDH/GEO composite.

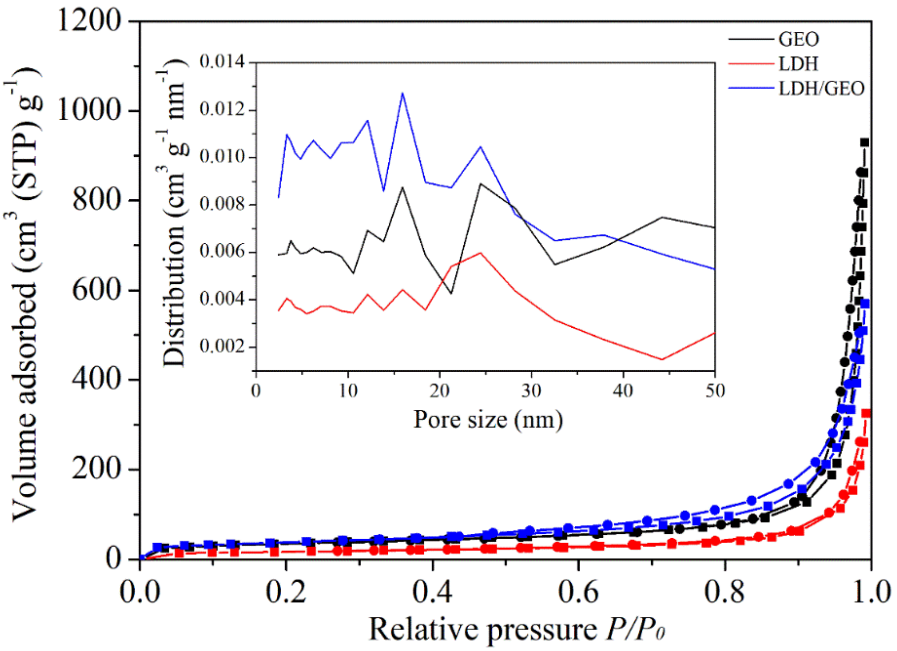

Fig. 5.5 Nitrogen adsorption–desorption isotherms of GEO, LDH and LDH/GEO composite. The inset shows the corresponding pore size distribution curves determined by the BJH method.

Table 5.1 Elemental compositions and specific surface areas of GEO, LDH and LDH/GEO.

Sample	Si/Al molar ratio[a]	Mg/Al molar ratio[a]	LDH (wt%)	GEO (wt%)	Exchanged NO_3^- (mmol/g)[b]	S_{BET} (m^2/g)	Pore volume (cm^3/g)
GEO	1.52	-	-	100	-	122.6	1.391
LDH	-	2.21	100	-	2.946	59.2	0.428
LDH/GEO	0.88	1.14	46.02	53.98	1.612	134.1	0.848

[a]Calculated based on ICP analysis results, [b]Ion chromatographic analysis was performed by exchanging the interlayer anion with 0.1 M Na_2CO_3.

5.3.2 Immobilization of Cs^+ and SeO_4^{2-} in LDH/GEO composite

The cosorption results of Cs^+ and SeO_4^{2-} using GEO, LDH, and LDH/GEO were shown in **Fig. 5.6**. MgAl-NO_3-LDH presented very poor ability to immobilize Cs^+ because of the positive charge on the surface. Differently, approximately 0.62 mmol/g of Cs^+ sorption amount was obtained by GEO which possessed permanent negative charge provided by AlO_4 tetrahedrons. The LDH/GEO composite showed a lower Cs^+ sorption capacity (0.34 mmol/g) due to the fewer sorption sites compare to parent GEO. The isotherm study (below) confirms that the adsorption could achieve the equilibrium at the designated concentration. Thus, the sorption capacity of Cs^+ normalized for a unit mass of GEO was approximately 0.63 mmol/g which was similar to the value obtained by pure GEO. This implied that the surface of GEO covered by MgAl-LDH did not affect the sorption of Cs^+, even though a part of negative adsorption sites had been compensated by LDH as zeta potential results indicated. This could be because Cs^+ ions can diffuse into the internal space through the irregular channels made by the connection of SiO_4 and AlO_4 tetrahedrons in geopolymer. Conversely, the sorption capacity of SeO_4^{2-} onto LDH/GEO composite normalized to LDH (approximately 0.90

mmol/g) was still lower than that obtained by pure LDH (1.21 mmol/g), which could be explained by charge compensation as stated above.

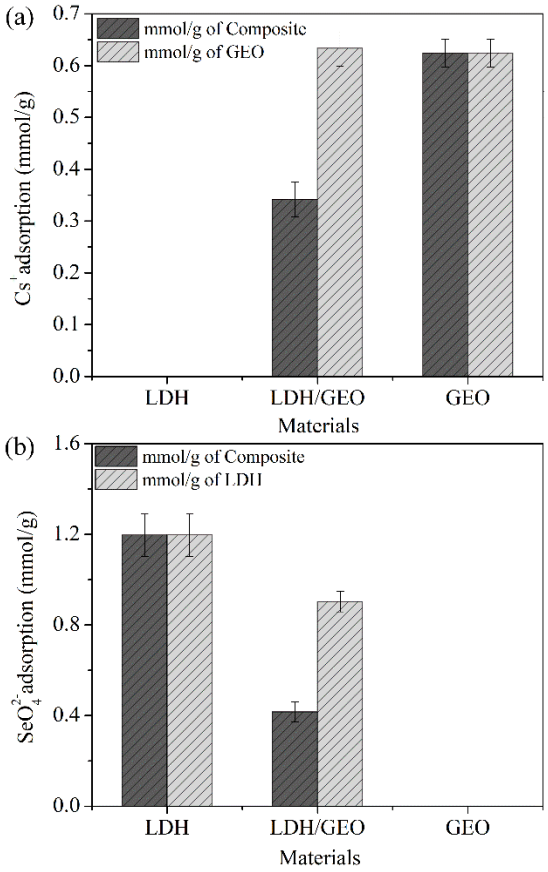

Fig. 5.6 Co-sorption of (a) Cs^+ and (b) SeO_4^{2-} onto GEO, LDH and LDH/GEO composite.

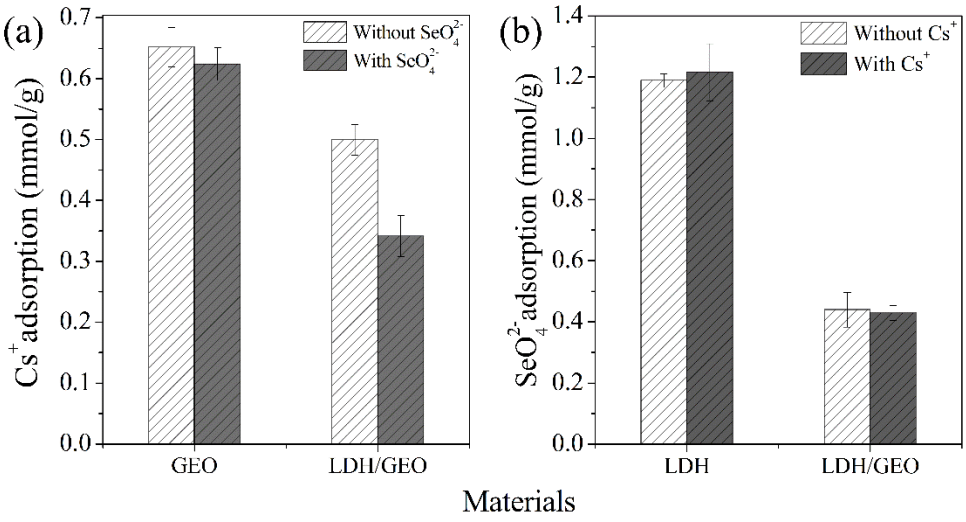

Fig. 5.7 Sorption of (a) Cs^+ and (b) SeO_4^{2-} onto GEO, LDH, and LDH/GEO composite with and without another ion.

Fig. 5.7 presents the sorption results of Cs^+ and SeO_4^{2-} with and without the co-existing ions. It could be found that the presence of SeO_4^{2-} has a negative effect on the sorption of Cs^+ onto LDH/GEO composite. For both GEO and LDH/GEO composite, the sorption amounts of Cs^+ became lower in the presence of SeO_4^{2-}. However, the sorption capacity of SeO_4^{2-} seemed not to be influenced by the presence of Cs^+. This might be due to the presence of the ion-pair complex of $[CsSeO_4]^-$ in the binary solution, and a part of Cs^+ could be detained because of charge repulsion with the geopolymer surface [5-8]. Meanwhile, it could be attracted by the positively charged surface of LDH. Generally, the interaction between Cs^+ and SeO_4^{2-} in the ion-pair complex of $[CsSeO_4]^-$ should be very weak, and it could be easily destructed by the strong positive charge on LDH layer. Then, the released SeO_4^{2-} from the complex was quickly immobilized by LDH.

5.3.3 Influence of contact time on the cosorption of Cs^+ and SeO_4^{2-}

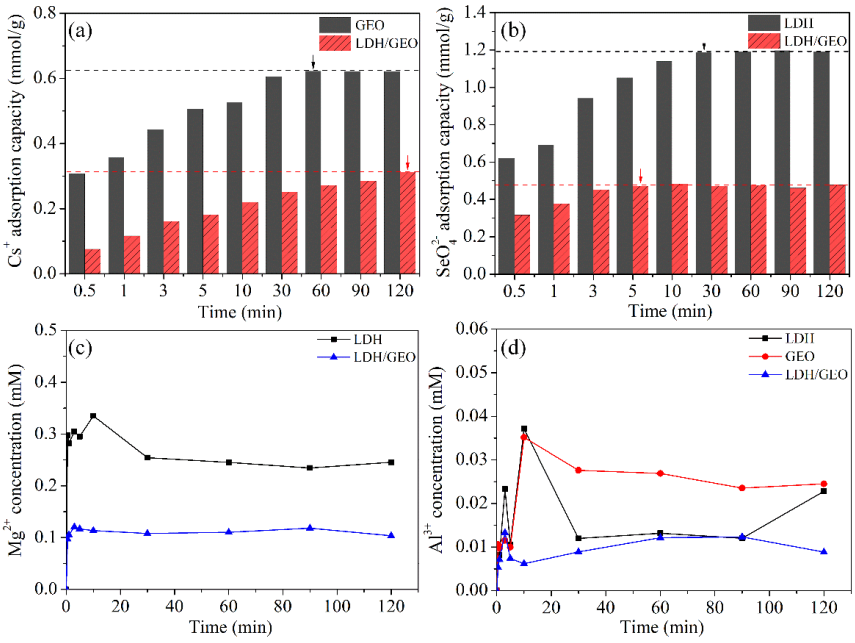

Fig. 5.8 Effect of sorption time on the sorption capacities of (a) Cs^+ and (b) SeO_4^{2-} onto MgAl-LDH/GEO composite; the dissolved (c) Mg and (d) Al concentrations. The dash lines represent the equilibrium adsorption capacity.

The influence of the contact time on the cosorption of Cs^+ and SeO_4^{2-} onto GEO, LDH, and LDH/GEO composite are shown in **Fig. 5.8**. From the above discussion, it could be known that GEO and LDH provide the corresponding sorption sites for Cs^+ and SeO_4^{2-}, respectively. The sorption amount of Cs^+ onto GEO increased with the contact time and reached the equilibrium within 1 h (**Fig. 5.8a**). However, the required time to reach the equilibrium became longer than 2 h for the sorption of Cs^+ onto LDH/GEO composite. This could be due to the reduction of negative sites on the surface of GEO, as stated above, and the sorption of Cs^+ onto the LDH/GEO composite should be controlled by particle diffusion. Conversely, the SeO_4^{2-} sorption onto LDH/GEO reached equilibrium at approximately 5 min, which was much faster than the sorption of SeO_4^{2-} onto pure LDH. Therefore, the well-distributed LDH on the surface of GEO makes the ion-exchange process easier. On the other hand, the concentration of dissolved Mg^{2+} from LDH was almost two times higher than that from LDH/GEO composite, and this was approximately consistent with the proportion of LDH in the composite. In addition, the dissolved Al concentrations were much lower than the Mg concentration, and no regular changes occurred to them. The specific sorption characteristics were expressed using pseudo-first-order and pseudo-second-order kinetics, and the diffusion processes were studied using the Boyd equation [9].

Pseudo first-order: $$\log(q_e - q_t) = \log q_e - \frac{k_1}{2.303} t \quad (5.1)$$

Pseudo second-order: $$\frac{t}{q_t} = \frac{1}{k_2 q_e^2} + \frac{t}{q_e} \quad (5.2)$$

where q_e and q_t (mmol/g) are the amounts of metal ions sorbed onto adsorbent at equilibrium and at time t, respectively, and k_1, k_2 are the rate constants (min^{-1}) of the pseudo-first-order and pseudo-second-order equations, respectively.

The related kinetic parameters calculated from the linear relationships of $\log(q_e - q_t)$ versus t, and t/q_t versus t (**Fig. 5.9a** and **5.9b**) are shown in **Table 5.2**. It could be obviously known that pseudo-second-order is much more befitting than pseudo-first-order for both Cs^+ and SeO_4^{2-} sorbed onto GEO, LDH, and LDH/GEO composite based on the comparisons of R^2 and deviations between experimental and calculated q_e. Thus, the sorption processes were controlled by chemical sorption. The k_2 and h reveal that LDH/GEO has a higher adsorption rate for SeO_4^{2-}, and nevertheless a lower sorption rate for Cs^+. The specific surface area of LDH in the LDH/GEO composite might control the sorption speed of SeO_4^{2-}. For Cs^+ sorption, the Boyd equations were applied to fit the experimental data to determine the kinetics governing the overall removal rate of the sorption process.

Boyd equation: $$Bt = -\ln\frac{\pi^2}{6}(1-F) \quad (5.3)$$

$$Bt = 2\pi - \frac{\pi^2 F}{3} - 2\pi(1-\frac{\pi F}{3})^{1/2} \quad (5.4)$$

where F is the fractional attainment of equilibrium at time t ($F = q_e/q_t$), B the time constant. Specifically, Equation (4) is used for values of F ranging from 0 to 0.85 and Equation (3) for F ranging from 0.85 to 1 [10]. The linearity test of the Bt versus time plots is generally employed to distinguish between film and particle diffusion controlling the sorption process. If the plot is a straight line that passes through the origin, then the sorption is controlled by the particle diffusion mechanism; otherwise, it is governed by film diffusion. The plot of Bt versus t for Cs^+ sorption onto GEO was linear but obviously did not pass through the origin (**Fig. 5.9c**), which implied that the sorption process could be controlled by film diffusion. However, the plot for Cs^+ sorption onto LDH/GEO composite was linear and almost passed through the origin. This could indicate that particle diffusion controlled the Cs^+ sorption onto LDH/GEO,

as the assumption stated earlier. In addition, the sorption processes of SeO_4^{2-} on both LDH and LDH/GEO composite were controlled by film diffusion.

Table 5.2 The calculated parameters of kinetic models for Cs^+ and SeO_4^{2-} sorbed onto GEO, LDH, and LDH/GEO composite.

Kinetic model	Parameter	Cs^+		SeO_4^{2-}	
		GEO	LDH/GEO	LDH	LDH/GEO
Pseudo-first-order	$q_{e,\,exp}$ (mmol/g)	0.62	0.34	1.19	0.42
	$q_{e,\,cal}$ (mmol/g)	0.22	0.19	0.33	0.08
	k_1 (min^{-1})	0.075	0.015	0.116	0.0875
	R^2	0.985	0.896	0.944	0.9101
Pseudo-second-order	$q_{e,cal}$ (mmol/g)	0.63	0.31	1.20	0.47
	k_2 (h^{-1})	1.492	0.876	1.408	16.295
	h (mmol g^{-1} min^{-1})	0.59	0.08	2.02	3.64
	R^2	0.999	0.995	0.999	0.999

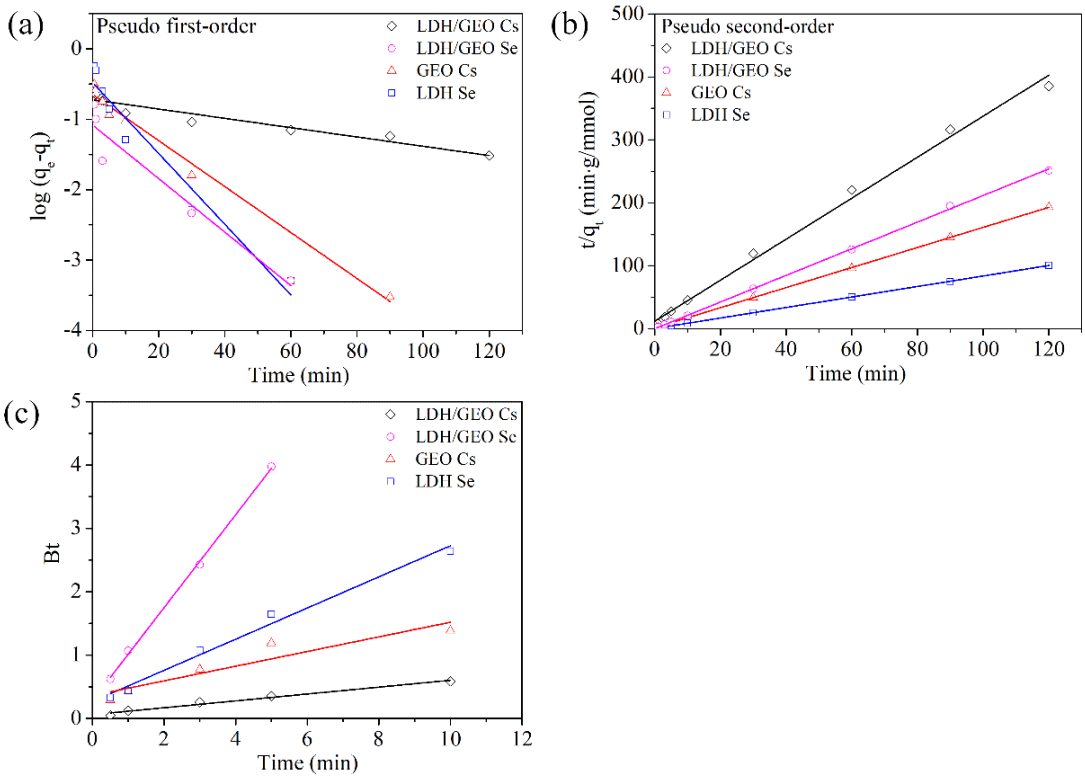

Fig. 5.9 Pseudo-first-order kinetic plots (a), pseudo-second-order kinetic plots (b) and plots of Bt versus t (c) for the sorption of Cs^+ and SeO_4^{2-} onto the GEO, LDH and LDH/GEO composite.

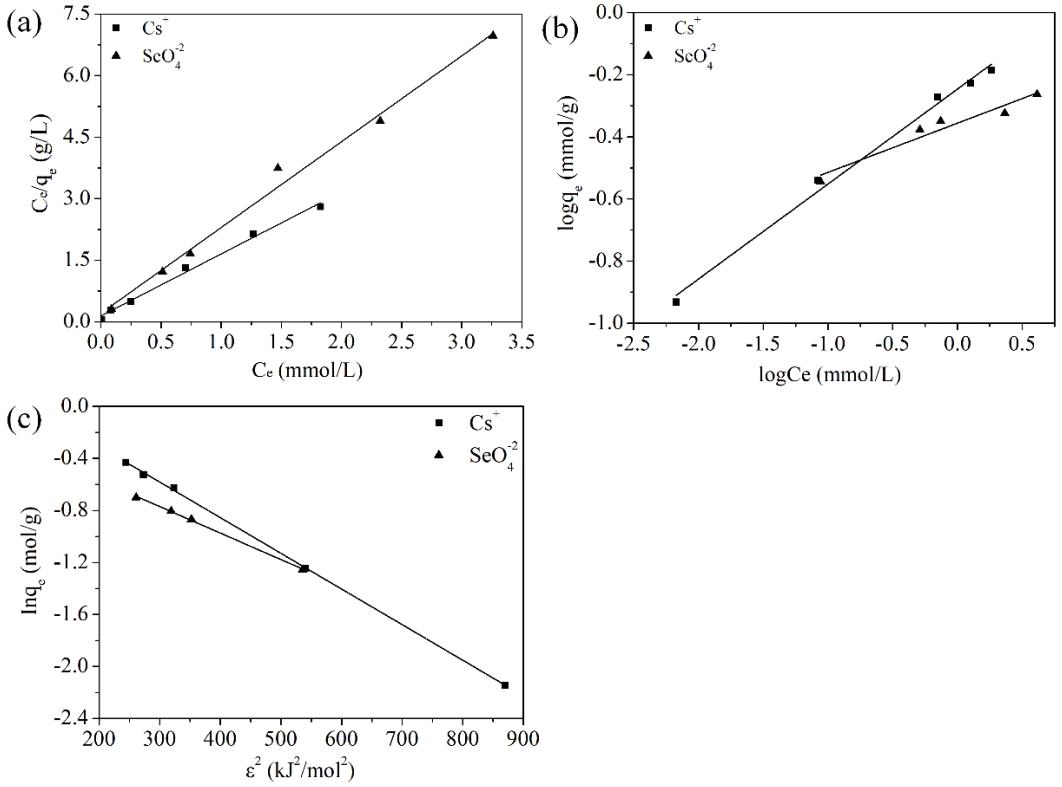

Fig. 5.10 Linear forms of (a) Langmuir, (b) Freundlich and (c) Dubinin-Radushkevitch isotherms of Cs^+ and SeO_4^{2-} sorption onto LDH/GEO in the single electrolytic solution.

5.3.4 Sorption isotherms of Cs^+ and SeO_4^{2-} in the single electrolytic solution

The sorption isotherms of Cs^+ and SeO_4^{2-} onto LDH/GEO composite were explored in single electrolytic solutions, as shown in **Fig. 5.10**. The experimental sorption data of Cs^+ and SeO_4^{2-} was well fit with Langmuir and Freundlich nonlinear sorption isotherm models as below [9].

Langmuir equation: $\frac{C_e}{q_e} = \frac{1}{Q_m b} + \frac{1}{Q_m} c_e$ (5.5)

Freundlich equation: $\log q_e = \log K_f + \frac{1}{n} \log C_e$ (5.6)

where q_e is the amount of metal ion sorbed onto adsorbent (mmol/g), C_e the equilibrium concentration of metal ion in the equilibrium solution (mmol/L). Q_m the monolayer adsorption capacity (mmol/g) and b the constant related to the free energy

of adsorption. K_f is constant indicative of the relative sorption capacity of adsorbent (mmol/g), and $1/n$ is the constant indicative of the intensity of the sorption process. If the value of n is greater than 1, it means a strong interaction between the surface of the adsorbent and adsorbate.

For Cs^+ sorption, both the Langmuir and Freundlich isotherm models were fitted preferably, evidenced by better R^2 (**Table 5.3**), and the value of n from the Freundlich model was higher than 1. This indicated that the sorption of Cs^+ onto the LDH/GEO composite could be monolayer, and the removal process was favorable on this composite. Similarly, the sorption of SeO_4^{2-} followed Langmuir monolayer adsorption. In order to further study the nature of these sorption processes, the Dubinin–Radushkviech isotherm was adopted in the form [11]:

$$\ln q_e = \ln q_m - \beta\varepsilon^2 \tag{5.7}$$

where q_m is the maximum amount of ion that can be sorbed onto unit weight absorbent (mmol/g), and β is the constant related to the sorption energy (mol^2/KJ^2). ε is the Polanyi potential = $RT \ln(1+1/C_e)$, where R is the gas constant (8.314 J/mol K), and T is the absolute temperature (K).

In addition, the average free energy of sorption could be the free energy change when the ions are transferred to the surface of adsorbent from the solution. The calculation formula is expressed in equation (8).

$$E = (-2\beta)^{-1/2} \tag{5.8}$$

where E is the free energy (kJ/mol). Generally, the free energy in the range of 8–16 kJ/mol indicates the cation exchange process, and the value less than 8 kJ/mol suggests the physical adsorption, and more than 16 kJ/mol implies the chemical adsorption [11].

Table 5.3 Langmuir, Freundlich and D-R model parameters for the sorption of Cs^+ and Sr^{2+} onto LDH/GEO composite.

Isotherm	Parameter	Cs^+	SeO_4^{2-}
Langmuir	Q_0 (mmol/g)	0.662	0.478
	$b\times10^3$ (L/mmol)	10.585	10.166
	R^2	0.992	0.989
Freundlich	n	3.271	6.314
	K_f (mmol/g)	0.568	0.441
	R^2	0.991	0.925
D-R model	β (mol^2/kJ^2)	0.002	0.002
	q_m (mmol/g)	1.272	0.794
	R^2	0.999	0.985
	E (kJ/mol)	14.228	15.467

The D-R plots of ln q_e versus ε^2 for these sorption processes are given in **Fig. 5.10c**, and the statistical results are shown in **Table 5.3**. It can be seen that the sorption process of Cs^+ onto LDH/GEO composite has the free energies of 14.228 kJ/mol. In addition, the free energy value for the sorption of SeO_4^{2-} onto LDH/GEO composite was 15.467 kJ/mol. This obviously indicated that the sorption processes for both Cs^+ and SeO_4^{2-} are dominantly ion exchange without any secondary chemical interactions.

5.3.5 Effect of coexisted anions and cations on the sorption of Cs^+ and SeO_4^{2-} onto LDH/GEO composite

The effect of the coexisting cations on the removal of Cs^+ with or without SeO_4^{2-} was explored and shown in **Fig. 5.11**. No matter which cation existed in the solution, the sorption capacities of Cs^+ without SeO_4^{2-} were always higher than that with SeO_4^{2-}, which confirmed the earlier explanation. The results also indicated that divalent ions (Mg^{2+}, Ca^{2+}, and Sr^{2+}) had greater impacts than monovalent ions (Li^+, Na^+, and K^+) on the Cs^+ adsorption onto LDH/GEO. Furthermore, the cation with a larger atomic

number such as K^+, Sr^{2+} could have more influence on the Cs^+ sorption. Therefore, the effects of other metal cations on the Cs^+ sorption in the multicomponent system (Cs^++other ions) are arranged as follows: $Na^+ < Li^+ < Mg^{2+} < K^+ < Ca^{2+} < Sr^{2+}$. The influence order of these coexisting cations has a partly positive correlation with the increase in the valences and decrease in the radii of the corresponding metallic ions. In addition, the removal capacities of SeO_4^{2-} in the tricomponent system ($Cs^+ + SeO_4^{2-}$ + other cation) were almost unaffected by these cations (**Fig. 5.11b**).

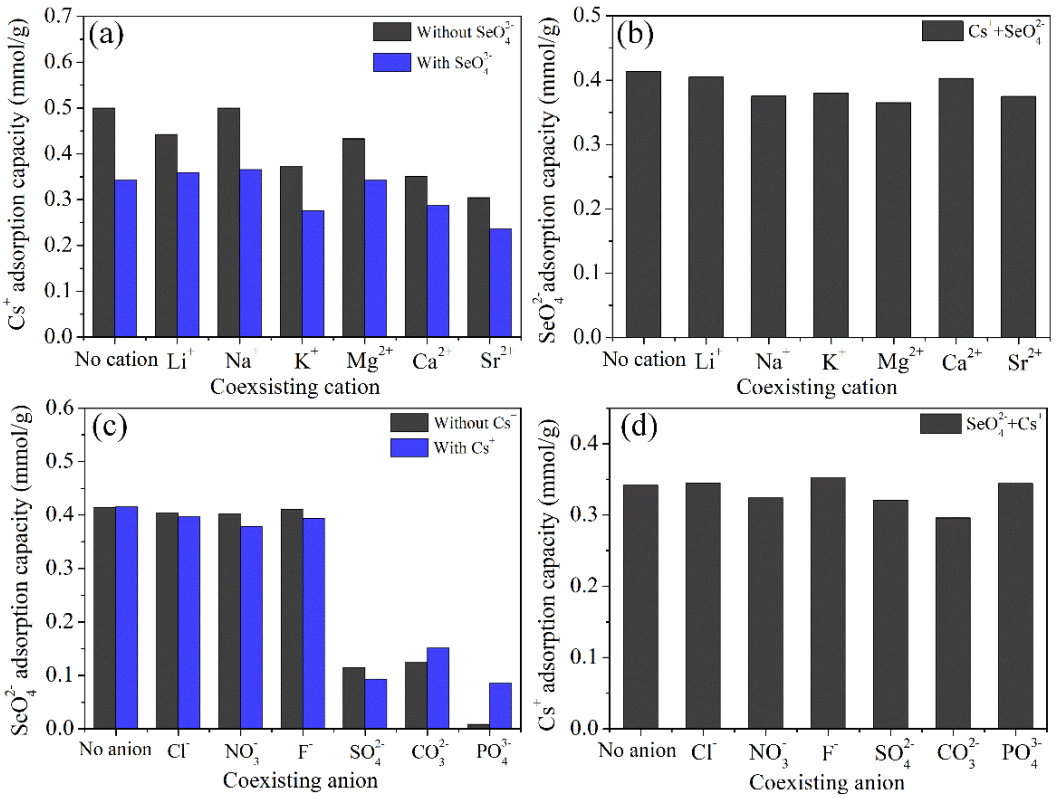

Fig. 5.11 Effects of coexisting cations and anions on the sorption of (a) Cs^+ and SeO_4^{2-} in bicomponent solution, the error is within 5%.

Similarly, the effect of coexisting anions on the removal of SeO_4^{2-} onto the LDH/GEO composite was studied with and without Cs^+, as shown in **Fig. 5.11c**. The influence of monovalent anions (Cl^-, NO_3^-, F^-) on the uptake of SeO_4^{2-} was much less, while the multivalent anions showed a larger effect. The decrease in the removal capacities of SeO_4^{2-} in both binary and ternary systems could be directly related to the

Miyata series of anion preference for LDH [12]. Multivalent anions could have higher electrostatic force with the LDH layer than monovalent anions. Similar studies have also indicated that LDH has higher affinity with higher charge density and divalent anions than monovalent anions [13]. It should be noted that the presence of Cs^+ has less effect on the sorption of SeO_4^{2-} except the case of PO_4^{3-}. The sorption amount of SeO_4^{2-} was much improved in the presence of Cs^+ compared to that without Cs^+. This might be due to the formation of a stronger ion-pair complex between Cs^+ and PO_4^{3-}. **Fig. 5.11d** showed the influence of co-anions on the sorption of Cs^+ in the tricomponent system (SeO_4^{2-}+ Cs^++other anion). The extra anion in the solution does not have a large effect on the uptake of Cs^+ on the composite. This implies that the formation of ion-pair complexes could only affect the sorption process to a certain extent.

5.3.6 Mechanisms of Cs^+ and SeO_4^{2-} cosorption onto the MgAl-LDH/GEO composite

Geopolymer is always regarded as the zeolite precursor, and ion exchange ability has been considered as its special characteristics. In the present study, it has been found that the sorption capacity of Cs^+ by LDH/GEO normalized for the unit mass of GEO does not show a decrease compared to that obtained by pure GEO, even though the surface negative charge of GEO has been partially compensated by the positive charge of LDH layer. This could be best explained by the particle diffusion inside the geopolymer structure, corroborated by the kinetic results. Furthermore, this kind of diffusion was enhanced by the coverage of MgAl-LDH onto the surface of GEO because the Na^+ ions located in the surface layers of GEO would move out or go deeper inside the structure due to the charge repulsion between LDH layer and Na^+ ion.

However, there is generally no cage or channel in the structure of geopolymer as zeolite because of its amorphous essence [14]. Thus, this kind of diffusion should be restricted in a certain distance around the ring entrance gate, and it would be controlled by the local structure of geopolymer, which was defined as "pocket diffusion". **Fig. 5.12** shows the XRD patterns of GEO, LDH, and LDH/GEO composite after cosorption of Cs^{+} and SeO_4^{2-}. For GEO, there was almost no change in terms of the main broad peak compared to its XRD pattern before sorption. This is mainly because the properties of geopolymer are relatively stable, and the structure would not change through ion exchange with other cations. Differently, the structure of LDH would have some changes after ion exchange with other anions. The FTIR and Raman spectra (**Fig. 5.13**) of LDH and LDH/GEO after sorption indicate that SeO_4^{2-} has been immobilized in LDH and LDH/GEO composite, respectively. Meanwhile, the contamination caused by CO_3^{2-} has also been confirmed. On the other hand, the peak intensity at d_{003} of pure LDH after sorption (**Fig. 5.12**) decreased after sorption, which could be due to the fact that different anions (NO_3^-, SeO_4^{2-}, CO_3^{2-}) existing in the interlayer space of LDH could enhance the disorder of layer arrangement because these anions possess different radii (NO_3^-: 0.179 nm, SeO_4^{2-}: 0.249 nm, CO_3^{2-}: 0.178 nm) [15]. However, the peak at d_{003} of LDH in LDH/GEO composite surprisingly disappeared after sorption. The existence of 110 peak at approximately 61° indicated the existence of the MgAl hydroxide layers. The structure of LDH in the composite might become much more disordered than the pure LDH after sorption, and on the other hand, less content of LDH (46.02%) in LDH/GEO composite might also lead to the obscure changes.

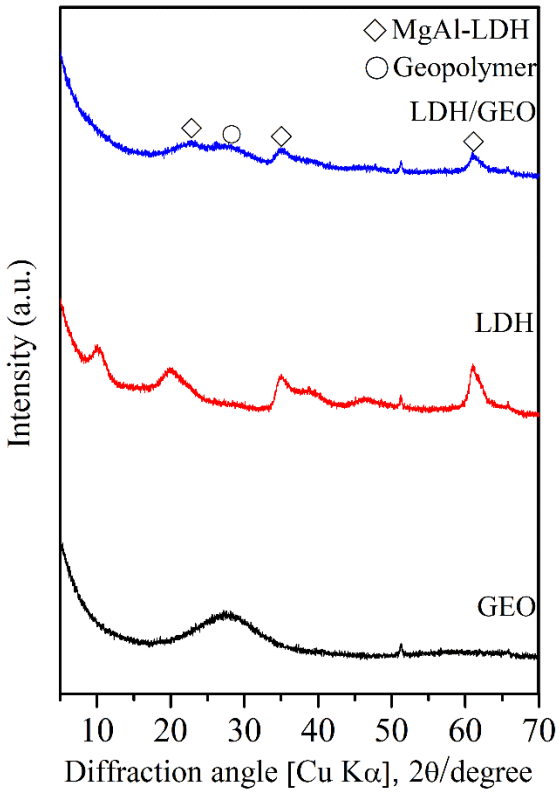

Fig. 5.12 XRD patterns of GEO, LDH, and LDH/GEO composite after cosorption of Cs^{+} and SeO_4^{2-}.

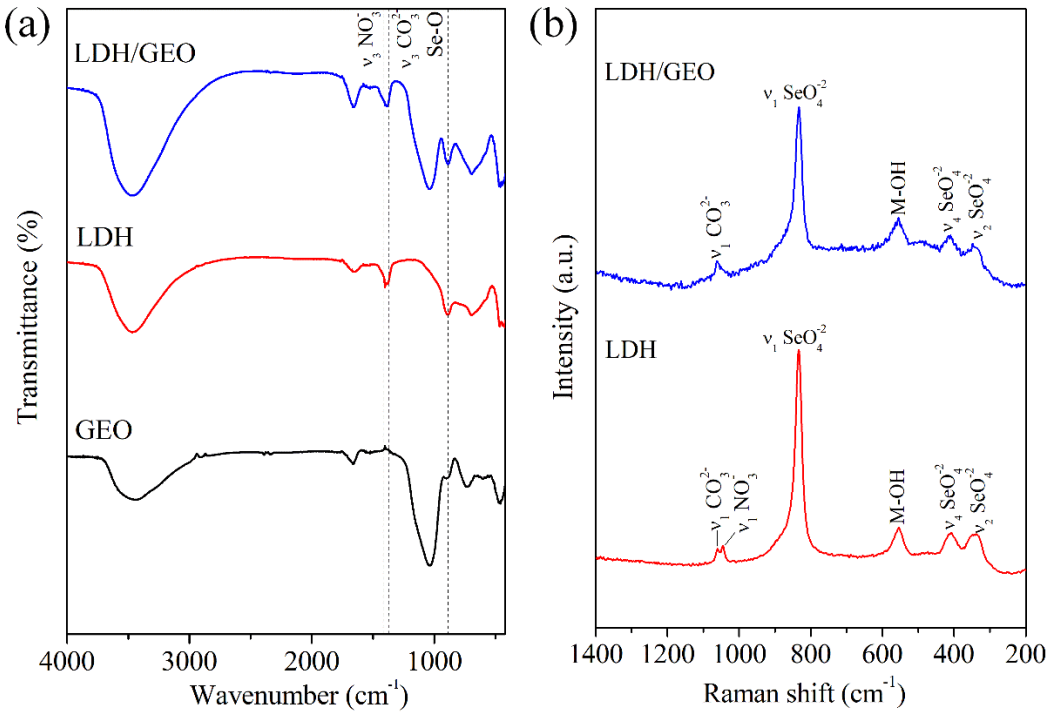

Fig. 5.13 FTIR (a) and Raman (b) spectra of GEO, LDH and LDH/GEO composite after cosorption of Cs^{+} and SeO_4^{2-}.

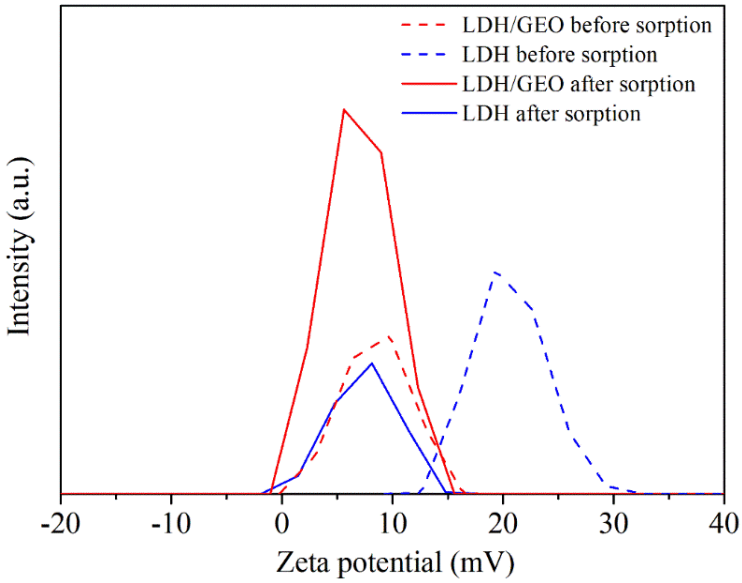

Fig. 5.14 Zeta potential measurements of synthesized LDH and LDH/GEO composite before and after cosorption of Cs^+ and SeO_4^{2-} (pH 9.2–9.4).

Zeta potential measurements were conducted for LDH and LDH/GEO composite after cosorption of Cs^+ and SeO_4^{2-} (**Fig. 5.14**). The zeta potentials of LDH and LDH/GEO after sorption were changed to 7.63 and 6.41 mV (pH 9.26). This obviously implied that electrostatic surface adsorption was also one of the mechanisms for SeO_4^{2-} removals. In addition, the change of zeta potentials of LDH before and after sorption was 16.37 mV, and then the changes of zeta potential caused by SeO_4^{2-} per mmol could be calculated as 13.46 mV·g/mmol. Assuming that the structure changes of LDH in LDH/GEO composite are similar to the pure LDH after sorption and the negative sites provided by geopolymer are fixed, the reduction of zeta potential for LDH/GEO after sorption should be approximately 5.59 mV. This was rightly close to the experimental value (5.41 mV), which indicated that the number of negative sites from geopolymer was not changed and furthermore the distribution of LDH on the surface of geopolymer was still maintained as that before adsorption. Moreover, the SEM-EDX measurement of the LDH/GEO composite after cosorption of Cs^+ and SeO_4^{2-} indicated

that the elemental distribution of LDH/GEO composite including Mg, Al, and Si, etc. was well consistent with that before sorption, and the element distributions of Cs and Se are overlapped with the components of LDH/GEO composite (**Fig. 5.15**). Therefore, the driving force for Cs^+ sorption under certain concentration should be a constant value at the initial stage. As indicated earlier, the sorption of Cs^+ by LDH/GEO composite in the presence of SeO_4^{2-} was lower than that without SeO_4^{2-} due to the formation of the ion-pair complex of $[CsSeO_4]^-$. The attraction force between geopolymer and Cs^+ was much stronger than the interaction between Cs^+ and SeO_4^{2-} at the initial stage. The negative sites on the geopolymer surface were compensated by Cs^+, and then the affinities decreased and were gradually equal to the interaction force between Cs^+ and SeO_4^{2-}. Based on the results from **Fig. 5.11**, when other anions including Cl^-, NO_3^- et al. were added into the mixed solution (Cs^+ + SeO_4^{2-}) separately, the sorption amounts of Cs^+ were not seriously affected compared to that without anion addition. Different anions might have different stability constant to form ion-pair complexes with Cs^+. These interactions could be very weak, and it also depends on the concentrations of ions in the solution. Thus, adding more anions did not contribute to more strong ion-pair complexes, which might be controlled by the Cs^+ concentration. Therefore, the attraction force between geopolymer and Cs^+ controlled the final sorption amount, and the sorption process is shown as **Fig. 5.16**.

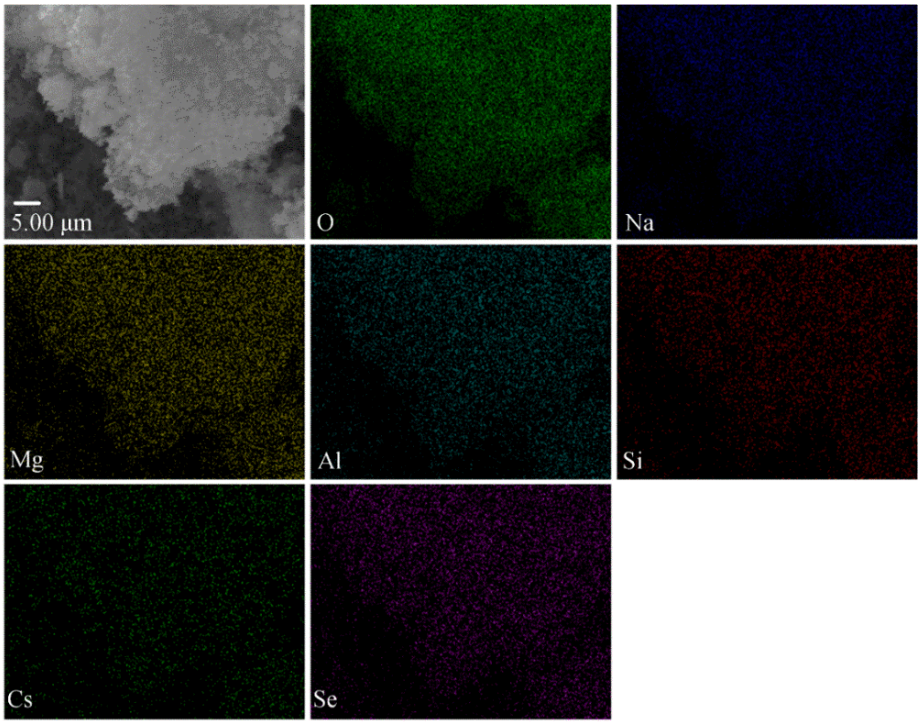

Fig. 5.15 SEM-EDX elemental mapping of MgAl-NO_3-LDH/GEO composite after cosorption of Cs^+ and SeO_4^{2-}.

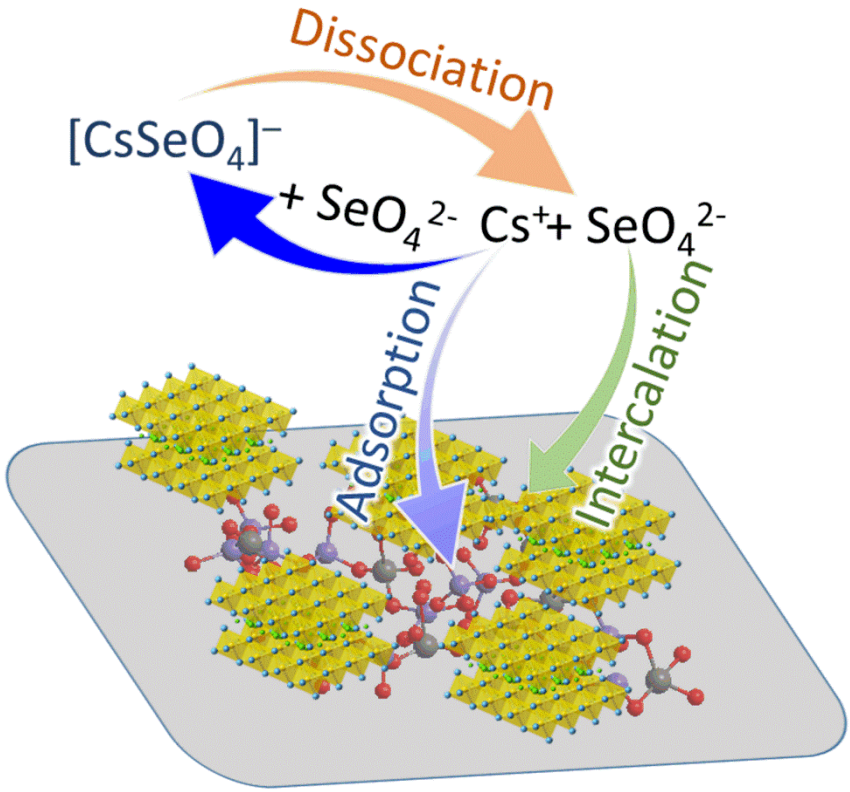

Fig. 5.16 Schematic illustration for the sorption process.

5.4 Conclusions

Hydrotalcite-like minerals can be formed during geopolymeration in the presence of MgO. In the present study, a novel composite of layered double hydroxide/geopolymer (LDH/GEO) were synthesized using sol-gel and co-precipitation. It was found that the surface of geopolymer was homogeneously covered by the LDH platelets, evidenced by SEM-EDX, particle size, and zeta potential measurements. The ability of LDH/GEO to sorb Cs^+ was maintained as that of pure GEO. In the binary system (Cs^+ + SeO_4^{2-}), the sorption amount of Cs^+ onto both GEO and LDH/GEO would decrease due to the existence of ion-pair $[CsSeO_4]^-$. However, it has less effect on the sorption of SeO_4^{2-} onto both pure LDH and LDH/GEO, and this could be because of the stronger attraction of LDH layer to SeO_4^{2-}. On the other hand, film diffusion governed the sorption process of Cs^+ onto pure GEO via ion exchange. However, the sorption of Cs^+ onto LDH/GEO composite was controlled by particle diffusion. This could be explained by the fact that the Na^+ ions located in the surface layers of GEO would move out or go deeper inside the structure because of the charge repulsion between LDH layer and Na^+ ions. "Pocket diffusion" was defined because this kind of diffusion would be restricted to a certain distance around the ring entrance gate due to the amorphous essence of GEO. For SeO_4^{2-} sorption, it occurred by ion-exchange with the interlayer NO_3^- and surface sorption. Importantly, the sorption of SeO_4^{2-} onto LDH/GEO composite is much faster than the case of pure LDH. The current results demonstrate that the LDH/GEO composite could be a kind of cost-effective, environmentally friendly material for co-immobilization of Cs^+ and SeO_4^{2-}.

References

[1] G. Mishra, B. Dash, S. Pandey, Layered double hydroxides: A brief review from fundamentals to application as evolving biomaterials, Applied clay science, 153 (2018) 172-186.

[2] I. García-Lodeiro, A. Fernández-Jiménez, A. Palomo, D.E. Macphee, Effect of calcium additions on N–A–S–H cementitious gels, Journal of the American Ceramic Society, 93 (2010) 1934-1940.

[3] Z. Xu, H. Zeng, Abrupt structural transformation in hydrotalcite-like compounds $Mg_{1-x}Al_x(OH)_2(NO_3)_x \cdot nH_2O$ as a continuous function of nitrate anions, The Journal of Physical Chemistry B, 105 (2001) 1743-1749.

[4] P. Koilraj, Y. Kamura, K. Sasaki, Synergetic co-immobilization of SeO_4^{2-} and Sr^{2+} from aqueous solution onto multifunctional graphene oxide and carbon-dot based layered double hydroxide nanocomposites and their mechanistic investigation, Journal of Materials Chemistry A, 6 (2018) 10008-10018.

[5] Y. Fujikawa, M. Fukui, Radionuclide sorption to rocks and minerals: effects of pH and inorganic anions. Part 1. Sorption of cesium, cobalt, strontium and manganese, Radiochimica Acta, 76 (1997) 153-162.

[6] Y. Fujikawa, M. Fukui, Radionuclide sorption to rocks and minerals: effects of pH and inorganic anions. Part 2. Sorption and speciation of selenium, Radiochimica Acta, 76 (1997) 163-174.

[7] M. Dammak, T. Mhiri, J. Jaud, J.M. Savariault, Structural study of the two new caesium sulfate and selenate tellurate $Cs_2SO_4 \cdot Te(OH)_6$ and $Cs_2SeO_4 \cdot Te(OH)_6$, International Journal of Inorganic Materials, 3 (2001) 861-873.

[8] D. Foose, G. Mitra, The crystal structure of cesium hydrogen selenate $CsHSeO_4$, Journal of Inorganic and Nuclear Chemistry, 39 (1977) 553-554.

[9] A.M. El-Kamash, Evaluation of zeolite A for the sorptive removal of Cs^+ and Sr^{2+} ions from aqueous solutions using batch and fixed bed column operations, Journal of Hazardous materials, 151 (2008) 432-445.

[10] D. Reichenberg, Properties of ion-exchange resins in relation to their structure. III. Kinetics of exchange, Journal of the American Chemical Society, 75 (1953) 589-597.

[11] P. Misaelides, S. Sarri, N. Kantiranis, F. Noli, A. Filippidis, B. de Blochouse, A. Maes, E. Breynaert, Investigation of chabazitic materials as Cs-137 sorbents from cementitious aqueous solutions, Microporous and Mesoporous Materials, 266 (2018) 183-188.

[12] S. Miyata, Anion-exchange properties of hydrotalcite-like compounds, Clays and Clay Minerals, 31 (1983) 305-311.

[13] L.V. Constantino, J.N. Quirino, A.M. Monteiro, T. Abrão, P.S. Parreira, A. Urbano, M.J. Santos, Sorption-desorption of selenite and selenate on Mg-Al layered double hydroxide in competition with nitrate, sulfate and phosphate, Chemosphere, 181 (2017) 627-634.

[14] W. Lee, J. Van Deventer, Use of infrared spectroscopy to study geopolymerization of heterogeneous amorphous aluminosilicates, Langmuir, 19 (2003) 8726-8734.

[15] T. Kameda, E. Kondo, T. Yoshioka, Equilibrium and kinetic studies of Se (vi) removal by Mg–Al layered double hydroxide doped with Fe^{2+}, RSC Advances, 4 (2014) 61817-61822.

Chapter 6

Mechanism of selenium (VI) immobilization using alkaline-earth metal oxides and ferrous salt

6.1 Introduction

Various treatment technologies such as adsorption, coagulation, ion-exchange, biological and chemical reduction, etc. have been proposed for the remediation of Se-contaminated water or soil [1]. Among them, the chemical reduction of SeO_4^{2-} to less soluble species has been deemed as a useful step to stabilize SeO_4^{2-} in soil or cement blocks especially for the treatment of ^{79}Se-contaminated radioactive wastes [2]. Iron-based materials including zero-valent iron (ZVI) or ferrous salts are environmentally friendly and inexpensive reagents for the reduction of selenium, and they have been extensively studied and widely used for in-situ and ex-situ environmental remediations [3, 4]. However, the ferric coating on the surface of ZVI is always the biggest obstacle for its long-time application [5, 6]. For ferrous salts such as ferrous sulfate or ferrous chloride, they have been commonly used in wastewater treatment [7]. Furthermore, Fe^{2+} simultaneously possesses reducibility and oxidability, and Fe(II)-adsorbed montmorillonite or calcite, green rust, pyrite, etc. have been tested for the reduction of selenium oxyanions [8-12]. On the other hand, alkaline-earth metal oxides including MgO and CaO are common cementitious materials. They have been widely adopted as adsorbent, pH regulator, etc. in wastewater treatment, waste-gas cleaning, solid waste disposal, and soil remediation [13-17].

The combination of alkaline-earth metal oxides (MgO and CaO) and ferrous salt could be the new possible stabilizers or the new additive into geopolymer blocks. Therefore, in the present study, the immobilization of SeO_4^{2-} was conducted outside the geopolymer blocks, in order to examine the efficiencies of alkaline-earth metal oxides and ferrous salt. The phase transformation in the process is still unclear and the comparison between MgO and CaO based reactions has not been reported. Thus, in

order to get a better understanding of the reactions, the present research explored the reduction capacity of Fe(II) salts mixed with MgO or CaO toward SeO_4^{2-} under anaerobic condition, and the specific immobilization mechanisms were explored by using X-ray absorption fine structure (XAFS), X-ray diffraction (XRD), Thermogravimetric analysis (TGA), X-ray photoelectron spectroscopy (XPS) and geochemical modeling.

6.2 Experimental

6.2.1 Materials and methods

The CaO was purchased in a purity of 99.9% (Wako), and MgO was a light-burned MgO with a purity of 96% (Wako). The ferrous sulfate heptahydrate ($FeSO_4 \cdot 7H_2O$, 99%, Wako) was adopted as the reducing reagent in the study. The simulated SeO_4^{2-} pollutant used in the study is sodium selenate (Na_2SeO_4, 97%, Wako). The deoxygenated water was prepared by simultaneously boiling and nitrogen bubbling the deionized water. The specific experimental conditions are named and designed as shown in **Table 6.1**. Noticeably, the concentration of Se based on the solid composition is approximately 8% (weight percent), according to the previous study [18]. Thereafter, the deoxygenated water was added to each tube at a water/solid mass ratio of 3 under the nitrogen protection to avoid oxygen and carbonate contaminations. After curing for 7 days, all of the samples were dried in a freeze dryer (FDU-1200) for 24 h without exposure to air. Lastly, the powder samples were obtained and used for the following characterizations and leaching tests.

As for the leaching test, three extractants including deionized water, acetic acid solution (pH 4.93), and nitric acid solution (pH 1) were used, and the liquid/solid ratio

was fixed to 20:1 (L: kg). After shaking at 30 rpm for 18 h, aliquots of supernatants were taken with the help of 0.2 μm filters and stored for concentration determination.

Table 6.1 The experimental condition. (unit, g; -, none; FSH, ferrous sulfate heptahydrate; SS, sodium selenate).

Sample	MgO	CaO	FSH	SS
M1	2	-	-	-
M2	2	-	-	0.5
M3	2	-	2	0.5
C1	-	2	-	-
C2	-	2	-	0.5
C3	-	2	2	0.5
MC1	1	1	-	0.5
MC2	1	1	2	0.5

6.2.2 Characterizations

The concentrations of selenium in solutions were determined using an inductively coupled plasma optical emission spectrometry (ICP-OES, Perkin Elmer, Optima 8300, US). The powder X-ray diffractions were collected on a Rigaku Ultima IV XRD (Akishima, Japan): Cu Kα (40 kV, 40 mA) with a Ni filter at a scanning speed of 2° min^{-1} and scanning step of 0.02°. In addition, Thermogravimetric analysis (TG, 2000 SA thermal balance, Bruker, Germany) was used to determine the weight loss of these samples. The heating rate and nitrogen flows were 10 °C/min and 100 $mL \cdot min^{-1}$, respectively. X-ray photoelectron spectroscopy (XPS) was adopted to determine the chemical states of Fe in solid residues, conducted on an ESCA 5800 (ULVAC-PHI, Inc., Kanagawa, Japan) using a monochromated Al Kα X-ray source. The binding energy of C1s = 284.6 eV for adventitious carbon was used to calibrate the binding energies. In addition, the experimental conditions of M3 and C3 were simulated using PHREEQC in order to evaluate the phase transformations during the reaction.

X-ray absorption fine structure (XAFS) spectra of the Se-K edge of solid residues were collected on a beamline-06 in the SAGA Light Source (Saga, Japan). The energy range of the light source is 2.1–23 keV, and the typical photon flux is 10^{10} photons/s. The electron storage ring operated at an energy of 1.4 GeV, and a silicon (111) double-crystal monochromator was used to obtain the incident X-ray beam. The Se-K edge was collected in the transmission mode and fluorescence mode (for the sample with low Se conc.). Each sample was measured in three loops to increase the data quality. Meanwhile, XAFS spectra of known reference materials including Na_2SeO_3 and Na_2SeO_4 were also measured on the beamline. Data processing was carried out on the ATHENA and ARTEMIS [19-23].

6.3 Results and discussion

6.3.1 Characterizations of solid residues

6.3.1.1 Phase analysis

Fig. 6.1a presents the XRD patterns of solid residues. It can be found that all of MgO or CaO has been hydroxylated into the corresponding hydroxides after 7 d curing. For M1, the XRD pattern showed the characteristic peaks including 001, 101, 102 and 110, etc. of $Mg(OH)_2$. The extra peaks at approximately 18, 22, 27, 28, etc. of 2θ belonging to Na_2SeO_4, appeared in the XRD pattern of M2. This indicated that the simulated pollutant of Na_2SeO_4 just went through dissolution and then crystallization in the reaction and drying processes, respectively. However, these peaks belonging to Na_2SeO_4 disappeared in M3 where Fe(II) existed, which could imply that SeO_4^{2-} was reacted with Mg and/or Fe.

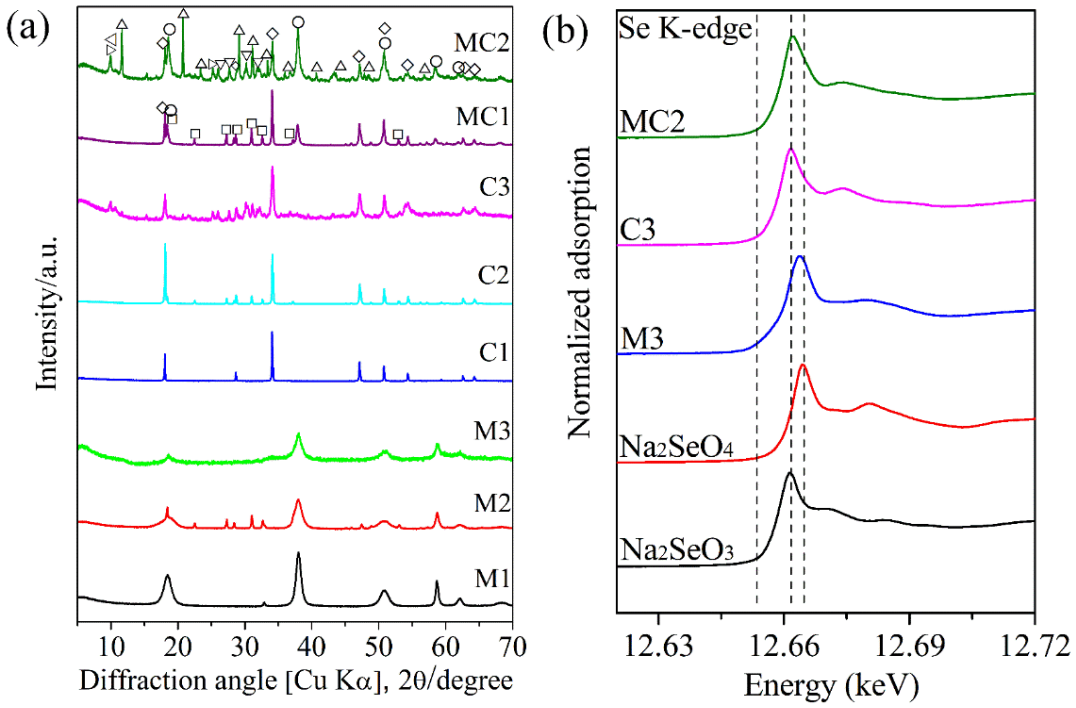

Fig. 6.1 (a) XRD patterns of solid residues collected from each experiment. Symbols: ○, Brucite ($Mg(OH)_2$); ◇, Porlandite ($Ca(OH)_2$); △, Gypsum ($CaSO_4 \cdot 4H_2O$); □, Sodium selenate (Na_2SeO_4); ▷, Ferricopiapite ($Fe_{4.67}(SO_4)_6(OH)_2 \cdot 20H_2O$); ◁, Paracoquimbite ($Fe_2(SO_4)_3(H_2O)_9$); ▽, Hematite ($Fe_2O_3$); (b) XANES spectra of solid residues from M3, C3, MC2, and the related standards.

Furthermore, the increased background noise might indicate that some amorphous minerals were formed. After removing the background, it can be clearly seen that there is a peak at 10°/2θ which could belong to the 003 peak of layered double hydroxide (LDH) structure (**Fig. 6.2**) [24, 25]. As for C1 and C2, they went through similar processes with M1 and M2, except that CaO was added in C1 and C2 instead of MgO. However, the XRD pattern of C3 showed more complex peaks than that of C1 and C2. It could be obviously found that Fe-related minerals including ferricopiapite ($Fe_{4.67}(SO_4)_6(OH)_2 \cdot 20H_2O$), paracoquimbite ($Fe_2(SO_4)_3(H_2O)_9$) and hematite ($Fe_2O_3$) were formed in the reaction system of CaO and $FeSO_4$. Similarly, these newly formed minerals occurred in the reaction of MC2 as well, which indicated that CaO controlled the whole reaction rather than MgO.

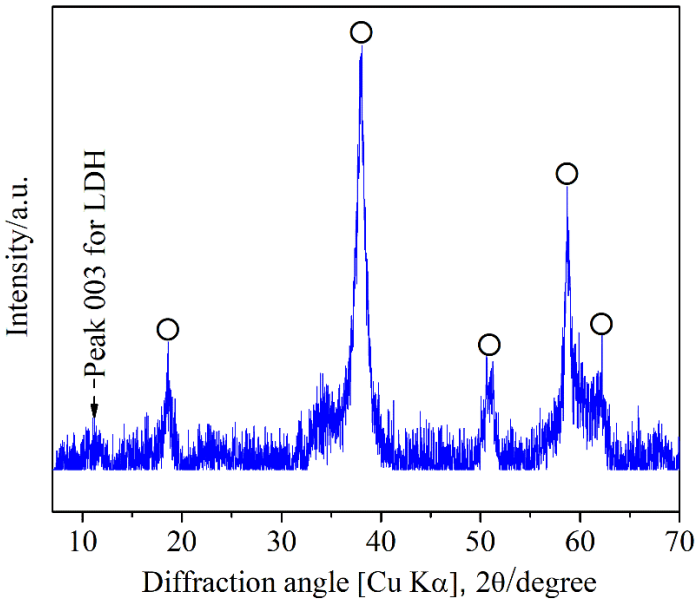

Fig. 6.2 XRD pattern of M3 sample (after removing background). Symbols: ○, Brucite ($Mg(OH)_2$).

6.3.1.2 XANES analysis

The reduction of SeO_4^{2-} to SeO_3^{2-} could be an important step in the immobilization process. The X-ray absorption near edge structure (XANES) spectra of M3, C3, MC2, and related standards are shown in **Fig. 6.2b**. Less SeO_4^{2-} were reduced to SeO_3^{2-} in the case of MgO and $FeSO_4$ (M3) because the XANES edge was closed to the edge of Na_2SeO_4. By contrast, almost all of SeO_4^{2-} had been reduced to SeO_3^{2-} by ferrous salt in the presence of CaO since the edge nearly coincided with that of Na_2SeO_3 (C3). The quantifications of SeO_3^{2-} and SeO_4^{2-} in M3 and MC2 samples were determined using linear combination fitting. It showed that 45.50% of SeO_4^{2-} had been reduced to SeO_3^{2-} in M3 and 86.70% for MC2. The reduction process of SeO_4^{2-} to SeO_3^{2-} could control the Se leaching behavior. Therefore, there would be two aspects that need to be clearly discussed: (1) the chemical associations of selenium in the M3, C3, and MC2 samples; (2) the mechanisms of how MgO and CaO affect the whole reactions.

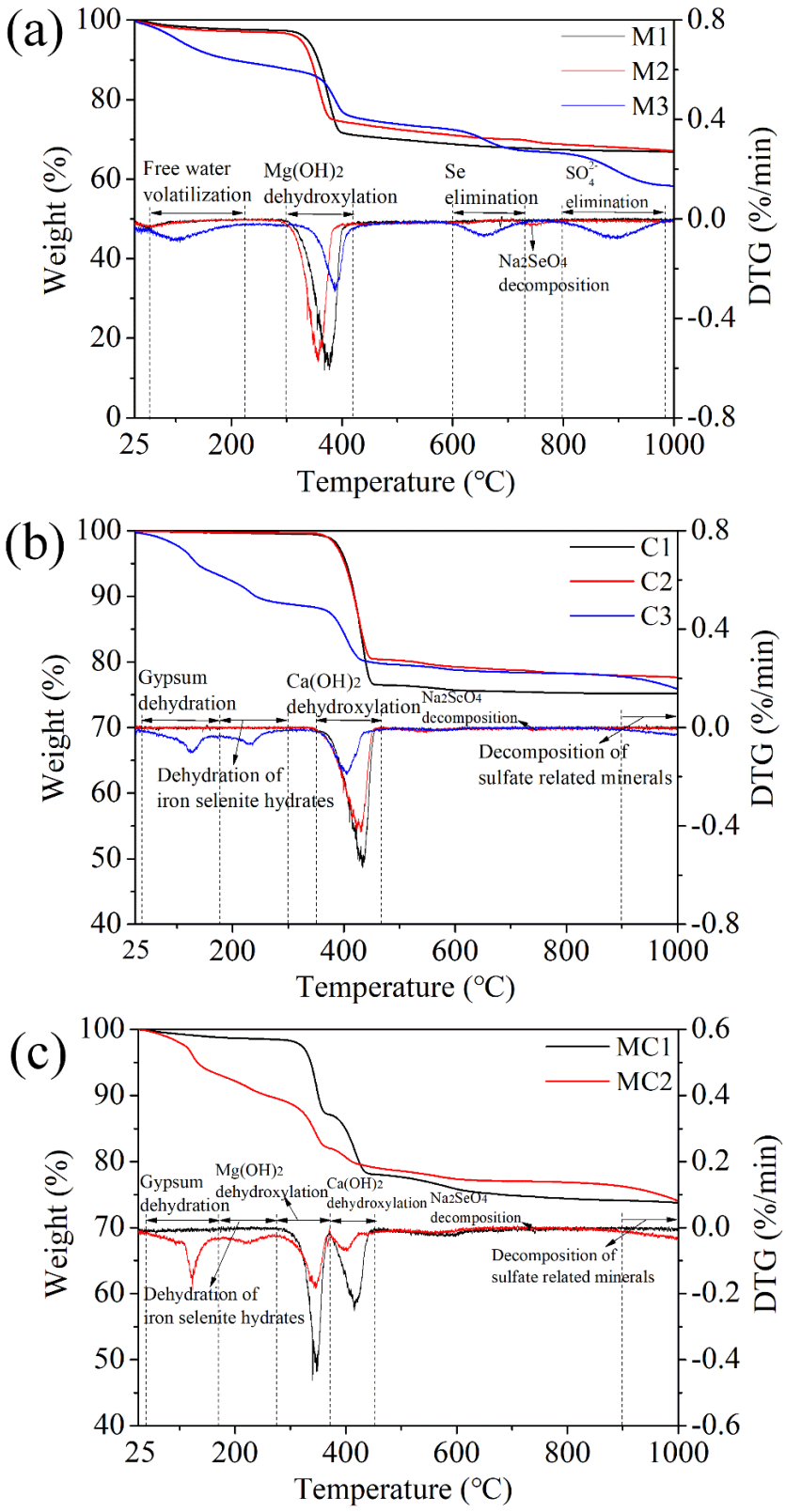

Fig. 6.3 TG results of solid residues from each experiment condition: (a), M1, M2 and M3; (b), C1, C2 and C3; (C), MC1 and MC2.

6.3.1.3 TG analysis

Thermogravimetric analysis (TGA) was adopted to get a further understanding of the solid residues, and the results were presented in **Fig. 6.3**. There are several stages concerning the heating temperature for each solid residue. For MgO-based reactions (M1-M3, **Fig. 6.3a**), a large weight loss at approximately 300–420 ℃ occurred to all of them because of the dehydroxylation of $Mg(OH)_2$. The small weight loss in the M2 curve at 710–800 ℃ is thought to be induced by the Na_2SeO_4 decomposition [26]. However, this small peak disappeared in the DTG curve of M3, indicating different associations of Se with that in M2. The eliminations of selenite or selenate, and sulfate can be identified for the M3 sample at 600–720 and 800–1000 ℃, respectively [27]. It seems similar to the decomposition process of selenium in LDH or MgO after selenium sorption (**Fig. 6.4**), and this might indicate the similar associations of selenium in M3 with that in LDH or MgO after selenium sorption.

On the other hand, for CaO-based reactions (C1-C3, **Fig. 6.3b**), the weight loss at approximately 350–470 ℃ can be mainly assigned to the dehydroxylation of $Ca(OH)_2$. The weight loss of the gypsum dehydration could be identified at the temperature lower than 200 ℃, which is overlapped with the volatilization of free water. A weight loss at the temperature of approximately 180–300 ℃ could be attributed to the dehydration of iron selenite hydrates [28, 29]. There was a weight loss starting at 900 ℃ to a higher temperature, which represented the decompositions of sulfate related minerals including ferricopiapite and paracoquimbite. Actually, the changes in weight loss for MC1 and MC2 (**Fig. 6.3c**) showed similar trends with the cases of C1-C3, and this was mainly because CaO controlled the reactions in MC1 and MC2 rather than MgO, as mentioned earlier. In addition, there was no weight loss

corresponding to the decomposition of Se in C3 or MC2. This indicated that the selenium in C3 or MC2 might be bonded with iron. Then, a higher temperature is needed for decomposition, which might be overlapped with the decomposition process of sulfate related minerals.

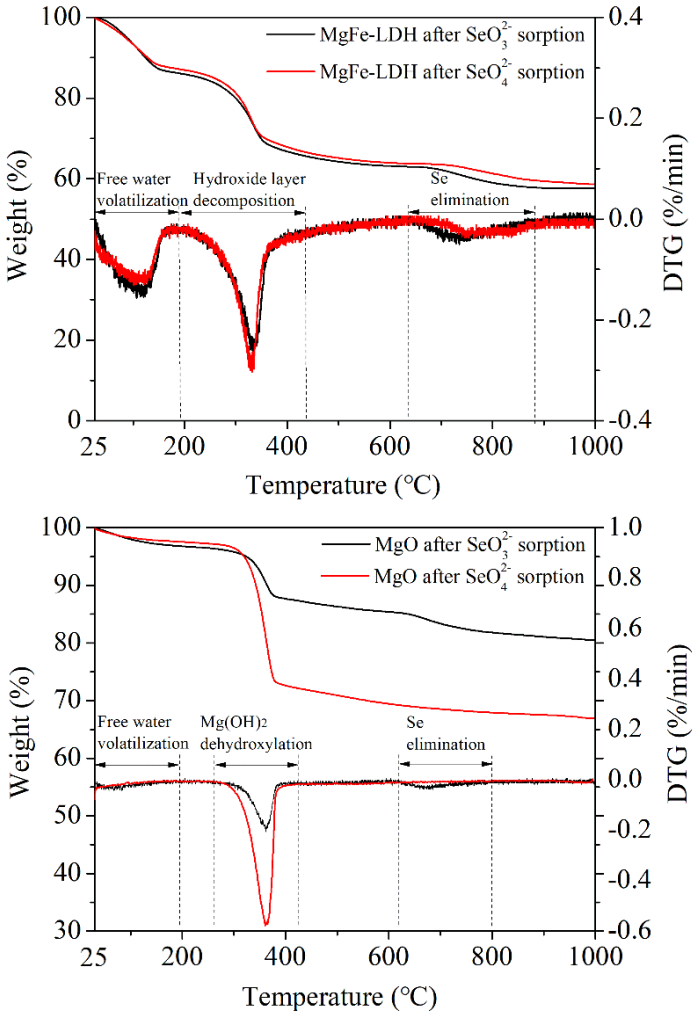

Fig. 6.4 TG results of different kinds of adsorbent after selenium sorption.

6.3.2 Leaching results

Three kinds of extractants were used in the leaching tests of these solid residues. The final pH of each leaching test is shown in **Fig. 6.5 (a)**. A similar pH occurred to the leachates of deionized water and acetic acid, and the pH of leachates using nitric

acid as the extractant was slightly lower. This illustrated that MgO and CaO had enough buffering capacities to resist acidic solutions. In addition, it could be found that the pH of leachate for M3 was always lower than that from M1 or M2, and this might be because iron ion belonged to the category of Lewis acid which can contribute to the consumption of OH^- in the solution. **Fig. 6.5 (b)** presents the leaching results of M3, C3, and MC2 using three extractants. For M2, C2, and MC1, most of the added SeO_4^{2-} was leached out because SeO_4^{2-} cannot strongly interact with MgO or CaO. However, in the presence of Fe(II), the leaching fractions greatly decreased to approximately 40% for M3, 4% for C3, and 15% for MC2. The leaching fraction for the case of CaO and Fe(II) was much lower than that of MgO and Fe(II). Furthermore, the leaching fractions for each experiment did not change with regard to different extractants. This indicated that the immobilization parts of selenium were very stable in the matrixes. Therefore, for MgO or CaO, they can be good matrixes for the immobilization of SeO_4^{2-} in the presence of Fe(II). Importantly, under the same experimental condition, different immobilization efficiencies for MgO and CaO were obtained, which also implied that the mechanisms behind them were incongruous.

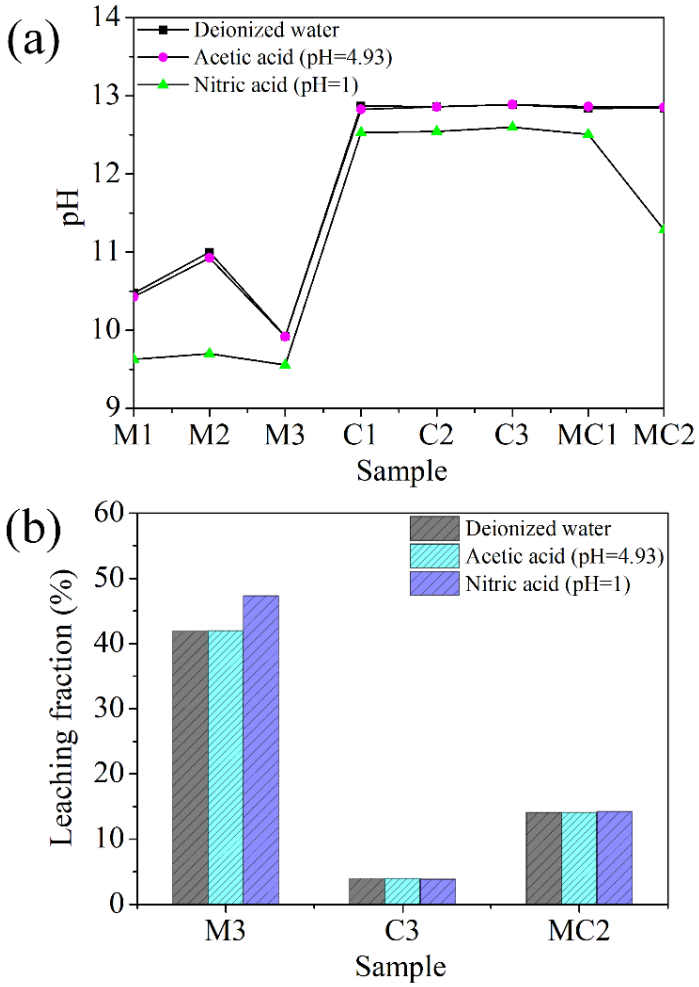

Fig. 6.5 leaching solution pH (a) and Se leaching fractions (b) from each sample using different extractants, the error for leaching fraction is within 5%.

6.3.3 Immobilization mechanisms

From the above characterizations, it has been found that different immobilization mechanisms occurred in terms of MgO and CaO in the presence of Fe(II), respectively. A clear distinction between them is the amount of SeO_4^{2-} which has been reduced to SeO_3^{2-}. In the case of CaO-Fe(II)-based reaction, almost all of SeO_4^{2-} was reduced to SeO_3^{2-}, and then a low leaching amount was obtained. However, only approximately 43% of SeO_4^{2-} was reduced to SeO_3^{2-} as referring to MgO-Fe(II)-based reaction. This reduction process plays a decisive role in the immobilization of SeO_4^{2-}, as indicated by

leaching results. The reduction of SeO_4^{2-} by Fe(II) could be expressed as equation (1) and (2) [30, 31].

$$Fe(OH)_2 + H_2O \rightarrow Fe(OH)_3 + H^+ + e^- \quad (6.1)$$

$$SeO_4^{2-} + 2H^+ + 2e^- \rightarrow SeO_3^{2-} + H_2O \quad (6.2)$$

Different reduction abilities shown by Fe(II) in these two matrixes could be explained by the following reasons. Firstly, MgO and CaO can produce the reaction environments with the pH of 10–11 and 12–13, respectively [14, 32, 33]. Generally, the redox potential (Eh) of SeO_4^{2-}/ SeO_3^{2-} pair decreases as the pH value increases [34]. Thus, the E_H [SeO_4^{2-}/ SeO_3^{2-}] in the MgO-based reaction should be higher than that in the CaO-based reaction, which indicates that SeO_4^{2-} would be easier to be reduced to SeO_3^{2-} in the CaO-based reaction under the same reducing environment. On the other hand, the oxidation rate of $Fe(OH)_2$ to $Fe(OH)_3$ is independent of pH (> 8) [35]. Therefore, for both MgO- and CaO-based reactions, the electron transfer rate should be the same assuming that other conditions are consistent. However, there is a large difference in the reduction ratios of SeO_4^{2-} under the same curing time. The interactions between Fe(II) and MgO or CaO might affect the reduction process. Both MgO and CaO do not only provide the alkaline condition, but also their hydration products, which might participate through phase transformations, as indicated by XRD, TG results.

Under CaO-based condition, almost all of SeO_4^{2-} has been reduced to SeO_3^{2-}, and the association of Se should be explored. XPS results (**Fig. 6.6a** and **6.6b**) indicated that Fe(II) in both C3 and MC2 samples had been oxidized into Fe(III). The PHREEQC calculation predicted that the possible precipitates were formed in the C3 sample as shown in **Fig. 6.7a**. The saturation indexes of Fe_2O_3, FeOOH, $Ca(OH)_2$, and

$CaSO_4 \cdot 2H_2O$ have the positive values, which means that these phases are the most likely to be formed in the case of CaO-based reaction (C3). This is consistent with the XRD analysis except that FeOOH is undetected in the XRD pattern, and this might be because of its amorphous properties [36]. Noticeably, the formation of $CaSeO_3$ seems to be less possibility to be formed because of the negative value of the saturation index. In addition, the negative values of saturation indexes of $Fe_2(OH)_4SeO_3$ and $Fe_2(SeO_3)_3 \cdot 2H_2O$ indicates that the direct formation of ferric selenite should be impossible in this reaction. Therefore, iron-based minerals (Fe_2O_3 and FeOOH) can be the best possibility to capture the SeO_3^{2-} through complexations.

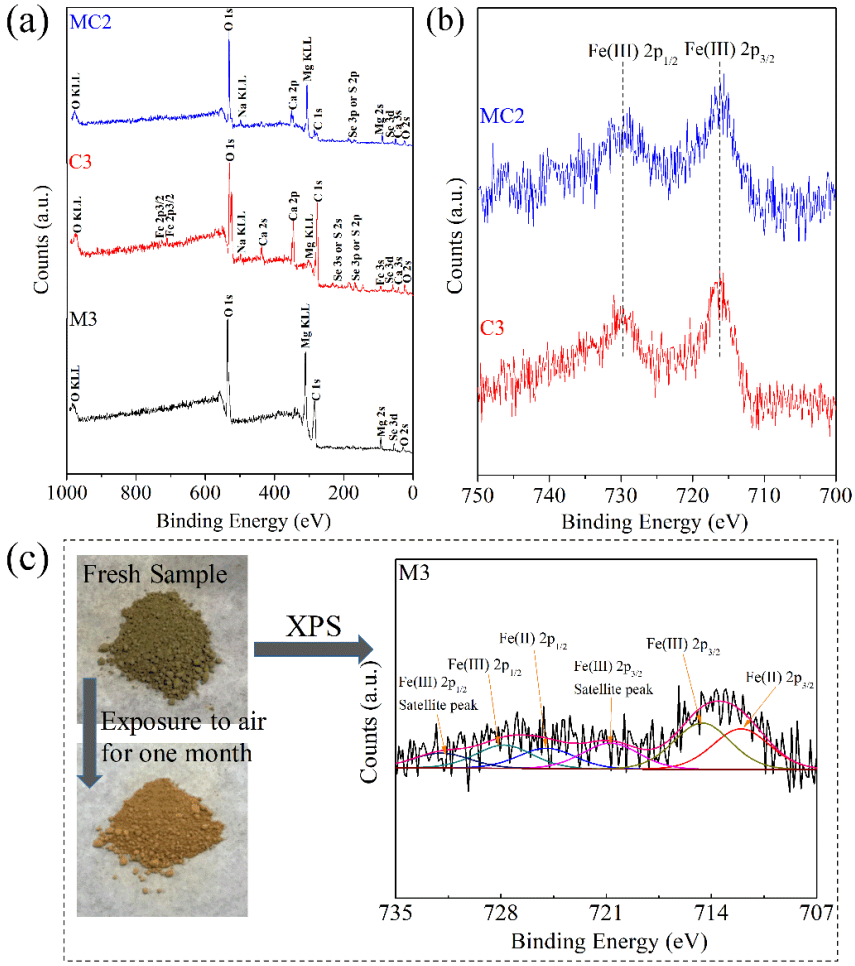

Fig. 6.6 (a) XPS wide scans of E3, E6 and E8; (b) Fe 2p peaks of E6 and E8; (c) Fe 2p peak separation of E3, and the pictures of fresh sample and sample after exposure to air.

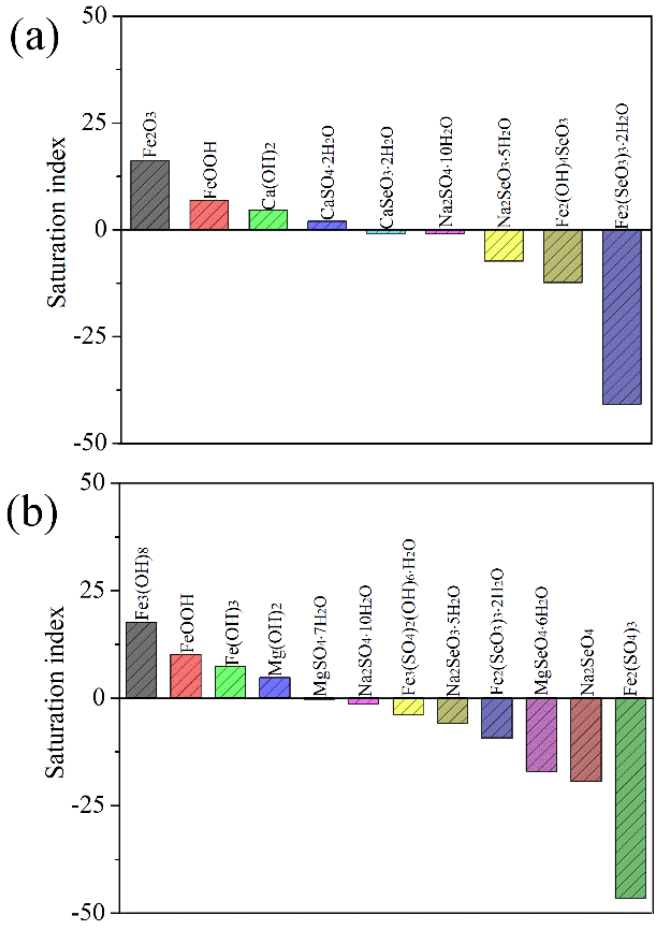

Fig. 6.7 The simulated mineralogical transformations for (a) C3 and (b) M3 experimental conditions at equilibrium state.

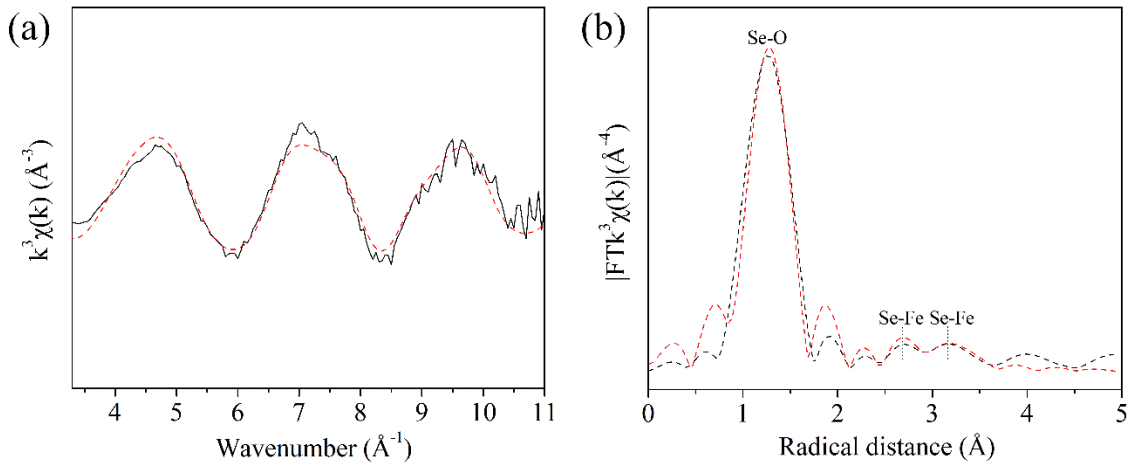

Fig. 6.8 (a) Corresponding k^3-weighted Se K-edge EXAFS data. (b) Se K-edge EXAFS data of Fourier transforms (not corrected for phase shift) showing both raw (solid lines) and fitted data (dash lines) of C3.

Table 6.2 Se K-edge EXAFS fitting results of C3. Coordination number (CN), interatomic distance (R), Debye-Waller factor (σ^2), and residual factor (R_f).

Sample	Shell	CN	R(Å)	σ^2(Å)	ΔE_0(eV)	R_f(%)
C3	Se-O	2.96	1.69	0.002	5.71	1.6
	Se-Fe	0.99	2.84	0.016		
		0.99	3.60	0.006		

In order to further confirm the associations of Se atoms in the CaO-based matrix, an extended X-ray absorption fine structure (EXAFS) spectrum of C3 was collected, and the k^3-weighted spectra and the radial structure functions around selenium atom from the Fourier transforms of the EXAFS data were shown in **Fig. 6.8**. Three shells of backscattering could be identified at radical distances of 1.3, 2.7 and 3.2 Å in the Fourier transform spectrum (FTs) (**Fig. 6.8b**). These contributions are simulated satisfactorily with an O shell at 1.69 Å containing 2.96 atoms, a Fe shell at 2.84 Å containing 0.99 atoms, and another Fe shell at 3.60 Å containing 0.99 atoms (**Table 6.2**). The first shell could be attributed to the three oxygen atoms in SeO_3^{2-}, which is consistent with the previous studies [37-39]. Theoretically, the shorter atomic distance of Se-Fe with 2.84 Å should be caused by a bidentate mononuclear edge-sharing (^{1}E) linkage between SeO_3^{2-} and FeO_6 octahedron, and the longer distance of Se-Fe with 3.6 Å should be in line with a monodentate mononuclear corner-sharing (^{1}V) linkage between one SeO_3^{2-} and FeO_6 octahedron [40]. The fitting results are relatively consistent with the previous studies [40-43]. Thus, according to the combined analysis of geochemical modeling and EXAFS analysis, it can be concluded that the generated SeO_3^{2-} was mainly adsorbed onto the iron-based minerals (Fe_2O_3 and FeOOH) through the formation of both bidentate mononuclear edge-sharing (^{1}E) and monodentate mononuclear corner-sharing (^{1}V) inner sphere surface complexes.

Compared to CaO-based condition, the MgO-based reaction seems to be more complex. The geochemical modeling results for the M3 sample are shown in **Fig. 6.7b**.

It can be known that $Fe_3(OH)_8$, FeOOH, $Fe(OH)_3$ and $Mg(OH)_2$ could be possibly formed in the MgO-based reaction because of the positive values of their saturation indexes. Among them, $Fe_3(OH)_8$ is the most likely to be formed due to the highest saturation index. The phase of $Fe_3(OH)_8$ has been claimed to be a Fe(II)-Fe(III) hydroxide-(sulfate) (green rust) which is a kind of LDH [44]. In addition, it could be obviously found that the fresh sample of M3 had an appearance of light green color, and the color changed to yellow after exposure to air for one month (**Fig. 6.6c**). This indicated the presence of Fe(II) in the fresh sample of M3. Thus, the reduction process of SeO_4^{2-} to SeO_3^{2-} could continue to occur until that almost of SeO_4^{2-} is reduced to SeO_3^{2-} if the reaction has not been stopped in 7 days. XPS result showed that the molar ratio of Fe(II)/Fe(III) in M3 was 0.88, which was far lower than the empirical values of green rust samples reported in references [45, 46]. Thus, a part of Fe(III) might exist in other phases such as FeOOH and $Fe(OH)_3$, as the PHREEQC simulation result indicated.

On the other hand, TG results (**Fig. 6.3a**) showed that the weight loss of selenium for M3 was 4.14% (620–700 ℃). After converting it to mmol/g (based on the weight of $Mg(OH)_2$), the volatile amount of selenium was 2.53 mmol/g which was extremely closed to the adding amount (2.57 mmol/g). This can suggest that there was no selenium (SeO_3^{2-} or SeO_4^{2-}) associated with Mg or Fe to form crystals because the decomposition temperature of selenite and selenate minerals would be generally higher than 700 ℃ [27, 47]. In order to confirm it, **Fig. 6.9** shows the k^2-weighted spectra and the radial structure functions around the selenium atom from the Fourier transforms of the EXAFS data. It can be found that the EXAFS spectrum of the M3 sample was similar to that of MgO after SeO_3^{2-} and SeO_4^{2-} sorption, and all of them did

not show any evidence of direct chemical bonding between the selenium oxyanions and magnesium or iron. Thus, the EXAFS results confirmed that SeO_4^{2-} or SeO_3^{2-}could only be adsorbed on the surface of some minerals mainly through outer-sphere complexation.

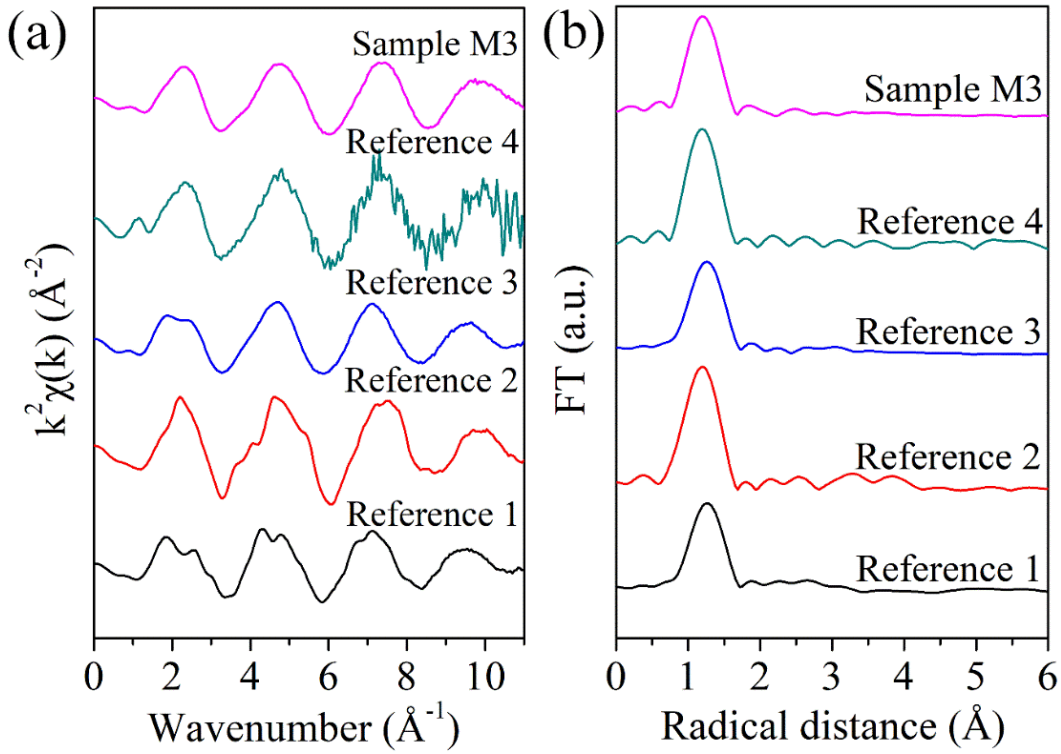

Fig. 6.9 X-ray absorption spectra of M3 and reference materials: Se K-edge EXAFS spectra in k space (a) and R space (b). Reference 1, 2, 3 and 4 are Na_2SeO_3, Na_2SeO_4, MgO after SeO_3^{2-} sorption, MgO after SeO_4^{2-} sorption, respectively.

The geochemical modeling result has suggested the formation of green rust, and this can be consistent with the XRD pattern (**Fig. 6.2**) which already indicates the existence of LDH in the solid residue of M3 because green rust is a kind of layered double hydroxide which can incorporate anionic species in the interlayer space [46]. SeO_3^{2-} is the most possible ion which can be incorporated into the LDH interlayer because a reactivity order of the involved anionic species could be as following: SO_4^{2-} $\approx$ SeO_4^{2-} < SeO_3^{2-} [48]. However, it should be noticed that the concentration of SO_4^{2-} is almost two times higher than SeO_3^{2-} or SeO_4^{2-}, which definitely leads to the intense

competition with SeO_3^{2-} or SeO_4^{2-} for the positively-charged sites on the external and internal surfaces of the LDH [49]. In addition, compared to the amount of $Mg(OH)_2$, the content of the formed LDH could be very low. Furthermore, the reaction occurred in a system with a small liquid/solid ratio (3:1), so there should be large differences in terms of anion transportation and incorporation compared to that in the solution. Thus, most of the selenium (SeO_3^{2-} and SeO_4^{2-}) was preferentially distributed onto the $Mg(OH)_2$ through outer-sphere adsorption, according to the above analysis and previous studies [50, 51]. In addition, the leaching results showed that the leaching amount of Se was consistent with the reduced amount of SeO_4^{2-}, indicating that SeO_4^{2-} cannot be effectively immobilized in MgO-based reaction and the further reaction between SeO_3^{2-} and Fe or Mg could occur during the leaching process.

6.4 Conclusions

The mixtures of metal oxide (CaO or MgO) and ferrous salt were used for the immobilization of SeO_4^{2-}, respectively. For CaO-based reaction, almost all of SeO_4^{2-} was reduced to SeO_3^{2-} within 7 days. EXAFS results indicated that the generated SeO_3^{2-} was mainly adsorbed onto the iron-based minerals (Fe_2O_3 and FeOOH) through the formation of both bidentate mononuclear edge-sharing (^1E) and monodentate mononuclear corner-sharing (^1V) inner-sphere surface complexes. Thus, a low leaching amount of Se (approximately 5%) was obtained for CaO-based reaction. However, only 45.50% of SeO_4^{2-} was reduced to SeO_3^{2-} in 7 days, and more than 40% of Se was leached out for MgO-based reaction. But the existence of Fe(II) can also indicate that the reaction system of MgO and ferrous salt can last for a longer time (more than 7 days), which definitely benefits for long-term pollution treatment such as

soil remediation, and kinetic study should be explored in the future. In terms of the Se association in the M3 sample, most of the selenium (SeO_3^{2-} and SeO_4^{2-}) was preferentially distributed onto the $Mg(OH)_2$ through outer-sphere adsorption.

References

[1] L. Xu, Y. Huang, A novel layered double hydroxide coupled with zero valent iron system for selenate removal under anaerobic condition: Batch and continuous studies, Chemical Engineering Journal, 359 (2019) 1166-1174.

[2] T. Suzuki, K. Sue, H. Morotomi, M. Niinae, M. Yokoshima, H. Nakata, Immobilization of selenium (VI) in artificially contaminated kaolinite using ferrous ion salt and magnesium oxide, Journal of Environmental Chemical Engineering, 7 (2019) 102802.

[3] M. Qiu, M. Wang, Q. Zhao, B. Hu, Y. Zhu, XANES and EXAFS investigation of uranium incorporation on nZVI in the presence of phosphate, Chemosphere, 201 (2018) 764-771.

[4] C. Tang, Y. Huang, Z. Zhang, J. Chen, H. Zeng, Y.H. Huang, Rapid removal of selenate in a zero-valent iron/Fe_3O_4/Fe^{2+} synergetic system, Applied Catalysis B: Environmental, 184 (2016) 320-327.

[5] F. Obiri-Nyarko, S.J. Grajales-Mesa, G. Malina, An overview of permeable reactive barriers for in situ sustainable groundwater remediation, Chemosphere, 111 (2014) 243-259.

[6] C. Tang, Y.H. Huang, H. Zeng, Z. Zhang, Reductive removal of selenate by zero-valent iron: The roles of aqueous Fe^{2+} and corrosion products, and selenate removal mechanisms, Water Research, 67 (2014) 166-174.

[7] A.S. Adeleye, J.R. Conway, K. Garner, Y. Huang, Y. Su, A.A. Keller, Engineered nanomaterials for water treatment and remediation: Costs, benefits, and applicability, Chemical Engineering Journal, 286 (2016) 640-662.

[8] S. Chakraborty, F. Bardelli, L. Charlet, Reactivities of Fe (II) on calcite: selenium reduction, Environmental Science & Technology, 44 (2010) 1288-1294.

[9] S. Myneni, T.K. Tokunaga, G. Brown, Abiotic selenium redox transformations in the presence of Fe (II, III) oxides, Science, 278 (1997) 1106-1109.

[10] A.C. Scheinost, L. Charlet, Selenite reduction by mackinawite, magnetite and siderite: XAS characterization of nanosized redox products, Environmental Science & Technology, 42 (2008) 1984-1989.

[11] A.G. Ilgen, J.N. Kruichak, K. Artyushkova, M.G. Newville, C. Sun, Redox transformations of As and Se at the surfaces of natural and synthetic ferric

nontronites: role of structural and adsorbed Fe (II), Environmental Science & Technology, 51 (2017) 11105-11114.

[12] N. Börsig, A.C. Scheinost, S. Shaw, D. Schild, T. Neumann, Retention and multiphase transformation of selenium oxyanions during the formation of magnetite via iron (II) hydroxide and green rust, Dalton Transactions, 47 (2018) 11002-11015.

[13] R. Li, J.J. Wang, B. Zhou, Z. Zhang, S. Liu, S. Lei, R. Xiao, Simultaneous capture removal of phosphate, ammonium and organic substances by MgO impregnated biochar and its potential use in swine wastewater treatment, Journal of Cleaner Production, 147 (2017) 96-107.

[14] Q. Tian, B. Guo, S. Nakama, L. Zhang, Z. Hu, K. Sasaki, Reduction of undesirable element leaching from fly ash by adding hydroxylated calcined dolomite, Waste Management, 86 (2019) 23-35.

[15] X. Wang, W. Zeng, M. Song, F. Wang, X. Hu, Q. Guo, Y. Liu, Polyetheramine improves the CO^2 adsorption behavior of tetraethylenepentamine-functionalized sorbents, Chemical Engineering Journal, 364 (2019) 475-484.

[16] Z. Jin, Y. Jia, K.-S. Zhang, L.-T. Kong, B. Sun, W. Shen, F.-L. Meng, J.-H. Liu, Effective removal of fluoride by porous MgO nanoplates and its adsorption mechanism, Journal of Alloys and Compounds, 675 (2016) 292-300.

[17] L. Wang, L. Chen, D.-W. Cho, D.C. Tsang, J. Yang, D. Hou, K. Baek, H.W. Kua, C.-S. Poon, Novel synergy of Si-rich minerals and reactive MgO for stabilisation/solidification of contaminated sediment, Journal of Hazardous materials, 365 (2019) 695-706.

[18] W. Cui, P. Li, Z. Wang, S. Zheng, Y. Zhang, Adsorption study of selenium ions from aqueous solutions using MgO nanosheets synthesized by ultrasonic method, Journal of Hazardous materials, 341 (2018) 268-276.

[19] B. Ravel, M. Newville, ATHENA and ARTEMIS: interactive graphical data analysis using IFEFFIT, Physica Scripta, 2005 (2005) 1007.

[20] M. Newville, IFEFFIT: interactive XAFS analysis and FEFF fitting, Journal of synchrotron radiation, 8 (2001) 322-324.

[21] B. Ravel, M. Newville, ATHENA, ARTEMIS, HEPHAESTUS: data analysis for X-ray absorption spectroscopy using IFEFFIT, Journal of synchrotron radiation, 12 (2005) 537-541.

[22] A. Ankudinov, B. Ravel, J. Rehr, S. Conradson, Real-space multiple-scattering calculation and interpretation of x-ray-absorption near-edge structure, Physical Review B, 58 (1998) 7565.

[23] B. Guo, Y. Xiong, W. Chen, S.A. Saslow, N. Kozai, T. Ohnuki, I. Dabo, K. Sasaki, Spectroscopic and First-Principles Investigations of Iodine Species Incorporation into Ettringite: Implications for Iodine Migration in Cement Waste Forms, Journal of Hazardous materials, (2019) 121880.

[24] W. Cheng, T. Wan, X. Wang, W. Wu, B. Hu, Plasma-grafted polyamine/hydrotalcite as high efficient adsorbents for retention of uranium (VI) from aqueous solutions, Chemical Engineering Journal, 342 (2018) 103-111.

[25] Q. Tian, K. Sasaki, A novel composite of layered double hydroxide/geopolymer for co-immobilization of Cs^+ and SeO_4^{2-} from aqueous solution, Science of the Total Environment, 695 (2019) 133799.

[26] M. Trivedi, K. Sethi, P. Panda, S. Jana, Physicochemical, thermal and spectroscopic characterization of sodium selenate using XRD, PSD, DSC, TGA/DTG, UV-vis, and FT-IR, Marmara Pharmaceutical Journal, 21 (2016).

[27] M. Ebert, D. Havlíček, Magnesium selenites, Chem. zvestí, 34 (1980) 441-451.

[28] A. Holzheid, M.V. Charykova, V.G. Krivovichev, B. Ledwig, E.L. Fokina, K.L. Poroshina, N.V. Platonova, V.V. Gurzhiy, Thermal behavior of ferric selenite hydrates ($Fe_2(SeO_3)_3 \cdot 3H_2O$, $Fe_2(SeO_3)_3 \cdot 5H_2O$) and the water content in the natural ferric selenite mandarinoite, Chemie der Erde, 78 (2018) 228-240.

[29] G. Giester, F. Pertlik, Synthesis and crystal structure of iron (III) selenate (IV) trihydrate, $Fe_2(SeO_3)_3\ 3H_2O$, Journal of Alloys and Compounds, 210 (1994) 125-128.

[30] H.K. Shrimpton, D.W. Blowes, C.J. Ptacek, Fractionation of selenium during selenate reduction by granular zerovalent iron, Environmental Science & Technology, 49 (2015) 11688-11696.

[31] I.-H. Yoon, S. Bang, K.-W. Kim, M.G. Kim, S.Y. Park, W.-K. Choi, Selenate removal by zero-valent iron in oxic condition: the role of Fe(II) and selenate

removal mechanism, Environmental Science and Pollution Research, 23 (2016) 1081-1090.

[32] B. Guo, S. Nakama, Q. Tian, N.D. Pahlevi, Z. Hu, K. Sasaki, Suppression processes of anionic pollutants released from fly ash by various Ca additives, Journal of Hazardous materials, 371 (2019) 474-483.

[33] Y. Jia, B. Wang, Z. Wu, T. Zhang, Effect of CaO on the reaction process of MgO-SiO_2-H_2O cement pastes, Materials Letters, 192 (2017) 48-51.

[34] P. An, X. Langqiu, Redox potential E H [Se(VI)/Se(IV)] of aqueous extractof soils from Yongshou Kaschin-Beck diseaseregion and the influence by humic acid, Journal of Environmental Sciences, 1 (1989) 29-36.

[35] B. Morgan, O. Lahav, The effect of pH on the kinetics of spontaneous Fe(II) oxidation by O_2 in aqueous solution–basic principles and a simple heuristic description, Chemosphere, 68 (2007) 2080-2084.

[36] R. Yin, J. Sun, Y. Xiang, C. Shang, Recycling and reuse of rusted iron particles containing core-shell Fe-FeOOH for ibuprofen removal: Adsorption and persulfate-based advanced oxidation, Journal of Cleaner Production, 178 (2018) 441-448.

[37] B. Guo, K. Sasaki, T. Hirajima, Selenite and selenate uptaken in ettringite: Immobilization mechanisms, coordination chemistry, and insights from structure, Cement and Concrete Research, 100 (2017) 166-175.

[38] Z. Nie, N. Finck, F. Heberling, T. Pruessmann, C. Liu, J. Lützenkirchen, Adsorption of selenium and strontium on goethite: EXAFS study and surface complexation modeling of the ternary systems, Environmental Science & Technology, 51 (2017) 3751-3758.

[39] L. Zhu, L. Zhang, J. Li, D. Zhang, L. Chen, D. Sheng, S. Yang, C. Xiao, J. Wang, Z. Chai, Selenium sequestration in a cationic layered rare earth hydroxide: a combined batch experiments and EXAFS investigation, Environmental Science & Technology, 51 (2017) 8606-8615.

[40] N. Jordan, A. Ritter, A.C. Scheinost, S. Weiss, D. Schild, R. Hübner, Selenium (IV) uptake by maghemite (γ-Fe_2O_3), Environmental Science & Technology, 48 (2014) 1665-1674.

[41] N. Jordan, A. Ritter, H. Foerstendorf, A. Scheinost, S. Weiß, K. Heim, J. Grenzer, A. Mücklich, H. Reuther, Adsorption mechanism of selenium (VI) onto maghemite, Geochimica et Cosmochimica Acta, 103 (2013) 63-75.

[42] K.F. Hayes, A.L. Roe, G.E. Brown, K.O. Hodgson, J.O. Leckie, G.A. Parks, In situ X-ray absorption study of surface complexes: Selenium oxyanions on α-FeOOH, Science, 238 (1987) 783-786.

[43] D. Peak, Adsorption mechanisms of selenium oxyanions at the aluminum oxide/water interface, Journal of Colloid and Interface Science, 303 (2006) 337-345.

[44] H.C.B. Hansen, O.K. Borggaard, J. Sørensen, Evaluation of the free energy of formation of Fe(II)-Fe(III) hydroxide-sulphate (green rust) and its reduction of nitrite, Geochimica et Cosmochimica Acta, 58 (1994) 2599-2608.

[45] C. Bhave, S. Shejwalkar, A review on the synthesis and applications of green rust for environmental pollutant remediation, International journal of environmental science and technology, 15 (2018) 1243-1248.

[46] M. Usman, J. Byrne, A. Chaudhary, S. Orsetti, K. Hanna, C. Ruby, A. Kappler, S. Haderlein, Magnetite and green rust: synthesis, properties, and environmental applications of mixed-valent iron minerals, Chemical Reviews, 118 (2018) 3251-3304.

[47] M.A. Nabar, S.V. Paralkar, Studies on selenates: II. Thermal decomposition of heavier rare-earth selenate hydrates, Thermochimica Acta, 17 (1976) 239-246.

[48] L.V. Constantino, J.N. Quirino, A.M. Monteiro, T. Abrão, P.S. Parreira, A. Urbano, M.J. Santos, Sorption-desorption of selenite and selenate on Mg-Al layered double hydroxide in competition with nitrate, sulfate and phosphate, Chemosphere, 181 (2017) 627-634.

[49] S.-L. Wang, C.H. Liu, M.K. Wang, Y.H. Chuang, P.N. Chiang, Arsenate adsorption by Mg/Al–NO_3 layered double hydroxides with varying the Mg/Al ratio, Applied clay science, 43 (2009) 79-85.

[50] E.M. Opiso, T. Sato, T. Yoneda, Immobilization of selenium by Mg-bearing minerals and its implications for selenium removal from contaminated water and wastewater, Applied clay science, 123 (2016) 121-128.

[51] X. Hou, R.J. Kirkpatrick, Solid-State ^{77}Se NMR and XRD Study of the Structure and Dynamics of Seleno-Oxyanions in Hydrotalcite-like Compounds, Chemistry of Materials, 12 (2000) 1890-1897.

Chapter 7

Conclusions

Stabilization/solidification (S/S) has been always adopted as an essential technology for the safe disposal of hazardous wastes. Geopolymers have been attracted much attention for the S/S treatment because of their good properties. Moreover, it has been also certified that geopolymers can be effective for the immobilization of cationic pollutants. However, few studies have focused on the immobilization of anionic species in geopolymer. On the other hand, selenium contamination has been of great concern globally, due to the vast of anthropogenic activities such as mining and disposals of tailings, coal fly ash, or other industrial wastes. Furthermore, isotope ^{79}Se as one of the fission products in nuclear waste possesses a long half-life (approximately 2.95×10^5 yrs.). Thus, in this thesis, some strategies have been used to enhance the S/S performance of Se oxyanions in geopolymer, and the corresponding mechanisms have been also proposed.

In **Chapter 1**, the background information about hazardous waste pollution, the policies for solid waste treatment, treatment techniques, etc. The different materials used for S/S treatment were summarized and compared. Then, the significances and objectives of this thesis were specified and proposed. Furthermore, all methodologies used in this thesis were summarized in **Chapter 2**.

In **Chapter 3**, the immobilization of SeO_3^{2-} and SeO_4^{2-} was explored using geopolymers activated by different alkaline solutions. The effect of calcined hydrotalcite on their leaching performances was also studied. It has been found that lower leaching percentages of SeO_3^{2-} and SeO_4^{2-} (approximately 10% and 18%) can be achieved in Na_2SiO_3-activated geopolymers (S9 and S11) with the comparison of NaOH-activated geopolymers (approximately 58% and 74% for S3 and S5, respectively). Based on the LCF and TG results, it has been proven that electrostatic

interaction is the main association mode of SeO_3^{2-} and SeO_4^{2-} in both NaOH- and Na_2SiO_3-activated geopolymers. Therefore, the leaching behaviors of SeO_3^{2-} and SeO_4^{2-} should have a close relationship with the compactness of geopolymer. According to the BET results, the addition of CHT can increase the specific surface areas and pore sizes of both NaOH- and Na_2SiO_3-geopolymers. This can be the main reason why the Se leaching amount increased from Na_2SiO_3-activated geopolymers (S10 and S12) where LDHs were not formed. While the leaching percentages of SeO_3^{2-} and SeO_4^{2-} decreased to approximately 50% and 60%, respectively, after the CHT was added into NaOH-activated geopolymers (S4 and S6), and this was mainly because of the formation of LDHs in these pastes. In addition, Na_2SiO_3-activated geopolymers showed much higher compressive strength (> 25 MPa) than NaOH-activated geopolymers (< 15 MPa). Therefore, Na_2SiO_3-activated geopolymer can be the promising material for the immobilization of Se oxyanions.

According to **Chapter 3**, the soluble silicate has a significant effect on the re-formation of layered double hydroxide (LDH). Thus, in **Chapter 4**, the effect of silicate on the phase transformations of calcined layered double hydroxides for the immobilization of SeO_3^{2-} and SeO_4^{2-} was explored at pH 10 and 13, respectively. It has been found that both pH and silicate have significant effects on the immobilization of SeO_3^{2-} and SeO_4^{2-} using CLDHs. The sorption amounts of them dramatically decreased when pH became higher. This is mainly because there is a larger amount of OH^- in the solution with a higher pH, thereby leading to the less positive surface charge of regenerated LDHs and increased competition between Se oxyanions and OH^- into LDH interlayers. On the other hand, the silicate ion can have adverse effects on the memory effect of LDHs. Specifically, silicate ion could react with the MgO and Al_2O_3

in CLDHs to accordingly generate magnesium silicate hydrate and geopolymer-like substance, certified by NMR and XPS results. These substances covered on the surface of CLDHs and blocked the hydroxylation of metal oxides, resulting in the non-regeneration of LDHs particularly for CLDH-1 and CLDH-4 after reaction at pH 10 in the presence of silicate. However, higher pH can suppress the interaction between MgO and silicate and enhance the formation of geopolymer-like substance, which relatively promotes the regeneration of LDHs. Al in CLDHs plays a critical role in the regeneration of LDHs. Overall, the ternary oxides (CLDH-2 and CLDH-3) have more resistance to the impact of silicate, mainly because they possess much larger specific surface areas (127.7 and 158.2 m^2/g) than binary oxides.

The LDHs were always formed in the NaOH-activated geopolymers and showed suppressive effect on Se leaching in **Chapter 3**. A novel composite of layered double hydroxide/geopolymer (LDH/GEO) was synthesized using sol-gel and co-precipitation in **Chapter 5**. It was found that the surface of geopolymer was homogeneously covered by the LDH platelets, evidenced by SEM-EDX, particle size, and zeta potential measurements. The ability of LDH/GEO to sorb Cs^+ was maintained as that of pure GEO. In the binary system (Cs^+ + SeO_4^{2-}), the sorption amount of Cs^+ onto GEO and LDH/GEO would decrease due to the existence of ion-pair $[CsSeO_4]^-$. However, it has less effect on the sorption of SeO_4^{2-} onto both pure LDH and LDH/GEO, and this could be because of the stronger attraction of LDH layer to SeO_4^{2-}. On the other hand, film diffusion governed the sorption process of Cs^+ onto pure GEO via ion exchange. However, the sorption of Cs^+ onto LDH/GEO composite was controlled by particle diffusion. This could be explained by the fact that the sodium ions located in the surface layers of GEO would be moved out or go depth inside the structure because

of the charge repulsion between LDH layer and sodium ion. "Pocket diffusion" was defined because this kind of diffusion would be restricted to a certain distance around the ring entrance gate due to the amorphous essence of GEO. For SeO_4^{2-} sorption, it occurred by ion-exchange with the interlayer NO_3^- and surface sorption. Importantly, the sorption of SeO_4^{2-} onto LDH/GEO composite is much faster than the case of pure LDH. The current results demonstrate that the LDH/GEO composite could be a kind of cost-effective, environmentally friendly material for co-immobilization of Cs^+ and SeO_4^{2-}.

In **Chapter 6**, the mixtures of metal oxide (CaO or MgO) and ferrous salt were used for the immobilization of SeO_4^{2-}, respectively. For CaO-based reaction, almost all of SeO_4^{2-} was reduced to SeO_3^{2-} within 7 days. EXAFS results indicated that the generated SeO_3^{2-} was mainly adsorbed onto the iron-based minerals (Fe_2O_3 and FeOOH) through the formation of both bidentate mononuclear edge-sharing (^1E) and monodentate mononuclear corner-sharing (^1V) inner-sphere surface complexes. Thus, a low leaching amount of Se (approximately 5%) was obtained for CaO-based reaction. However, only 45.50% of SeO_4^{2-} was reduced to SeO_3^{2-} in 7 days, and more than 40% of Se was leached out for MgO-based reaction. But the existence of Fe(II) can also indicate that the reaction system of MgO and ferrous salt can last for a longer time (more than 7 days). In terms of the Se association in the MgO-based reaction sample, most of the selenium (SeO_3^{2-} and SeO_4^{2-}) was preferentially distributed onto the $Mg(OH)_2$ through outer-sphere adsorption.

In **Chapter 7**, the main conclusions of this thesis were summarized. It has been found that both SeO_3^{2-} and SeO_4^{2-} can be immobilized in geopolymer through electrostatic interaction. The specific reaction processes and mechanisms have been

explored and proposed. The reaction system of metal oxide and ferrous salt could be introduced to geopolymer reaction, and this might be an alternative way to further enhance the S/S efficiencies using geopolymer.

Acknowledgments

My deepest gratitude goes first and foremost to my respectable supervisor, Prof. Keiko Sasaki, for her constant encouragement, guidance, and support. She always guided me with practical academic advice and feasible instructions and enlightened me while I was confused during the doctoral period. She has offered me many valuable suggestions in my academic studies, and her insightful ideas and meaningful inspirations have benefited me a lot. Her incisive comments and constructive criticisms have greatly contributed to the completion of this thesis. Without her strong support, this thesis cannot have reached its present form.

I am also grateful to Prof. Kazuya Idemitsu (Department of Applied Quantum Physics and Nuclear Engineering) and Assoc. Prof. Hajime Miki who belong to my thesis defense committee. Their insightful criticisms and suggestions on my dissertation greatly help me to improve this work.

Then, I would like to express my appreciation to Emeritus Prof. Tsuyoshi Hirajima, Assoc. Prof. Naoko Okibe and Assistant Prof. Moriyasu Nonaka, who always give me kind helps and suggestions on my academic research and daily life in Japan. Also, I would like to give the special thanks to Ms. Makiko Semba who invariably edits and files many kinds of documents for us silently.

As a PhD candidate, I spent the majority of time with other members of Mineral Processing, Recycling and Environmental Remediation laboratory, and I received enormous help from them. It is them who create the harmonious and pleasant environment in the office. I would like to express my most heartfelt thanks to them and list their names as bellows: Dr. Binglin Guo, Dr. Chitiphon Chuaicham, Dr. Santisak Kitjanukit, Dr. Kojo Twum Konadu, Dr. Keishi Oyama, Dr. Wuhui Luo, Dr.

Gde Pandhe Wisnu Suyantara, Dr. Paulmanickam Koilraj, Dr. Pawar Radheshyam Rama, Dr. Karthikeyan Sekar, Shingo Nakama, Shunsuke Imamura, Haruki Noguchi, Ryohei Nishi, Mengmeng Wang, Li Zhang, Yu Tanaka, Yuta Orii, Tsubasa Oji, Ryoutaro Sakai, Zenta Shirozu, Yuki Semoto and Kaito Hayashi. Thank you for sharing time with me.

Last but not the least, I would like to appreciate the scholarship provided by China Scholarship Council (No. 201706420068). Without the CSC scholarship, I cannot put all of my efforts in academic research. In addition, all of my academic works were supported to Prof. Keiko Sasaki by the Japan Society for the Promotion of Science (JSPS) KAKENHI (No. JP16H02435, JP19H00883). I am very grateful for the opportunity studying for Ph.D. degree in Kyushu University.

Finally, I really appreciate my parents for their financial and spiritual support.

September 2020, Quanzhi Tian
Kyushu University
Fukuoka, Japan